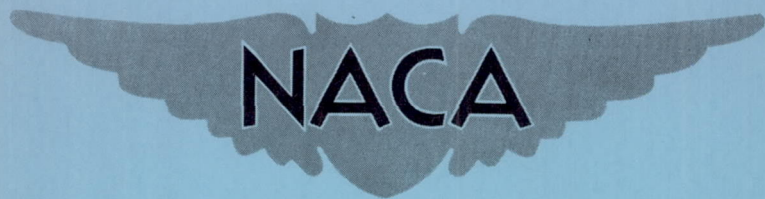


NACA RM A51F12



RESEARCH MEMORANDUM

WIND-TUNNEL TESTS OF A 1/12-SCALE MODEL OF THE X-3 AIRPLANE
AT SUBSONIC AND SUPERSONIC SPEEDS

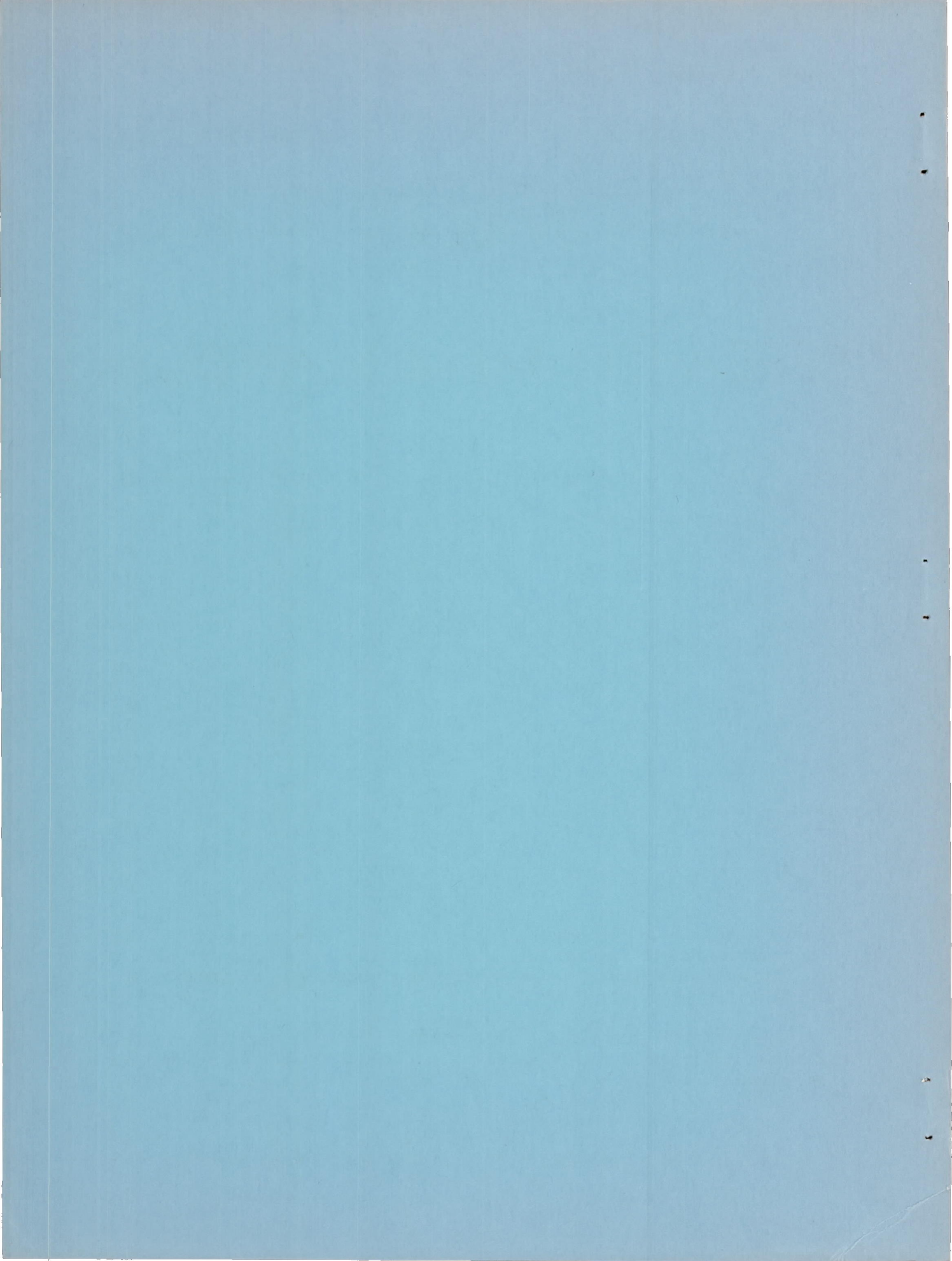
By Robert N. Olson and Robert S. Chubb

Ames Aeronautical Laboratory
Moffett Field, Calif.

NATIONAL ADVISORY COMMITTEE
FOR AERONAUTICS

WASHINGTON

September 14, 1951
Declassified July 17, 1958



NATIONAL ADVISORY COMMITTEE FOR AERONAUTICS

RESEARCH MEMORANDUM

WIND-TUNNEL TESTS OF A 1/12-SCALE MODEL OF THE X-3 AIRPLANE

AT SUBSONIC AND SUPERSONIC SPEEDS

By Robert N. Olson and Robert S. Chubb

SUMMARY

The static longitudinal-, lateral-, and directional-stability and control characteristics of a 1/12-scale model of the Douglas X-3 airplane at subsonic and supersonic Mach numbers are presented. The model was equipped with an all-movable horizontal tail, an aileron on the left wing, and a rudder on the vertical-tail surface. The investigation covered a range of Mach numbers from 0.60 to 0.93 and 1.30 to 1.91 at Reynolds numbers of 0.98 to 2.61 million.

In general, the lift-curve slope gradually increased with increasing subsonic speed up to a Mach number of 0.93, and gradually decreased with increasing supersonic speed up to a Mach number of 1.91. A slight increase in drag coefficient was evident at a Mach number of 0.90, but the drag-divergence Mach number was not reached within the subsonic Mach number range of the tests. At supersonic speeds, the drag coefficient for lift coefficients less than 0.3 gradually decreased with increasing speed up to a Mach number of 1.91.

The first results of the stability investigation indicated that at a Mach number of 0.85, the airplane would have marginal longitudinal stability for moderate lift coefficients and at a Mach number of 1.91, have nearly neutral longitudinal stability for high values of lift coefficient with the controls set for zero pitching moment. The use of a larger horizontal tail (38.4-percent larger area) of higher aspect ratio (4.33 as compared with 3.05 for the original configuration) was shown to eliminate the marginal longitudinal-stability region at 0.85 Mach number and to provide adequate longitudinal stability for all lift coefficients for zero pitching-moment conditions at a Mach number of 1.91.

The effectiveness of the all-movable horizontal tail in providing longitudinal control was found to be constant with increasing subsonic Mach number, but the results indicate about a 40-percent decrease in

the pitching-moment effectiveness with increasing speed in the range of Mach numbers from 1.30 to 1.91.

Although the results indicate that the airplane will be directionally and laterally stable in the subsonic and supersonic speed ranges investigated, the directional stability may be marginal for small angles of sideslip at a Mach number of 0.90.

The directional- and lateral-control data indicate linear variations of yawing-moment coefficient with rudder deflection and rolling-moment coefficient with aileron deflection for the airplane little affected by angle of attack.

INTRODUCTION

In order to aid in the prediction of the stability and control characteristics of the X-3 airplane (Air Force Project MX-656) and to provide a sound basis for the flight investigations which will be conducted using this proposed supersonic research vehicle, the aerodynamic characteristics of a 1/12-scale model of the X-3 airplane have been determined from tests made in the Ames 6- by 6-foot supersonic wind tunnel.

The present report gives the results of force tests of the 1/12-scale model of the X-3 research airplane made to determine the longitudinal-, lateral-, and directional-stability and control characteristics at Mach numbers of from 0.60 to 1.91, inclusive. Results of additional tests made to determine the effects on the longitudinal-stability characteristics of increasing the size of the horizontal tail are also presented. Static pressures at various fuselage stations, obtained in conjunction with the force tests, are presented for use in determining canopy loads and possible airspeed-orifice locations.

COEFFICIENTS AND SYMBOLS

All data are presented as standard NACA coefficients of forces and moments referred to the axes shown in figure 1. With the exception of the horizontal-tail hinge moments, all data were referred to a longitudinal center-of-gravity position at the leading edge of the wing mean aerodynamic chord and a vertical position 1-inch-model scale above the fuselage reference line.

Sufficient data are presented to permit the reader to compute the yawing moments and rolling moments about the stability axes.

Horizontal-tail hinge moments for both configurations investigated were measured about an axis positioned at the 25-percent point of the mean aerodynamic chord of the exposed tail of configuration A which passes through the plane of symmetry at the 54.7-percent point of the theoretical root chord.

The symbols and coefficients are defined as follows:

$$C_L \quad \text{lift coefficient} \quad \left(\frac{\text{lift}}{qS} \right)$$

$$C_D \quad \text{drag coefficient} \quad \left(\frac{\text{drag}}{qS} \right)$$

$$C_m \quad \text{pitching-moment coefficient} \quad \left(\frac{\text{pitching moment}}{qSc} \right)$$

$$C_h \quad \text{horizontal-tail hinge-moment coefficient} \quad \left(\frac{\text{hinge moment}}{q S_t \bar{c}_t} \right)$$

(Moment tending to lower trailing edge is positive.)

$$C_Y \quad \text{cross-wind-force coefficient} \quad \left(\frac{\text{cross-wind force}}{qS} \right)$$

$$C_n \quad \text{yawing-moment coefficient} \quad \left(\frac{\text{yawing moment}}{qSb} \right)$$

$$C_l \quad \text{rolling-moment coefficient} \quad \left(\frac{\text{rolling moment}}{qSb} \right)$$

$$C_{L_\alpha} \quad \text{rate of change of lift coefficient with angle of attack, per degree}$$

$$C_{Y_\beta} \quad \text{rate of change of cross-wind-force coefficient with angle of sideslip, measured at constant angle of attack, per degree}$$

$$C_{n_\beta} \quad \text{rate of change of yawing-moment coefficient with angle of sideslip, measured at constant angle of attack, per degree}$$

$$C_{l_\beta} \quad \text{rate of change of rolling-moment coefficient with angle of sideslip, measured at constant angle of attack, per degree}$$

$\frac{dC_m}{di_t}$ rate of change of pitching-moment coefficient with horizontal-tail incidence, measured at constant lift coefficient, per degree

a local speed of sound, feet per second

b wing span, feet

b_t horizontal-tail span, feet

c chord of the wing parallel to plane of symmetry, feet

c_t chord of the horizontal tail parallel to plane of symmetry, feet

\bar{c} mean aerodynamic chord of the wing $\left(\frac{\int_0^{b/2} c^2 dy}{\int_0^{b/2} c dy} \right)$, feet

\bar{c}_t mean aerodynamic chord of the horizontal tail $\left(\frac{\int_0^{b_t/2} c_t^2 dy_t}{\int_0^{b_t/2} c_t dy_t} \right)$, feet

c_p specific heat at constant pressure

c_v specific heat at constant volume

i_t horizontal tail incidence with respect to the fuselage reference line, positive with the trailing edge downward, degrees

n mass flow

p local static pressure, pounds per square foot

p_o free-stream static pressure, pounds per square foot

q free-stream dynamic pressure $\left(\frac{1}{2} \rho V^2 \right)$, pounds per square foot

y perpendicular distance along the wing semispan from the model plane of symmetry, feet

- y_t perpendicular distance along the horizontal-tail semispan from the model plane of symmetry, feet
- A cross-sectional area of duct, square feet
- E ratio of duct outlet area to inlet area
- H total pressure, pounds per square foot
- ΔH (total pressure in the free stream) - (total pressure in the air duct)
- M Mach number $\left(\frac{V}{a}\right)$
- P pressure coefficient $\left(\frac{p-p_o}{q}\right)$
- R Reynolds number, based on the mean aerodynamic chord of the wing
- S wing area, including that portion enclosed by the fuselage as determined by extending the leading and trailing edges to the plane of symmetry, square feet
- S_t area of horizontal tail, including that portion enclosed by the fuselage as determined by extending the leading and trailing edges to the plane of symmetry, square feet
- V free-stream velocity, feet per second
- α angle of attack of the fuselage reference line, degrees
- β angle of sideslip, degrees
- γ ratio of specific heats $\left(\frac{c_p}{c_v}\right)$
- δ_a aileron deflection, positive downward, degrees
- δ_r rudder deflection, positive with trailing edge to left, degrees
- ρ mass density in the free stream, slugs per cubic foot

The following notation is used in the figures to signify various combinations of the component parts of the model:

- BW combination of body and wing

BWV combination of body, wing, and vertical-tail surface

BWH combination of body, wing, and horizontal-tail surface

APPARATUS

Wind Tunnel and Equipment

The stagnation pressure in the Ames 6- by 6-foot supersonic wind tunnel can be regulated to maintain a given test Reynolds number. The supersonic Mach number can be varied continuously by use of the asymmetric adjustable nozzle, and the subsonic Mach number through regulation of the compressor speed with the nozzle set at the maximum-open position. A more complete discussion of the tunnel characteristics is presented in reference 1.

The model (shown in fig. 2) was mounted on a sting-type support system. For the investigation of longitudinal characteristics, the model was mounted with the plane of the wing vertical to permit continuous variation of angle of attack; while for the investigation of lateral and directional characteristics, the model was mounted with the plane of the wing horizontal to permit continuous adjustment of angle of yaw. The aerodynamic forces and moments on the model were measured by a six-component, electric resistance-type, strain-gage balance mounted on the sting support and enclosed within the body of the model. Hinge moments on the horizontal tail were measured by strain gages mounted on a cantilever-type beam contained within the fuselage.

Model

The 1/12-scale model of the X-3 research airplane was furnished by the Douglas Aircraft Company. A sketch of the model is shown in figure 3, and the geometry and dimensions of the wing and tail are given in table I. The model was provided with engine air intake scoops. Boundary-layer bleed scoops were not incorporated within the inlets; hence, the area of the intake scoops was made to equal the combined area of the engine air intake and boundary-layer bleed scoops. Engine air ducting was simulated to the stern of the fuselage. Constriction plates were furnished for the duct exits to provide exit to inlet area ratios of 0.779 and 0.877. An aileron was provided on the left wing, and the vertical tail had a rudder. Two all-movable horizontal tails were provided for the investigation of longitudinal control. (See fig. 3.) The positions of static pressure tubes inside the ducts and along the fuselage surface are shown in figure 4.

TESTS AND REDUCTION OF DATA

Range of Test Variables

The longitudinal stability and control characteristics of the model were investigated for a range of Mach numbers from 0.60 to 0.93 and from 1.30 to 1.91. Directional- and lateral-control characteristics were investigated at 1.40 Mach number only, while the lateral and directional stability characteristics were obtained at Mach numbers of 0.90, 1.40, and 1.91. Some additional longitudinal-stability and control characteristics were obtained at selected Mach numbers for the complete model incorporating a horizontal tail larger than that used on the original configuration. Henceforth, in this report, the model incorporating a horizontal tail of aspect ratio 3.05 shall be referred to as configuration A, and with the larger horizontal tail of aspect ratio 4.33 shall be referred to as configuration B. (See fig. 3.)

Reynolds number effect was investigated over a range of 1.0 to 2.6 million (based on the mean aerodynamic chord of the wing) in both the subsonic and supersonic Mach number ranges.

Static pressures at various fuselage stations were obtained for Mach numbers of 1.3, 1.5, and 1.7.

Precision

The accuracy of the results can be estimated by consideration of the uncertainty in determining angle of attack, in measuring tunnel pressures, and in measuring forces and moments with the strain-gage balance. A more detailed discussion of the factors involved is presented in reference 2. The following table lists the estimated accuracy of measurement or computation of various quantities and coefficients:

	<u>Maximum uncertainty</u>
Angle of attack	$\pm 0.1^\circ$
Horizontal-tail incidence	$\pm .2^\circ$
Mach number	$\pm .01$
Reynolds number	$\pm .03 \times 10^6$
Lift coefficient	$\pm .003$
Drag coefficient	$\pm .0015$
Pitching-moment coefficient	$\pm .001$
Hinge-moment coefficient	$\pm .004$

	<u>Maximum uncertainty</u>
Cross-wind force coefficient	±.002
Yawing-moment coefficient	±.001
Rolling-moment coefficient	±.001

Reduction of Data

With the exception of the drag data obtained for configuration B at a Mach number of 1.91, all data were obtained for the model with a duct outlet to inlet area ratio of 0.779 which produced a mass-flow ratio versus Mach number relationship corresponding to that of figure 5. The mass-flow-ratio values used in figure 5 were calculated by means of the following equation:

$$\frac{m_1}{m_0} = \frac{H_3}{H_0} \frac{A_3}{A_1} \frac{M_3}{M_0} \left(\frac{1 + \frac{\gamma-1}{2} M_0^2}{1 + \frac{\gamma-1}{2} M_3^2} \right)^{\frac{\gamma+1}{2(\gamma-1)}}$$

In the above equation, subscript 1 indicates duct inlet, subscript 3 indicates the duct station 4.5 inches from the duct outlet (the duct station of cross-sectional area equal to the duct outlet area), and subscript 0 indicates free-stream conditions. The total pressure in the air duct (H_3) was measured by means of a single total-head tube mounted at the center line of the duct. However, a subsequent survey of the total-pressure variation across the duct by means of a seven-tube total-head rake showed the pressure as measured by the single center tube to be within 3 percent of the average pressure as determined from the pressure survey.

The test data have been reduced to standard NACA coefficient form and corrected for the following factors which would affect the accuracy of the results.

Tunnel-wall interference.— The subsonic results have been corrected for the induced effects of the tunnel walls resulting from lift on the model (see reference 3) by the addition of the following:

$$\Delta\alpha = 0.265 C_L$$

$$\Delta C_D = .0046 C_L^2$$

Corrections for the effects of the tunnel walls on pitching-moment coefficients were negligible and have been omitted.

Constriction corrections to account for the blocking effect of the model in the tunnel test section at subsonic speeds were applied according to the method of reference 4. At 0.90 Mach number, this correction amounted to 3.3-percent increase in Mach number over that for tunnel without the model in place.

Stream variations.— A pressure survey at subsonic speeds has indicated that the longitudinal variation of static pressure in the region of the model is less than 2 percent of the dynamic pressure. No correction for this effect was made. Subsonic tests of a symmetrical model in both the normal and the inverted positions have indicated no significant stream curvature or inclination in the plane in which the model was pitched (model mounted with plane of wing in vertical position).

A survey of the air stream in the test section at supersonic speeds (reference 1) has indicated that the cross flow is very small at all Mach numbers. However, significant variations of stream inclination and curvature occur in the vertical and axial directions at Mach numbers greater or less than 1.4. Therefore, the directional- and lateral-stability characteristics are presented for both the inverted and normal positions. The survey also indicated that the static-pressure variations at supersonic speeds other than 1.4 were of sufficient magnitude to affect the drag results. A correction was added to the measured drag coefficient to account for the buoyancy caused by this longitudinal pressure gradient. This correction varied from a drag coefficient of 0.0009 at a Mach number of 1.30 to -0.0008 at a Mach number of 1.91.

Support interference.— Interference effects of the sting support at both high subsonic and supersonic speeds are unknown and, therefore, no corrections were applied. However, interference effects of the sting support on the aerodynamic characteristics of a 0.16-scale model of the X-3 airplane have been determined previously at low speed by testing the model in the Ames 7- by 10-foot wind tunnel with and without a dummy sting behind the fuselage. Results of the low-speed tests showed a negligible variation in the lift or pitching-moment-coefficient tares due to sting interference for the complete model. The low-speed drag-coefficient tare for the complete configuration remained constant at a value of 0.003 over the 0° to 5° angle-of-attack range, then gradually increased to a value of 0.010 at 10° angle of attack, and remained constant from 10° to 24° angle of attack. Further, unpublished data on file at this laboratory indicate the interference effects do not vary with speed up to a Mach number of 0.9; therefore, the subsonic variations of pitching-moment coefficient and drag coefficient with Mach number probably were not influenced by sting interference.

Pressures were measured at the base of the fuselage, and all drag data were adjusted to correspond to a base pressure equal to free-stream static pressure.

RESULTS AND DISCUSSION

All the force and moment data obtained during the investigation are presented in figures 6 through 34. For convenience, an index of these figures is presented in table II. All fuselage static-pressure data, presented without comment, are included in table III. Unless otherwise noted, all data were obtained for the model with the duct outlet to inlet area ratio of 0.779 which produced a mass-flow ratio versus Mach number relationship corresponding to that of figure 5.

Lift Characteristics

The variation of lift coefficient with angle of attack, for subsonic speeds, was essentially linear up to the stall except for a slight decrease in slope near zero angle of attack. (See figs. 6(a) and 7(a).) This decrease was most pronounced at the highest subsonic speeds investigated. Results of tests in the Ames 6- by 6-foot wind tunnel (reference 5) of an aspect ratio 3.1, unswept wing have shown a similar lift-curve trend near zero angle of attack at these Mach numbers. An increase in the aspect ratio of the horizontal tail (3.05 to 4.33) eliminated the decrease in slope of the lift curve near zero angle of attack for zero incidence of the horizontal tail (fig. 8(a)), but not the decrease in slope near zero lift for a -9.6° incidence of the horizontal tail (fig. 9(a)).

The increase in lift coefficient beyond the angle of attack at which the wing stalled,¹ evident at Mach numbers of 0.60 to 0.85 (fig. 6), was probably due to lift provided by the fuselage. Choked flow conditions in the tunnel, indicated by broken lines in the subsonic-data curves, prevented the attainment of the angle of attack for stall above a Mach number of 0.85.

At supersonic speeds, the lift-coefficient variation with angle of attack for small tail incidences was linear up to a lift coefficient of 0.4, beyond which the rate of increase of lift coefficient with angle of attack diminished with increasing lift coefficient. (See part (a) of figs. 10 through 15.) Increasing the tail aspect ratio (configuration B) had little effect on the lift-coefficient variation with angle of attack at supersonic speeds. (See part (a) of figs. 16 through 18.)

¹Stall is herein defined as the condition where the slope of the lift curve first becomes zero at a positive angle of attack.

Except at a Mach number of 0.90, where the lift-curve slope at a Reynolds number of 0.98 million was appreciably greater than that for the higher Reynolds numbers, Reynolds number had no significant effect on the lift characteristics up to the angle of attack for stall at subsonic speeds (figs. 19 through 22) nor through the entire angle-of-attack range investigated at supersonic speeds (figs. 23 through 25) for the range of Reynolds numbers investigated (0.98 to 2.61 million at subsonic speeds; 1.5 to 2.61 million at supersonic speeds).

The variation of lift-curve slope with Mach number is presented in figure 35 for various lift coefficients. A loss in lift-curve slope in the region of 0.85 Mach number occurs at a lift coefficient of 0.3, and at 0.93 Mach number near zero lift; however, the loss is not of sufficient magnitude to be of concern. At supersonic speeds, the lift-curve slope generally tends to decrease gradually with increasing Mach number and decreases with increasing lift coefficient throughout the supersonic speed range investigated.

Static Longitudinal Stability and Control

The variation of pitching-moment coefficient with lift coefficient was not linear for any of the subsonic test Mach numbers. (See fig. 6(b).) Near zero lift, the static longitudinal stability decreased rapidly with increasing Mach number until, at a Mach number of 0.93, the model became neutrally stable. At a Mach number of 0.85, this region of marginal stability persists over a range of lift coefficients from -0.10 to 0.25.

At lift coefficients of 0 to 0.3, a linear variation of pitching-moment coefficient with lift coefficient exists for configuration A (aspect-ratio-3.05 horizontal tail) for Mach numbers of 1.30 to 1.91, inclusive. (See figs. 10 through 15). Beyond a lift coefficient of 0.3, the static longitudinal stability generally decreased with increasing lift coefficient. This decrease in stability with increasing lift coefficient became more rapid with increasing Mach number until at a Mach number of 1.91 nearly neutral stability existed for configuration A at high values of lift coefficient with the controls set for zero pitching moment.

Because of the region of nearly neutral stability at a Mach number of 1.91 and the marginal stability existing for moderate lift coefficients at a Mach number of 0.85, additional tests were made of the 1/12-scale X-3 model incorporating a horizontal tail of greater aspect ratio (4.33 as against 3.05 for the original configuration) and 38.4-percent greater area. This larger tail model has been designated

configuration B. Figure 8(b) shows that use of the revised horizontal tail completely eliminated the regions of marginal stability at all lift coefficients up to the stall for all subsonic Mach numbers investigated. No marked changes in the static longitudinal stability were evident for Mach numbers of 1.3 and 1.6. At a Mach number of 1.9, however, use of the higher aspect-ratio tail did eliminate the neutral stability existing at high values of lift coefficient for $C_m=0$ conditions for the original configuration. (See figs. 16, 17, and 18.)

The investigation of Reynolds number effect at subsonic speeds showed that results obtained at 0.98-million Reynolds number generally exhibited a greater longitudinal stability than existed at the higher Reynolds numbers of 2.29 to 2.61 million. (See figs. 19, 20, 21, and 22.) At supersonic speeds, no appreciable Reynolds number effect was apparent for Reynolds numbers of 1.57 to 2.61 million. (See figs. 23, 24, and 25.)

The variation of static longitudinal stability with Mach number shown in figure 36 for lift coefficients of 0 and 0.3 indicates that the most forward position of the neutral point is at about 4 percent of the mean aerodynamic chord and occurs at a Mach number of 0.85. Thus, for a center-of-gravity position at the leading edge of the wing mean aerodynamic chord, a minimum stability margin of 4 percent is attained for model configuration A. Use of the 4.33-aspect-ratio horizontal tail (configuration B), however, increases this minimum stability margin to 17 percent while retaining a total center-of-pressure movement, over the investigated Mach number range, about the same as that for configuration A (about 45 percent of the mean aerodynamic chord).

A comparison of the tail-on (configuration A) and tail-off (BW) pitching-moment characteristics (figs. 10 through 15) indicates the tail was destabilizing at lift coefficients above 0.65 for the Mach number range of 1.30 to 1.91. Also, the tail-off configuration was stable throughout the angle-of-attack range investigated for Mach numbers of 1.3 to 1.7, inclusive, but became neutrally stable above an angle of attack of 10° at a Mach number of 1.91.

At a Mach number of 1.3, the horizontal-tail effectiveness gradually decreased with increasing tail deflection. This loss in effectiveness with increasing tail deflection substantially decreased with increasing Mach number until at a Mach number of 1.7, at moderate lift coefficients, the tail effectiveness was nearly linear throughout the tail deflection range investigated (0° to -25°).

A relatively constant tail effectiveness (fig. 37) is evident for the subsonic speed range investigated. At supersonic speeds, however,

the results indicate a reduction in tail effectiveness of about 40 percent for an increase in speed from a Mach number of 1.30 to 1.91. The 4.33-aspect-ratio tail (configuration B) was about 40 percent more effective than the 3.05-aspect-ratio tail (configuration A) as would be expected from almost a 40-percent greater tail area.

In general, the slope of the C_h versus C_L curve, for constant horizontal-tail deflection, is slightly negative for the entire angle-of-attack range investigated for Mach numbers of 1.30 to 1.91, inclusive. (See figs. 10(d) through 15(d).) The behavior of the hinge-moment coefficient with tail incidence was consistent with the variation of pitching-moment coefficient with tail incidence up to a tail deflection of -19.8° . The loss in effectiveness of the horizontal tail above -19.8° tail deflection was reflected in the hinge-moment-coefficient curves at a Mach number 1.3, but was not evident for Mach numbers of 1.4 to 1.91, inclusive.

Lateral and Directional Stability and Control

The lateral- and directional-stability characteristics of the model for Mach numbers of 0.90, 1.40, and 1.91 are shown in figures 26, 27, and 28. The model was tested in both the normal and inverted positions at all three Mach numbers to determine any possible effects of variations in stream angle on the stability characteristics of the model. As stated previously, no corrections have been made to these data for the unknown effects of sting interference.

A marked decrease in the directional stability near zero angle of sideslip is indicated at a Mach number 0.90. However, this region of nearly neutral stability may be due to the low test Reynolds number of the vertical stabilizing surface of the model. At a Mach number of 1.4, the yawing-moment-coefficient variation with sideslip angle was more nearly linear. At 1.91 Mach number, however, the nonlinear behavior is again evident with generally a greater directional stability existing for small angles of sideslip than for the larger angles of sideslip up to $\pm 6^\circ$.

The decrease in directional stability at small sideslip angles is reflected in the cross-wind-force coefficient versus angle-of-sideslip curves for 0.90 Mach number. (See part (b) of figs. 26, 27, and 28.) No other nonlinearities were indicated in the cross-wind-force characteristics at any of the three Mach numbers investigated.

The rolling moment due to sideslip (fig. 27(c)) was linear for a Mach number of 1.4, except for the broken-line portions of the curves

for the highest two lift coefficients investigated which, because of the asymmetry through zero sideslip, are believed to be unreliable data. At 0.90 and 1.91 Mach numbers (figs. 26(c) and 28(c)), the rolling moment due to sideslip was nonlinear for all values of lift coefficient investigated.

In figure 38 is shown the variation of the directional-stability, lateral-force, and effective-dihedral derivatives with lift coefficient for the model at a Mach number of 1.4 (derived from fig. 27). Because of the nonlinear nature of the lateral- and directional-stability curves at 0.90 and 1.91 Mach number, no attempt was made to determine the afore-mentioned derivatives for these Mach numbers. About a 50-percent loss in $C_{n\beta}$ is indicated in increasing the lift coefficient from 0 to 0.70. Almost no variation in the lateral-force derivative with lift coefficient was evident although the effective dihedral derivative became more negative with increasing lift coefficient.

No significant Reynolds number effect on the lateral and directional characteristics of the model was apparent over the range investigated. (See fig. 29.)

With the vertical tail removed, the results indicate the airplane would be directionally unstable at a Mach number of 1.4. (See fig. 30(a).) Adding the vertical tail produced the following changes in the stability derivatives: $C_{n\beta}$ from -0.0035 to 0.0052, $C_{y\beta}$ from -0.0085 to -0.0155, and $C_{l\beta}$ from 0.0009 to -0.0013. (See fig. 38.)

The effect of sideslip angle on the longitudinal characteristics is illustrated in figure 33. The results indicate that sideslip angle had no significant effect on the lift characteristics. However, the minimum drag coefficient for 6° of sideslip was about 0.010 greater than that for the unyawed condition. The pitching-moment coefficient increased, negatively, as much as 0.04 with increasing sideslip angle from 0° to 6° with the greater change occurring between 2° and 6° .

The directional-control characteristics for the model (figs. 30, 31, and 32) show a nearly linear variation of yawing-moment, cross-wind-force, and rolling-moment coefficients with rudder deflection, and were little affected by change in angle of attack (notwithstanding the broken-line portions of the rolling-moment characteristics at 10° angle of attack which data, because of the asymmetry through zero sideslip, are believed to be unreliable). Due to the high position of the vertical tail, the rolling moment due to rudder deflection is quite large, requiring about 3° differential deflection of the ailerons to balance the roll due to 5° rudder deflection. (See fig. 34.)

Results of the investigation of the lateral-control characteristics of the model indicate a nearly linear variation of rolling-moment coefficient with aileron deflection throughout the lift-coefficient range investigated. (See fig. 34.) It should be noted that these rolling-moment data are for deflection of one aileron only.

Drag Characteristics

Since the high-speed performance of airplanes is largely determined by the drag characteristics, the variation of drag coefficient with Mach number illustrated in figure 39 becomes of particular importance.

At subsonic speeds, a decrease in drag coefficient with increasing Mach number at constant lift coefficient is apparent in the range of 0.60 to 0.80 Mach number (fig. 39), and is associated with the increasing lift-curve slope with increasing Mach number at subsonic speed (fig. 35). Although there is a sudden increase in drag coefficient at a Mach number of 0.9 for a lift coefficient of 0.3, the increase is not sufficient to define the drag divergence Mach number.

At supersonic speeds, a gradual decrease in drag coefficient with increasing Mach number is evident for 0 and 0.3 lift coefficients up to a Mach number of 1.91. At a lift coefficient of 0.6, however, the drag coefficient decreases with increasing speed up to 1.6 Mach number above which there is a marked increase in drag coefficient up to the limiting Mach number of 1.91.

Substitution of the aspect-ratio-4.33 tail in place of the aspect-ratio-3.05 tail increased the drag of the model throughout the Mach number range investigated with the most marked increases occurring near Mach numbers of 0.80 and 1.30.

Several factors must be considered in correcting aerodynamic drag coefficients obtained from tests of a model in a wind tunnel to full-scale-airplane flight values. Among these are (a) the effects of Reynolds number, or the problem of correcting the viscous drag coefficient of a partly laminar flow at low Reynolds number to that of a fully turbulent flow at high Reynolds number; (b) the effects of the differences in surface condition of the model and airplane such as skin roughness, control surface gaps, and various protuberances; (c) the effect of base pressure, since a correction is necessary to adjust the base pressure coefficient of the model to that estimated for the jets-operating condition of the airplane; and (d) the effect of internal duct flow, since it is necessary to deduct from the total measured

model drag force the drag due to internal flow, defined in the same way as the engine manufacturer's net thrust, to obtain a drag for direct comparison with that estimated for the airplane. The drag due to internal flow is defined as the difference in total momentum between the flow issuing from the model at the exit and the flow ahead of the model in the free-stream tube entering the inlets. The magnitude of this drag due to internal flow is a function of the free-stream Mach number, ratio of exit total to free-stream total pressure, and mass-flow ratio. Sufficient data are presented in table III and figure 5 to permit calculation of this drag due to internal flow for the present investigation.

The extent of the foregoing corrections to the drag of the present 1/12-scale model has been estimated by the Douglas Aircraft Company to be of the following magnitudes (ΔC_D 's to be added to measured C_D 's):

	ΔC_D (Based on Wing Area)		
	<u>M = 1.3</u>	<u>1.5</u>	<u>1.7</u>
Effect of Reynolds number	-0.0055	-0.0058	-0.0060
Effect of surface condition	.0013	.0013	.0013
Effect of base pressure	.0015	.0015	.0015
Effect of internal duct flow	-.0035	-.0026	-.0016

By way of summation, totaling the corrections due to the various factors considered in converting the aerodynamic drag coefficients obtained from tests of the 1/12-scale model in the wind tunnel to full-scale-airplane flight values shows the minimum drag of the model to be approximately 10 percent higher than that to be expected of the airplane throughout the supersonic Mach number range of 1.3 to 1.7.

CONCLUDING REMARKS

The results of tests of a 1/12-scale model of the Douglas X-3 airplane in the Ames 6- by 6-foot supersonic wind tunnel have shown the following variations in the lift-curve slope and drag coefficient with Mach number. The lift-curve slope tended to increase with increasing subsonic speed up to a Mach number of 0.93, and gradually decreased with increasing supersonic speed up to a Mach number of 1.91. A slight increase in drag coefficient was evident at a Mach number of 0.90, but the drag-divergence Mach number was not reached within the subsonic Mach number range of the tests. At supersonic speeds and moderate lift coefficients, the drag coefficient gradually decreased with increasing speed up to a Mach number of 1.91.

Results of the stability investigation revealed a region of marginal longitudinal stability for moderate lift coefficients at a Mach number of 0.85 and nearly neutral longitudinal stability at high values of lift coefficient with the controls set for zero pitching moment at a Mach number of 1.91 for the original configuration. The use of a larger aspect-ratio horizontal tail of greater area (4.33 aspect ratio as against 3.05 for the original configuration, with a 38.4-percent increase in area) effectively eliminated the marginal longitudinal-stability region at 0.85 Mach number, and provided adequate longitudinal stability for high values of lift coefficient for $C_m=0$ conditions at a Mach number of 1.91.

The effectiveness of the all-movable tail in providing longitudinal control was nearly constant at subsonic speeds, but a 40-percent loss in effectiveness with increasing speed was indicated between Mach numbers of 1.30 and 1.91.

The directional stability, although adequate at Mach numbers of 1.40 and 1.91, was marginal for angles of sideslip near zero at a Mach number of 0.90.

Adequate lateral stability was indicated for all Mach numbers investigated (0.90, 1.40, and 1.91).

The directional- and lateral-control characteristics of the model indicate linear variations of yawing-moment coefficient with rudder deflection and of rolling-moment coefficient with aileron deflection, little affected by angle of attack.

Ames Aeronautical Laboratory,
National Advisory Committee for Aeronautics,
Moffett Field, Calif.

REFERENCES

1. Frick, Charles W., and Olson, Robert N.: Flow Studies in the Asymmetric Adjustable Nozzle of the Ames 6- by 6-Foot Supersonic Wind Tunnel. NACA RM A9E24, 1949.
2. Hall, Charles F., and Heitmeyer, John C.: Aerodynamic Study of a Wing-Fuselage Combination Employing a Wing Swept Back 63° .— Characteristics at Supersonic Speeds of a Model With the Wing Twisted and Cambered for a Uniform Load. NACA RM A9J24, 1950.
3. Silverstein, Abe, and White, James A.: Wind-Tunnel Interference with Particular Reference to Off-Center Positions of the Wing and to the Downwash at the Tail. NACA Rep. 547, 1935.
4. Herriot, John G.: Blockage Corrections for Three-Dimensional-Flow Closed-Throat Wind Tunnels, With Consideration of the Effect of Compressibility. NACA Rep. 995, 1947. (Formerly NACA RM A7B28)
5. Reese, David E., and Phelps, E. Ray: Lift, Drag, and Pitching Moment of Low-Aspect-Ratio Wings at Subsonic and Supersonic Speeds — Plane Tapered Wing of Aspect Ratio 3.1 With 3-Percent-Thick, Biconvex Section. NACA RM A50K28, 1951.

TABLE I.— MODEL DIMENSIONS

Wing	
Area, square inches	166.52
Aspect ratio	3.09
Taper ratio	0.389
Span, inches	22.69
Root section (at plane of symmetry) chord, feet	0.882
Thickness, percent of chord	4.5
Dihedral (wing reference plane), degrees	0
Incidence, degrees	0
Mean aerodynamic chord, inches	7.84
Sweepback (75-percent-chord line), degrees	0
Aileron	
Span, inches	3.16
Wing station at inboard end, inches	8.09
Wing station at outboard end, inches	11.26
Chord at inboard end, inches	1.49
Chord at outboard end, inches	1.04
Horizontal tail	
	Configuration A
Area, square inches	31.10
Area, exposed, square inches	24.48
Aspect ratio	3.05
Taper ratio	0.395
Span, inches	9.75
Root section	
Chord, inches	4.58
Thickness, percent of chord	7.5
Section at spanwise station, 1.70	
Chord, inches	3.61
Thickness, percent of chord	4.5
Tip section	
Chord, inches	1.84
Thickness, percent of chord	4.5
Dihedral, degrees	0
Incidence	variable
Mean aerodynamic chord, inches (based on total area).	3.40
Sweepback (50-percent-chord line), degrees	23

TABLE I.— CONCLUDED

Configuration B	
Area, square inches	43.06
Area, exposed, square inches	37.44
Aspect ratio	4.33
Taper ratio	0.409
Span, inches	13.67
Root section	
Chord, inches	4.48
Thickness, percent of chord	6.3
Tip section	
Chord, inches	1.84
Thickness, percent of chord	5.4
Dihedral, degrees	0
Incidence	variable
Mean aerodynamic chord, inches (based on total area)	3.34
Sweepback (50-percent-chord line), degrees	15
Vertical tail	
Area, square inches	23.62
Aspect ratio	1.32
Taper ratio	0.297
Span, inches	5.59
Root section	
Chord, inches	6.58
Thickness, percent of chord	4.5
Tip section	
Chord, inches	1.96
Thickness, percent of chord	4.5
Mean aerodynamic chord, inches	4.69
Sweepback (leading edge), degrees	45
Rudder	
Span, inches	3.54
Height of inboard end above horizontal tail reference plane, inches	0.91
Height of outboard end above horizontal tail reference plane, inches	4.52
Chord at inboard end, inches	1.98
Chord at outboard end, inches	1.09

TABLE II.- FIGURE INDEX

Longitudinal Stability and Control

	Horiz. tail configuration	Figure number for M=						
		0.60 to 0.93	1.30	1.40	1.50	1.60	1.70	1.91
C_L vs α	A	6(a), 7(a)	10(a)	11(a)	12(a)	13(a)	14(a)	15(a)
	B	8(a), 9(a)	16(a)	---	---	17(a)	---	18(a)
C_m vs C_L	A	6(b), 7(b)	10(b)	11(b)	12(b)	13(b)	14(b)	15(b)
	B	8(b), 9(b)	16(b)	---	---	17(b)	---	18(b)
C_D vs C_L	A	6(c), 7(c)	10(c)	11(c)	12(c)	13(c)	14(c)	15(c)
	B	8(c), 9(c)	16(c)	---	---	17(c)	---	18(c)
C_h vs C_L	A	---	10(d)	11(d)	12(d)	13(d)	14(d)	15(d)
	B	---	16(d)	---	---	17(d)	---	18(d)

Directional and Lateral Stability

	Figure number for M=		
	0.90	1.40	1.91
C_n vs β	26(a)	27(a)	28(a)
C_Y vs β	26(b)	27(b)	28(b)
C_l vs β	26(c)	27(c)	28(c)
C_L vs β	---	33	---
C_m vs β	---	33	---
C_D vs β	---	33	---

Directional and Lateral Control
(M = 1.40 only)

	Figure number for $\alpha=$		
	0°	5°	10°
C_n vs β	30(a)	31(a)	32(a)
C_Y vs β	30(b)	31(b)	32(b)
C_l vs β	30(c)	31(c)	32(c)
C_l vs C_L	34		

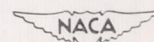


TABLE III.- SUMMARY OF PRESSURE DATA

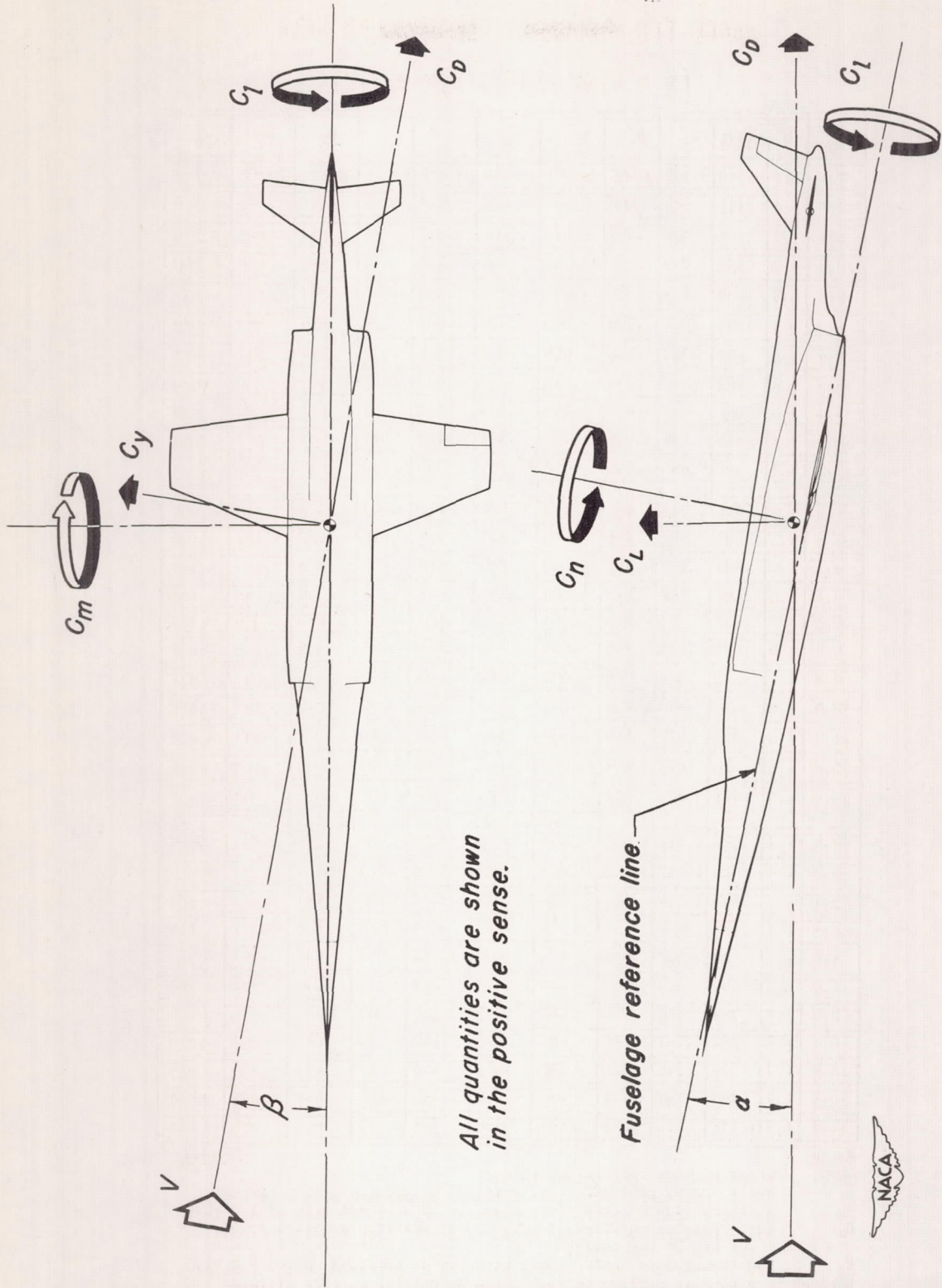
$$[R = 2.09 \times 10^6; E = 0.779]$$

α (deg)	M	$\Delta H/q$	P_1	P_2	P_b	P_3	P_4	P_5	P_6	P_7	P_8
-4.4	1.3	.115	.924	.866	-.081	-.014	-.028	0	-.031	-.180	-.100
-2.3	1.3	.111	.924	.866	-.077	-.014	-.028	0	-.031	-.180	-.100
-.1	1.3	.164	.866	.808	-.077	-.001	-.014	.018	-.013	-.091	-.086
2.1	1.3	.203	.839	.791	-.067	.012	.003	.036	.005	-.068	-.068
4.3	1.3	.234	.839	.786	-.058	.048	.048	.045	.027	-.042	-.037
6.5	1.3	.247	.822	.769	-.058	.052	.061	.040	.040	-.020	-.015
8.7	1.3	.256	.760	.751	-.054	.061	.078	.036	.053	.011	.011
10.9	1.3	.287	.760	.733	-.045	.070	.096	.031	.058	.038	.029
13.1	1.3	.384	.729	.672	-.058	.070	.096	.009	.058	.069	.038
15.3	1.3	.415	.694	.636	-.080	.074	.109	-.035	.049	.077	.047
17.5	1.3	.520	.645	.592	-.116	.087	.140	-.039	.080	.069	.033
-4.5	1.5	.204	1.016	.961	-.102	-.006	-.010	.003	-.018	-.170	-.254
-2.3	1.5	.234	.991	.936	-.089	.007	.003	.016	-.005	-.183	-.178
-.1	1.5	.284	.936	.886	-.093	.007	.003	.020	.003	-.187	-.120
2.1	1.5	.384	.861	.815	-.089	.015	.015	.024	.008	-.149	-.108
4.3	1.5	.396	.857	.812	-.081	.024	.036	.033	.020	-.112	-.103
6.4	1.5	.425	.836	.782	-.081	.036	.049	.024	.028	-.070	-.083
8.7	1.5	.471	.803	.728	-.081	.045	.065	.016	.033	-.033	-.041
10.8	1.5	.580	.728	.699	-.077	.049	.074	.008	.037	-.012	-.028
13.0	1.5	.663	.674	.624	-.072	.049	.090	-.018	.037	.013	-.008
15.2	1.5	.684	.653	.603	-.072	.049	.103	-.043	.037	.009	.013
17.4	1.5	.701	.665	.615	-.114	.061	.128	-.097	.041	.009	-.024
-4.4	1.7	.396	1.111	1.056	-.094	.005	.001	.002	-.010	-.067	-.208
-2.2	1.7	.421	1.077	1.015	-.082	.010	.005	.015	-.005	-.133	-.217
-.1	1.7	.505	1.004	.941	-.082	.022	.018	.019	.011	-.155	-.205
2.1	1.7	.629	.898	.861	-.086	.018	.018	.019	.011	-.171	-.200
4.2	1.7	.658	.882	.840	-.077	.026	.039	.023	.019	-.167	-.150
6.4	1.7	.687	.857	.811	-.077	.035	.047	.015	.015	-.146	-.108
8.5	1.7	.762	.798	.752	-.082	.043	.060	.002	.027	-.121	-.084
10.7	1.7	.808	.723	.732	-.082	.043	.068	-.019	.027	-.088	-.075
12.9	1.7	.719	.876	.826	-.098	.043	.076	-.027	.027	-.058	-.067
15.1	1.7	.798	.797	.751	-.098	.039	.089	-.044	.027	-.063	-.054
17.3	1.7	1.135	.535	.502	-.127	.039	.101	-.073	.027	.004	-.021

Notes:

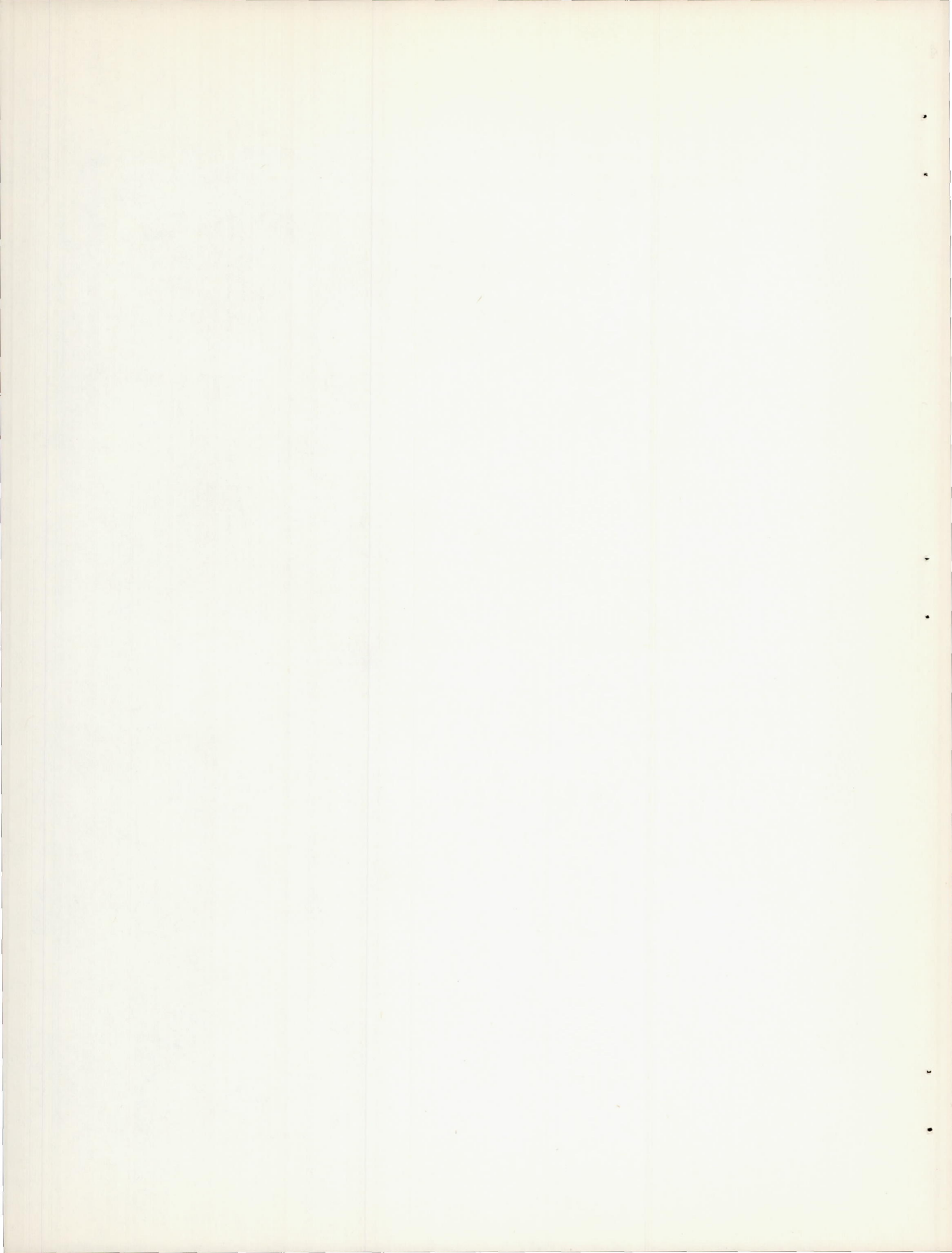
- $\Delta H/q$ pressure-loss coefficient in duct
 P_1 static-pressure coefficient measured on inboard side of air duct
 P_2 static-pressure coefficient measured on outboard side of air duct
 P_b base-pressure coefficient measured at orifices provided around the rim of the outlet
 P_3 static-pressure coefficients measured at orifices on the fuselage, through subscript numbers corresponding to orifice numbers given on figure 4 of this report

NACA



All quantities are shown in the positive sense.

Figure 1.- Sign convention.



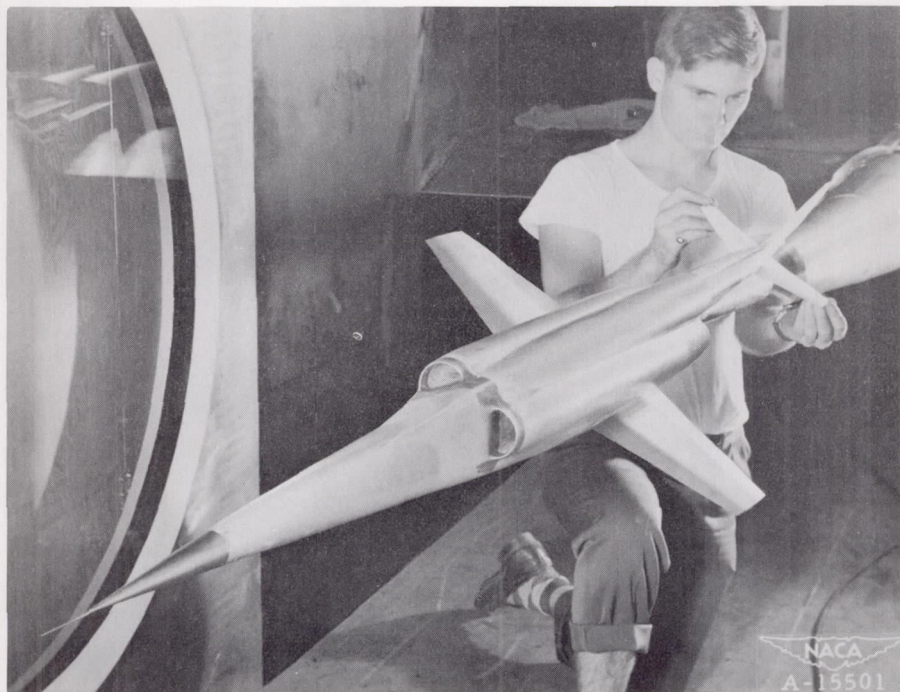
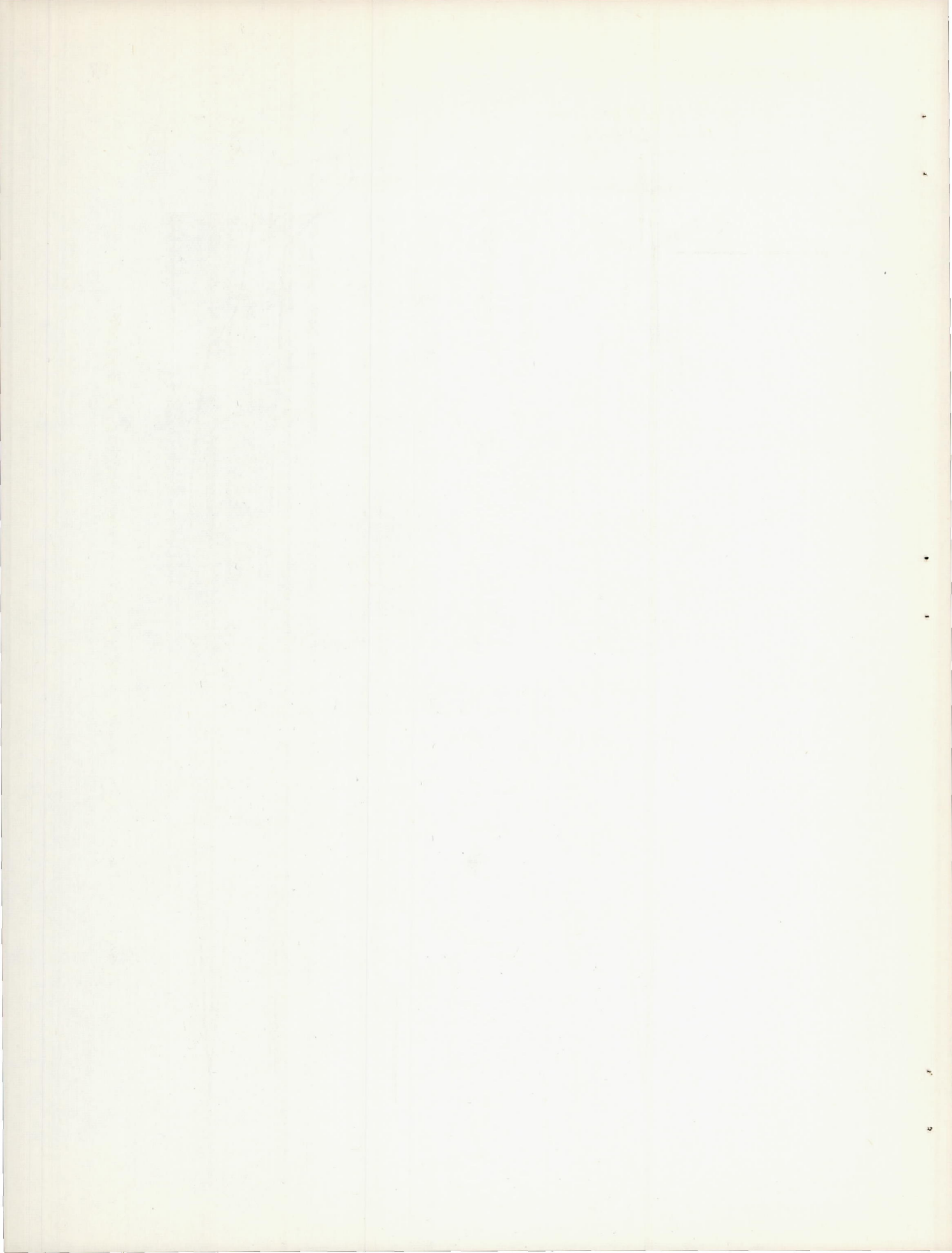
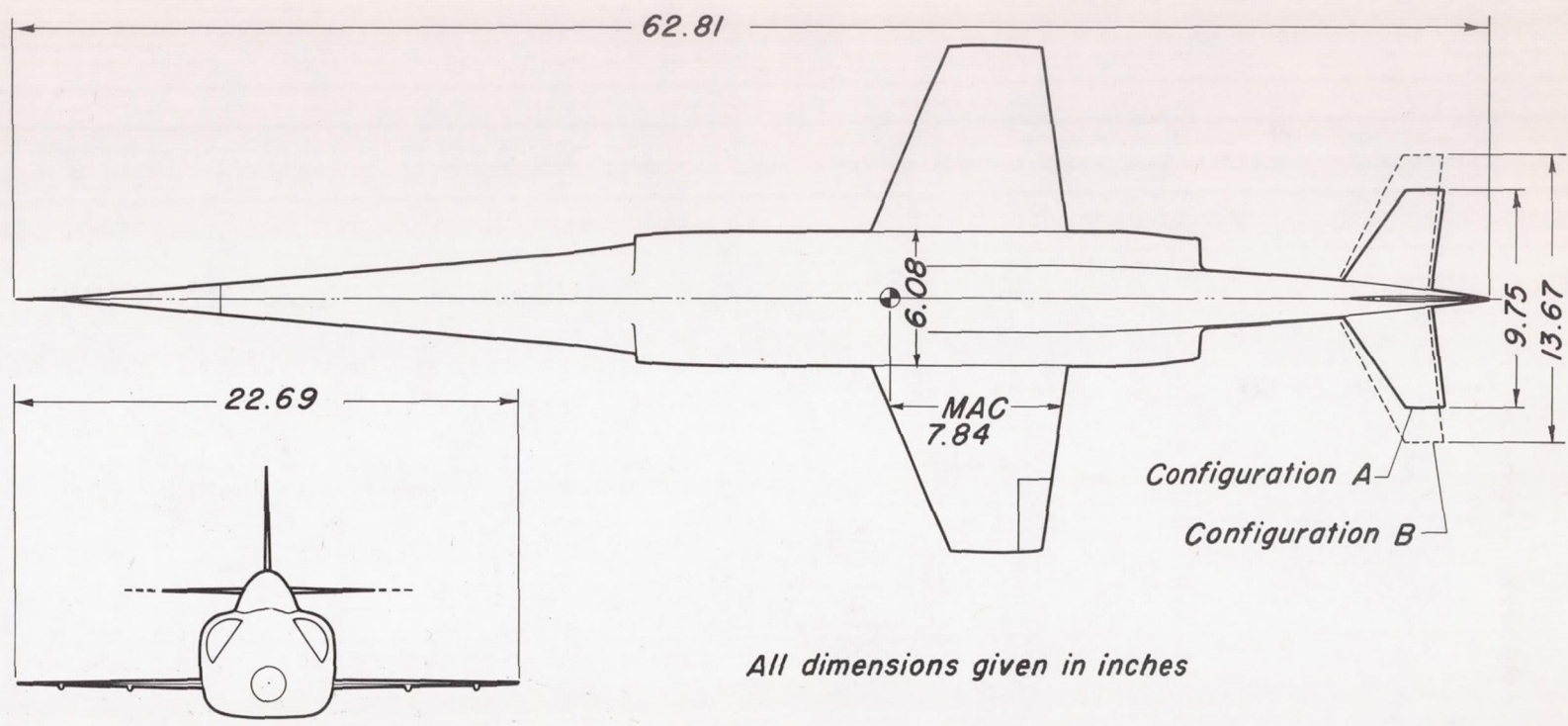


Figure 2.- The 1/12-scale Douglas X-3 model mounted in the 6- by 6-foot supersonic wind tunnel.





All dimensions given in inches

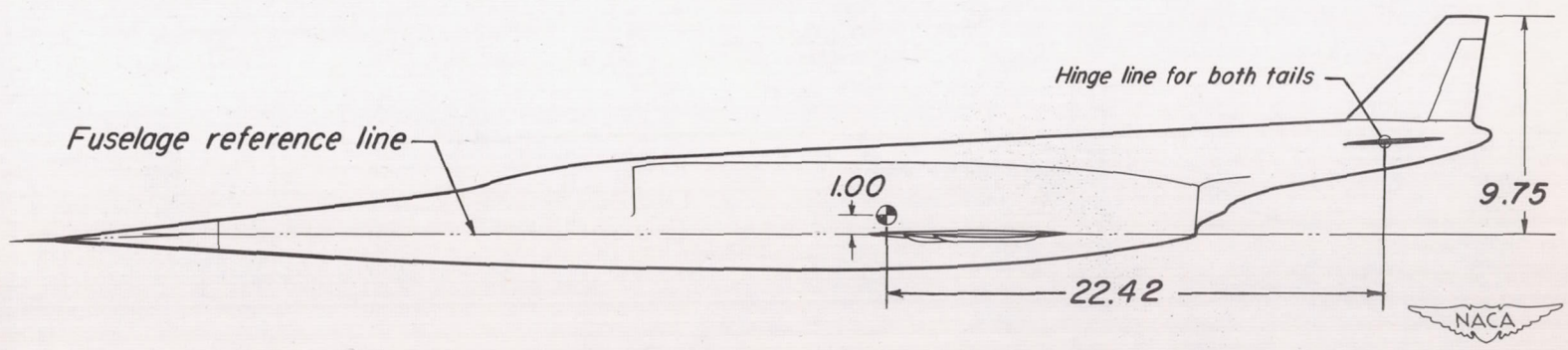


Figure 3.- Three-view drawing of the 1/12-scale Douglas X-3 model.

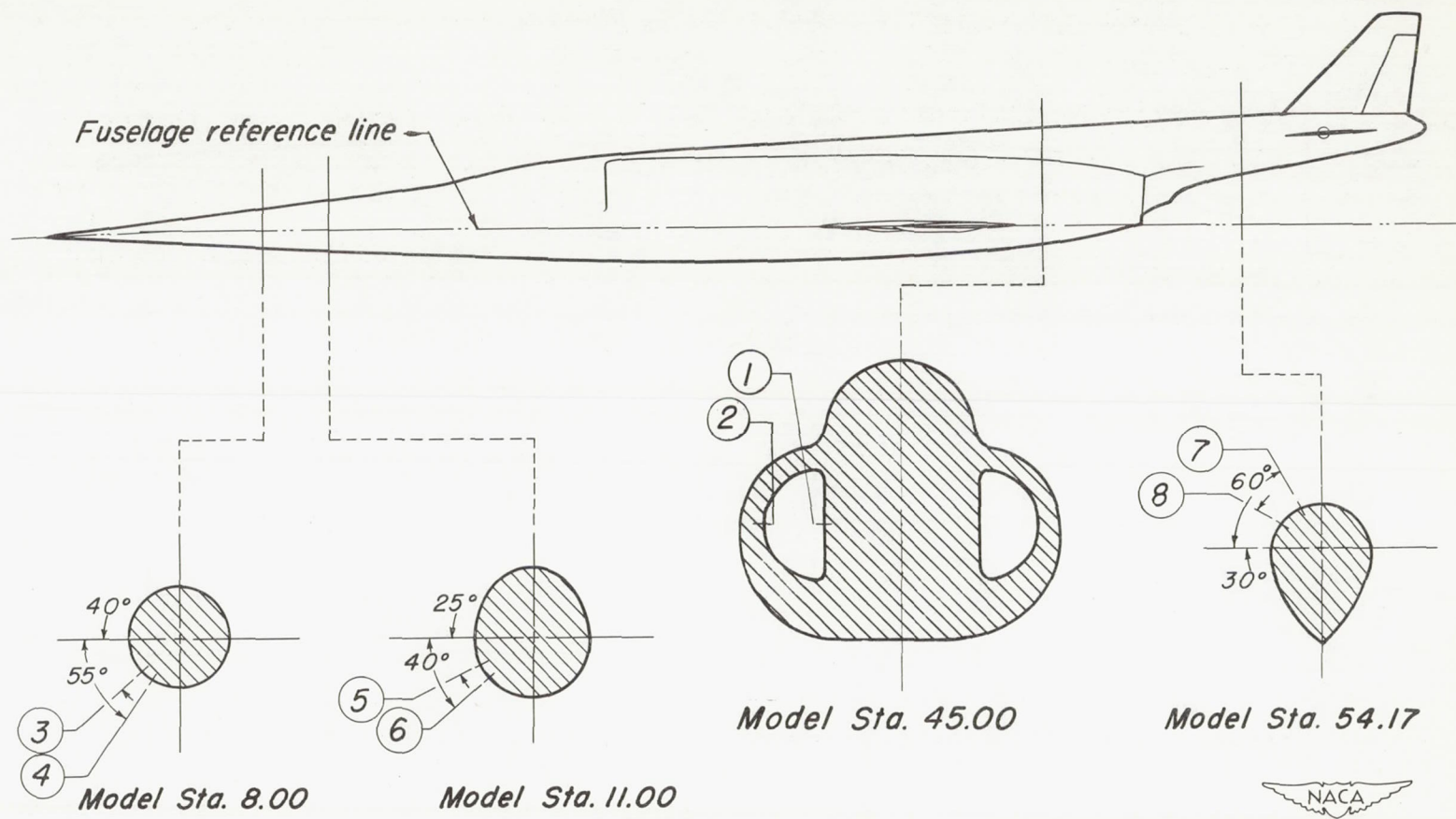


Figure 4.- Location of pressure orifices on fuselage of 1/12-scale Douglas X-3 model.

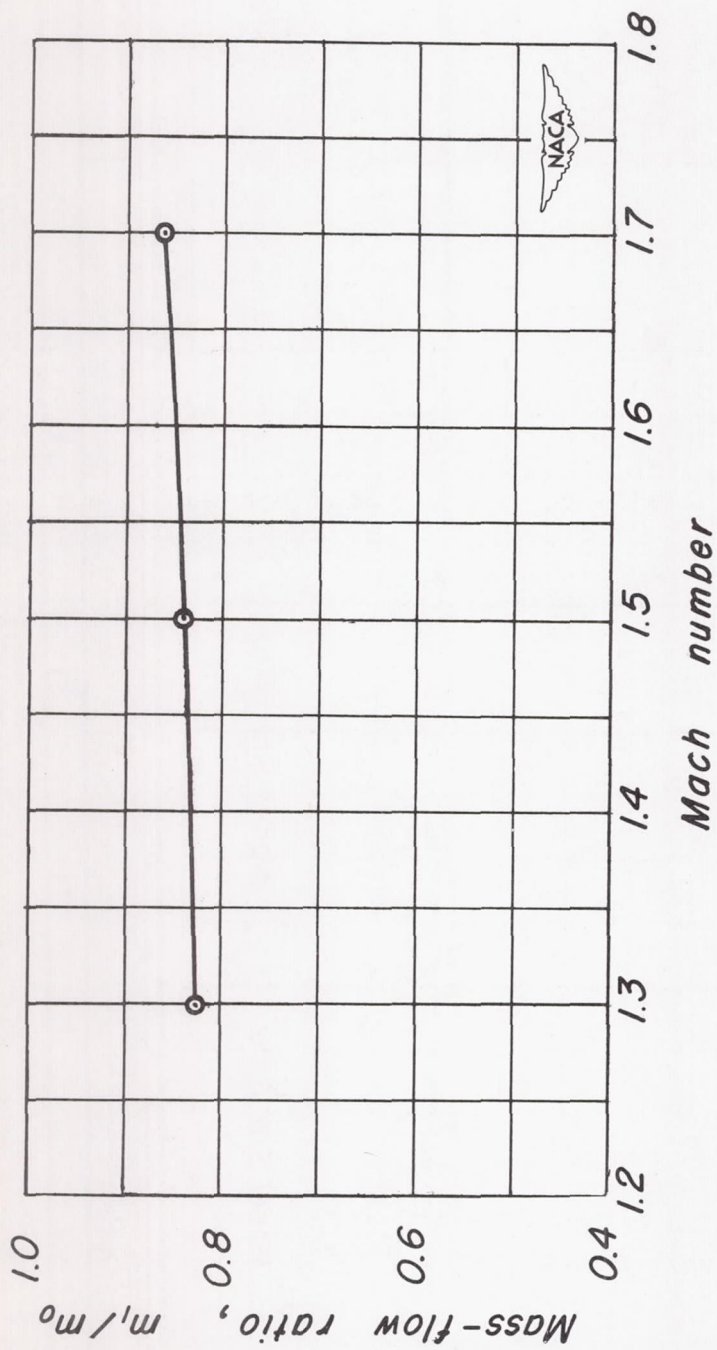


Figure 5.- Mass-flow ratio vs. Mach number relationship. $E=779$.

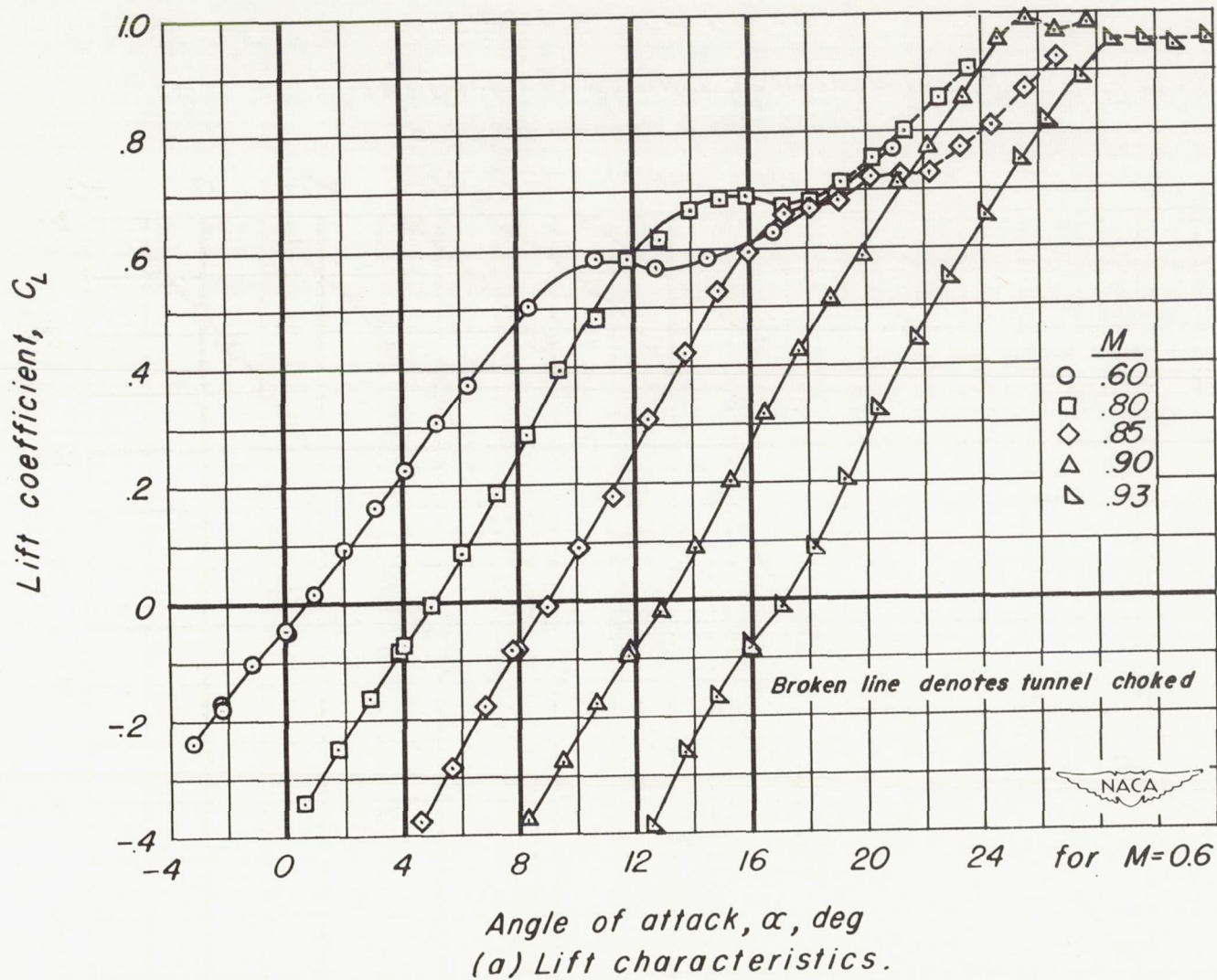


Figure 6.- Subsonic longitudinal stability and control characteristics of the 1/12-scale Douglas X-3 configuration A. $R = 2.61 \times 10^6$; $i_t = 0^\circ$

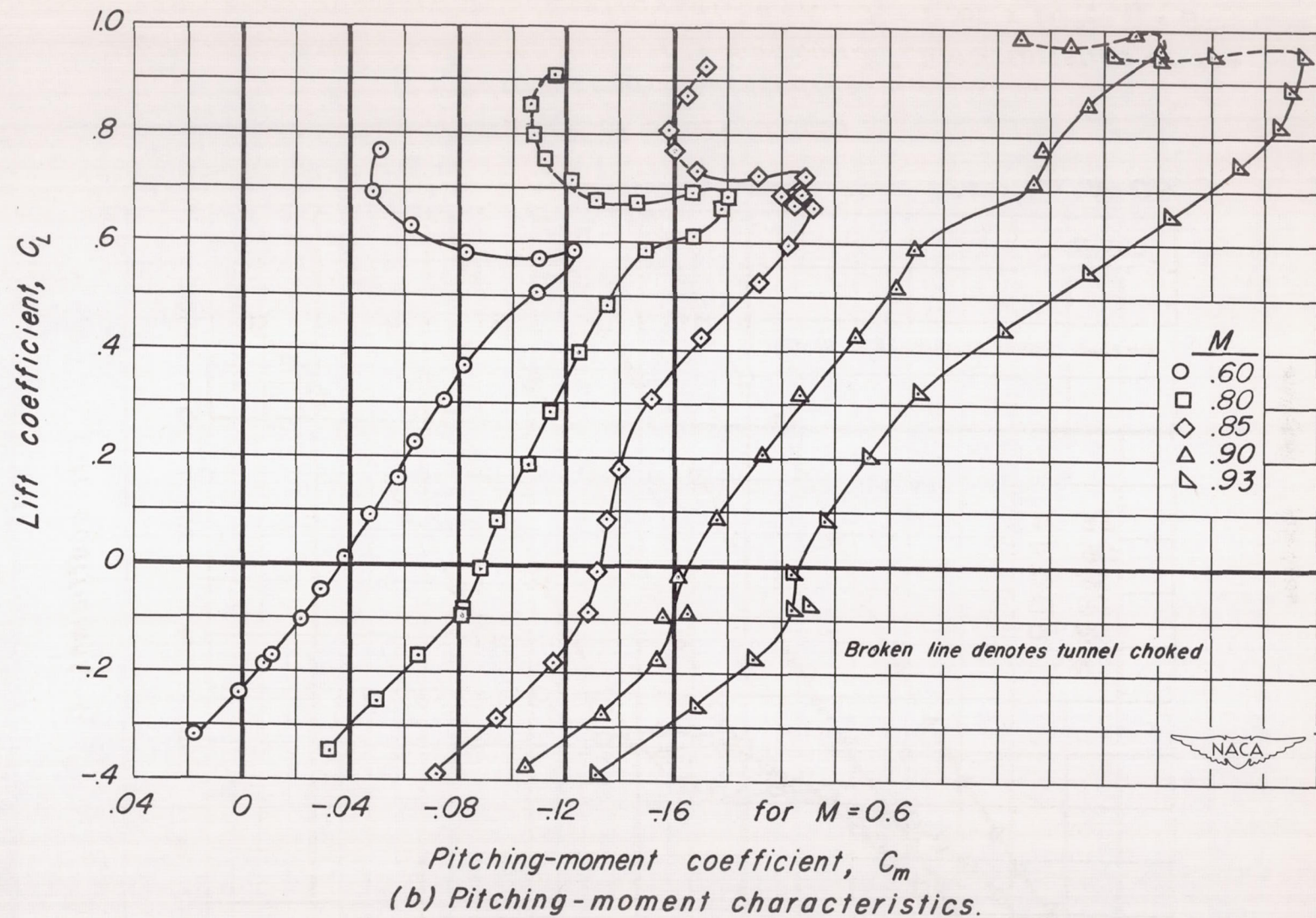
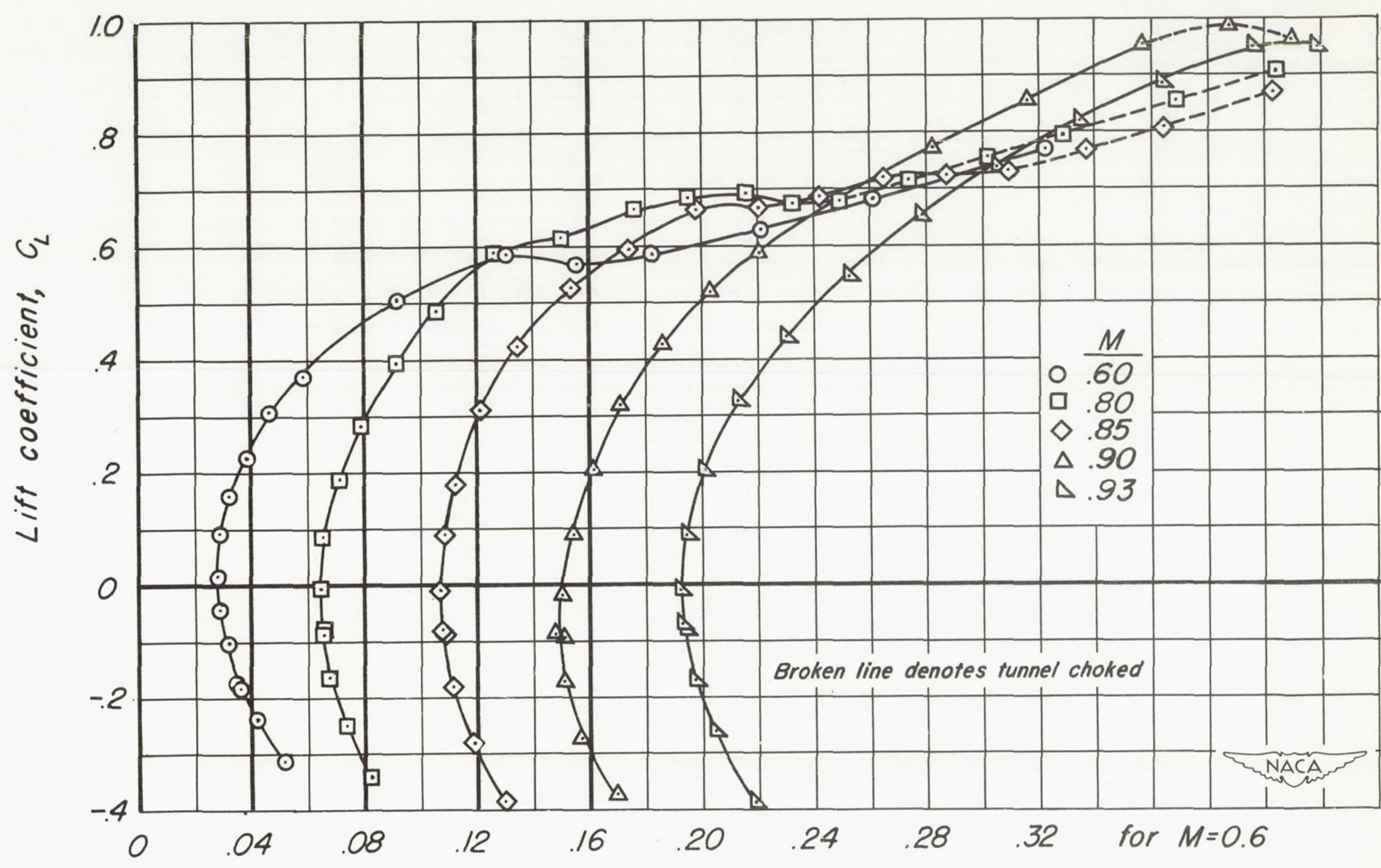


Figure 6.- Continued.



(c) Drag characteristics.

Figure 6.- Concluded.

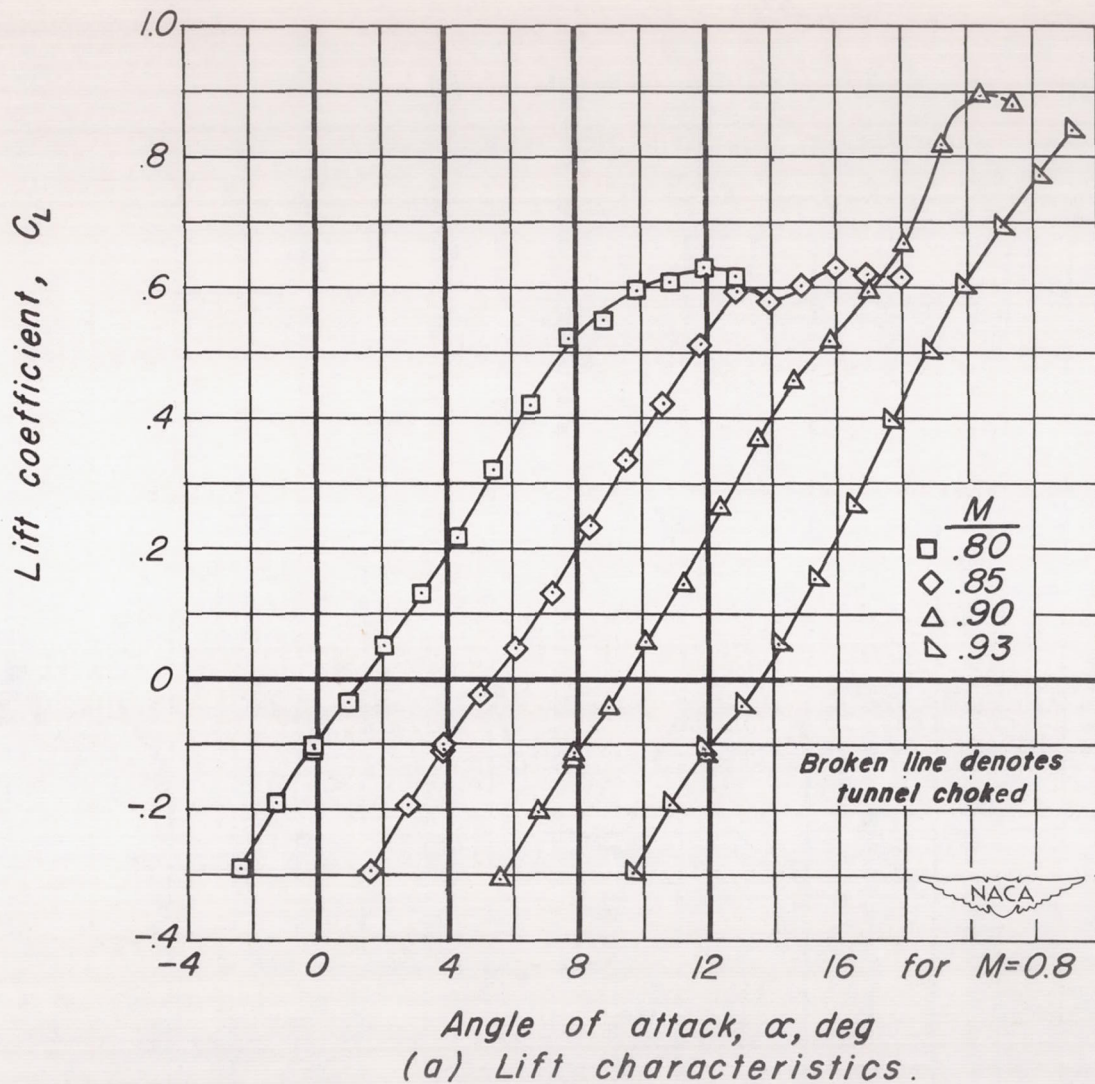
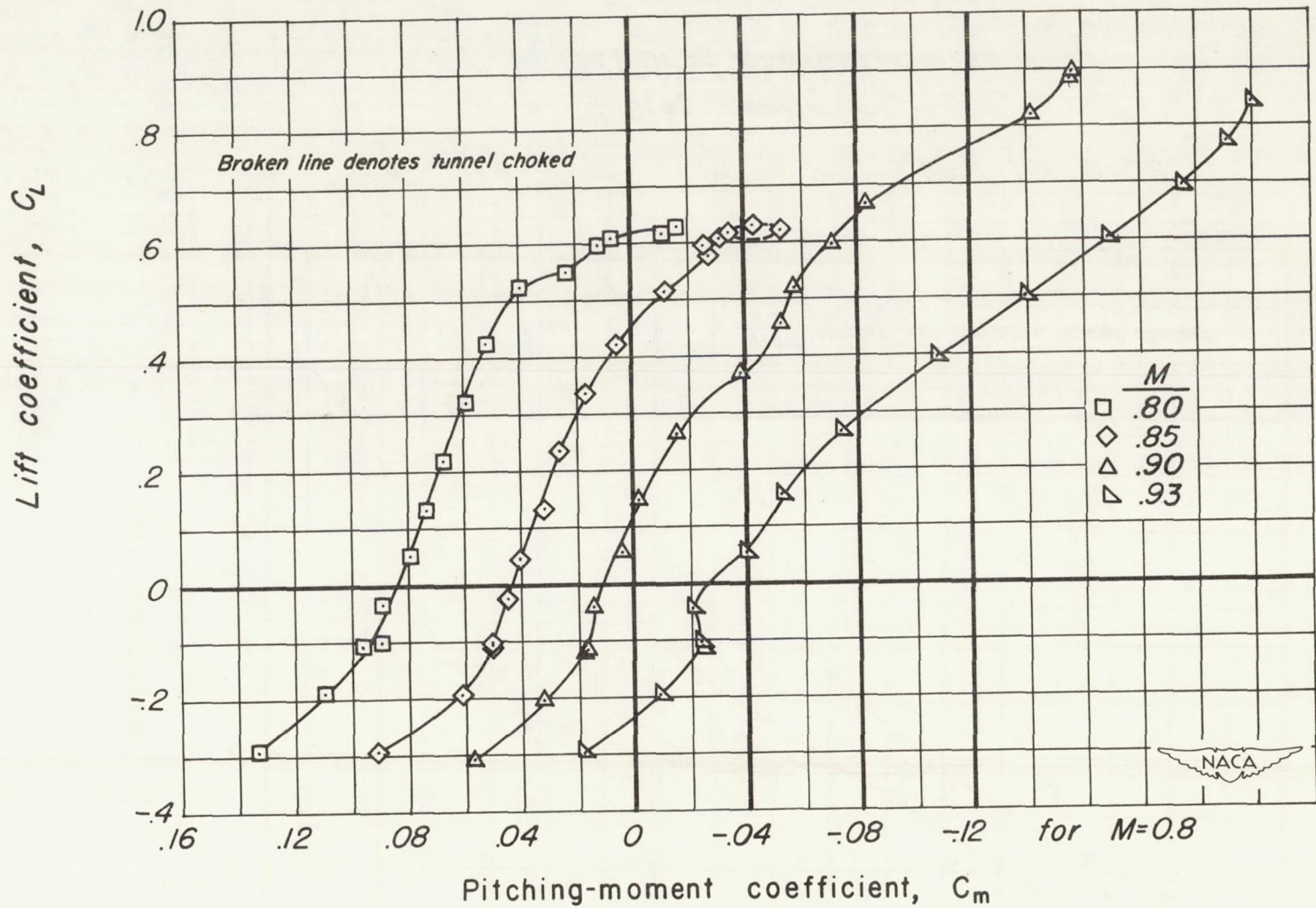
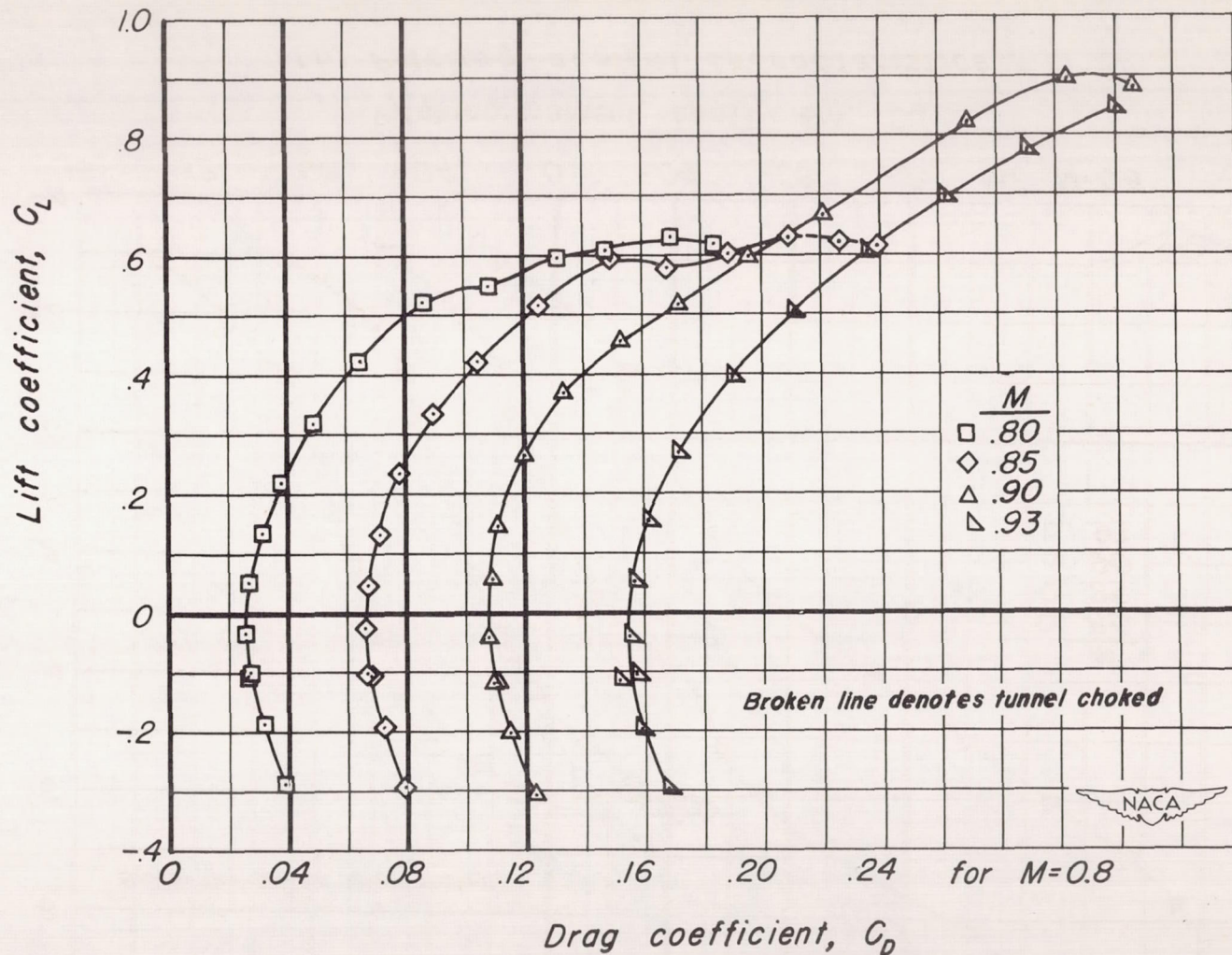


Figure 7.- Subsonic longitudinal stability and control characteristics of the 1/12-scale Douglas X-3 configuration A. $R = 2.61 \times 10^6$; $i_t = -4.6^\circ$.



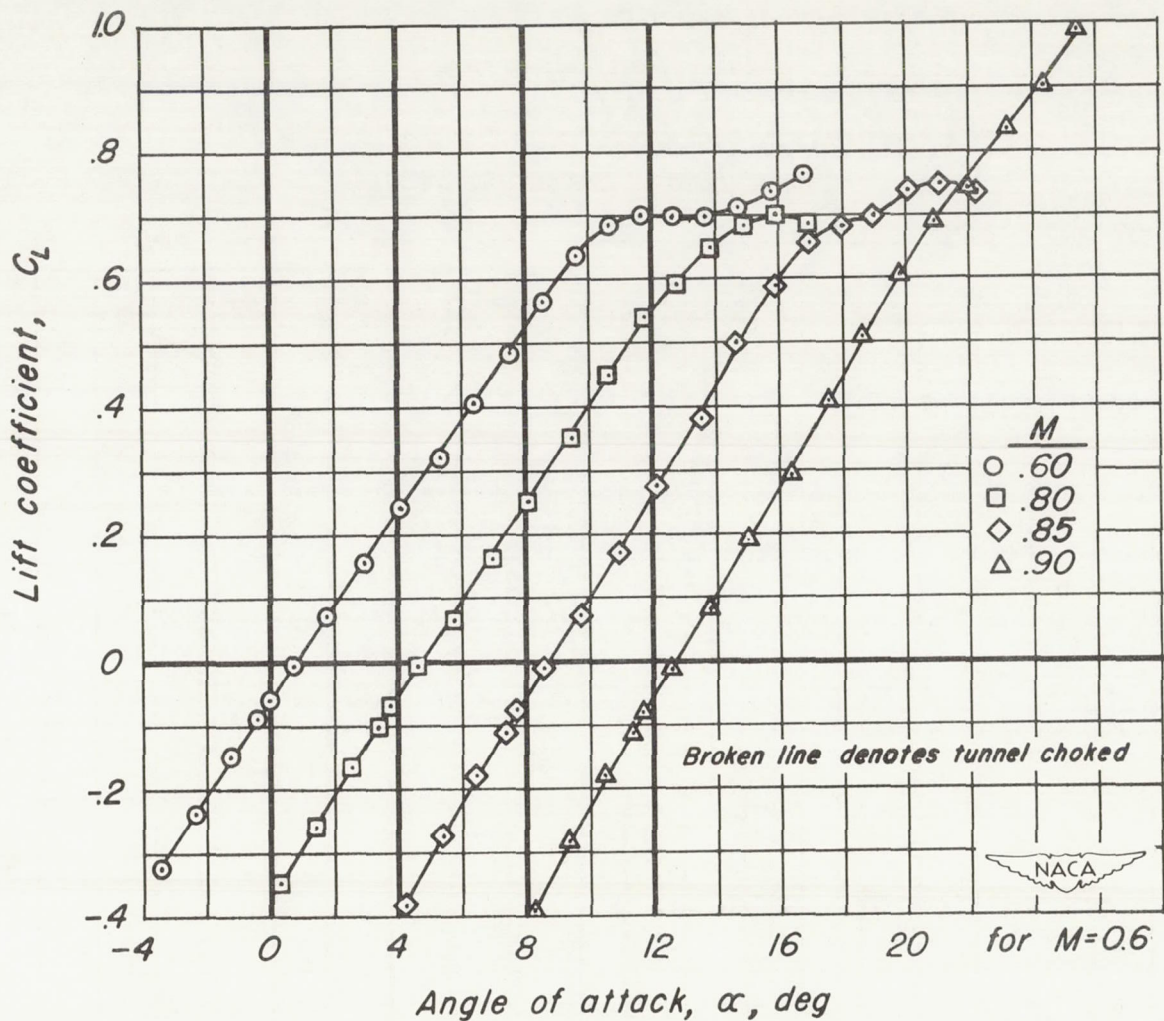
(b) Pitching-moment characteristics.

Figure 7.- Continued.



Drag coefficient, C_D
 (c) Drag characteristics.

Figure 7. - Concluded.



(a) Lift characteristics.
 Figure 8.- Subsonic longitudinal stability and control characteristics of the 1/12-scale Douglas X-3 configuration B. $R = 2.61 \times 10^6$; $i_1 = 0^\circ$.

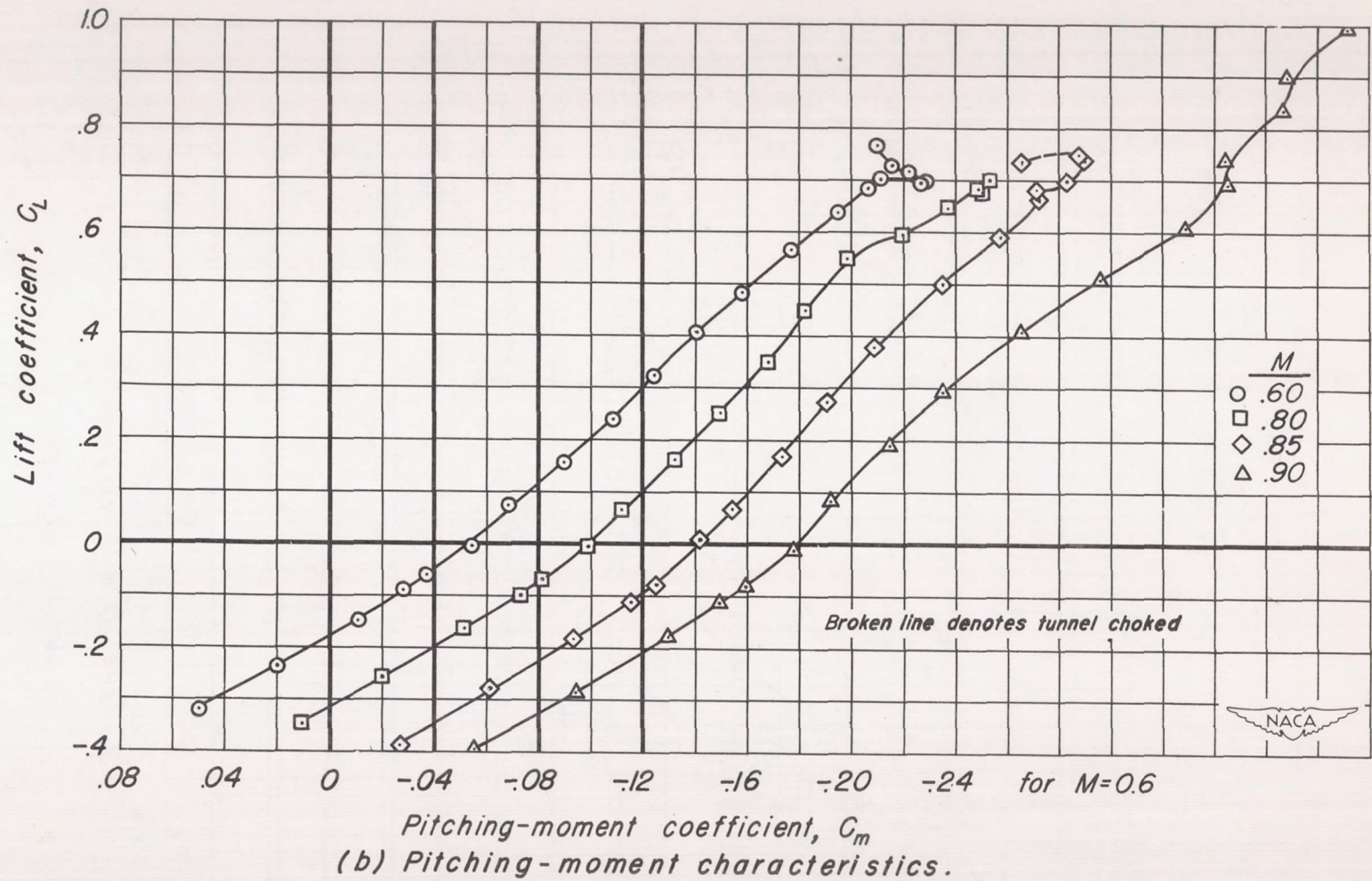
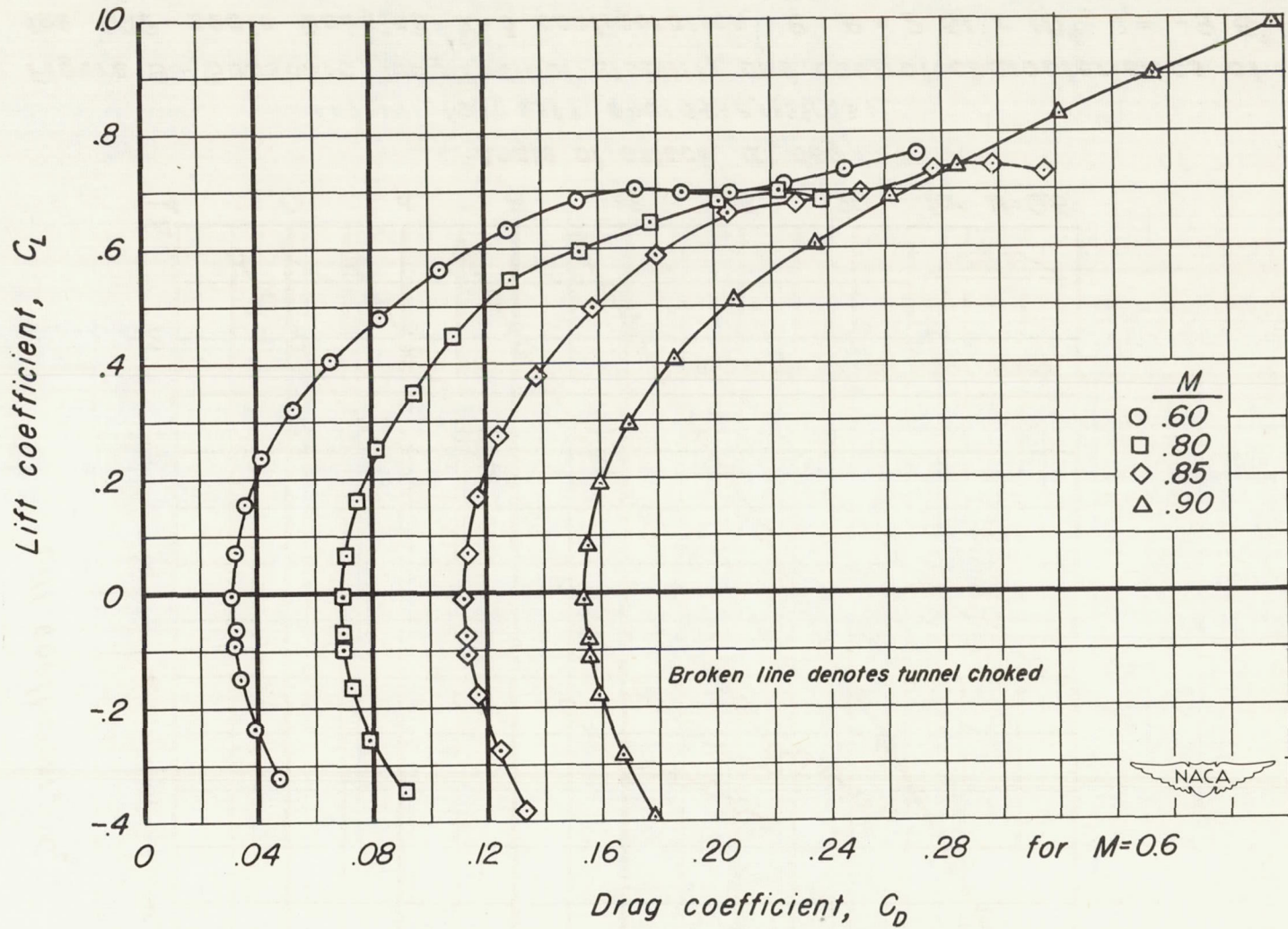
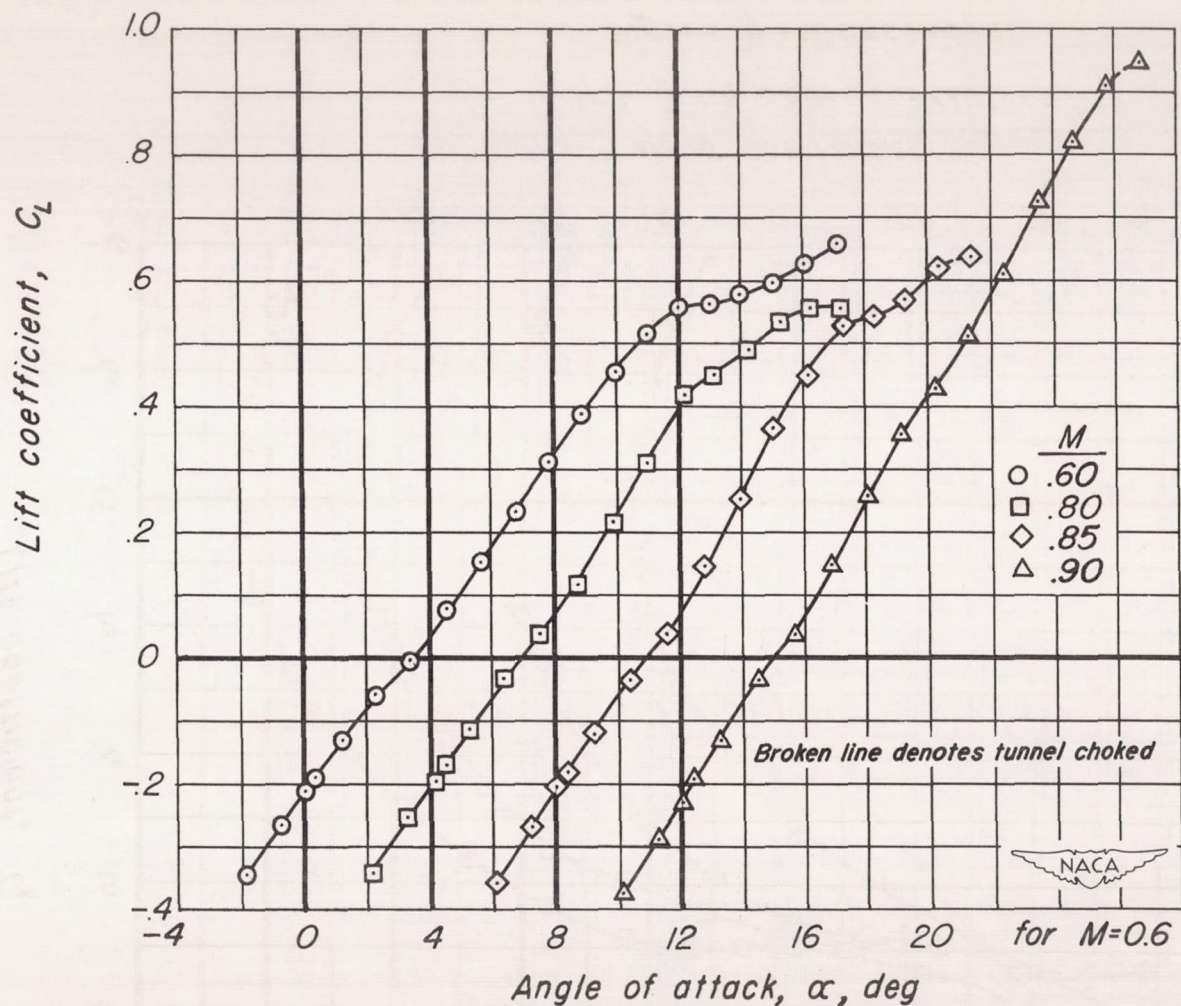


Figure 8.- Continued.



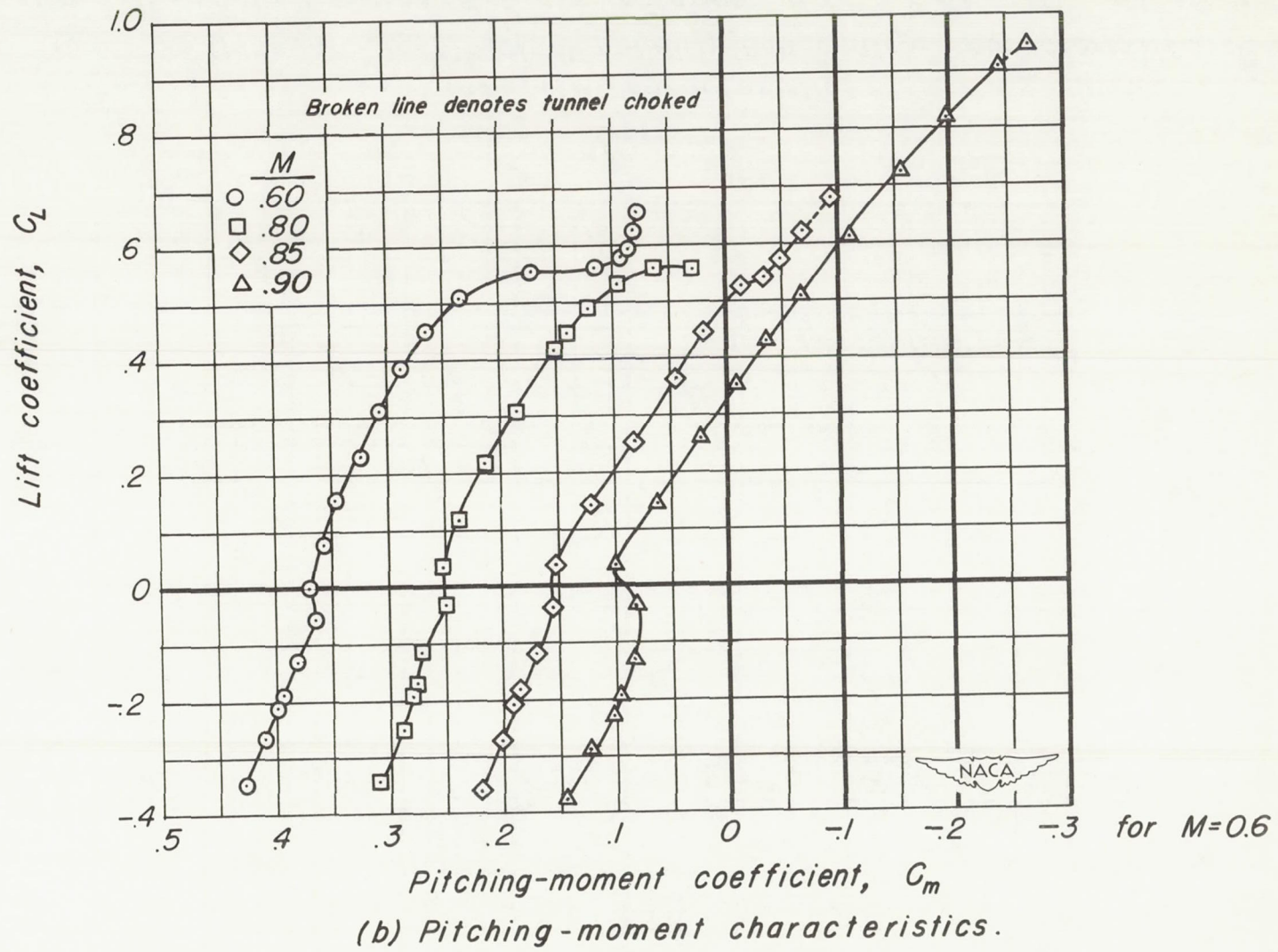
(c) Drag characteristics.

Figure 8.- Concluded.



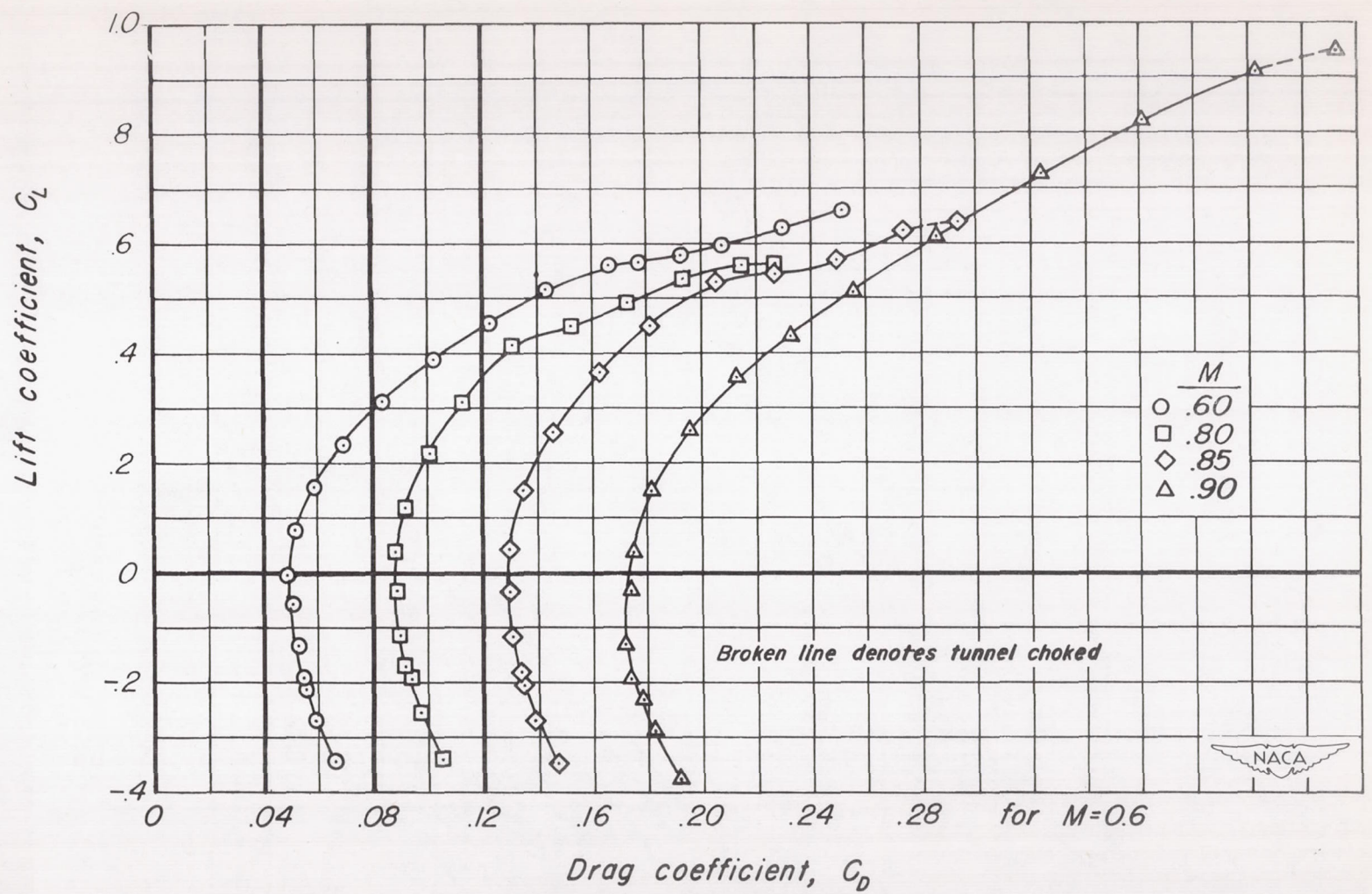
(a) Lift characteristics.

Figure 9.- Subsonic longitudinal stability and control characteristics of the 1/12-scale Douglas X-3 configuration $B.R = 2.61 \times 10^6$; $i_t = -9.6^\circ$.



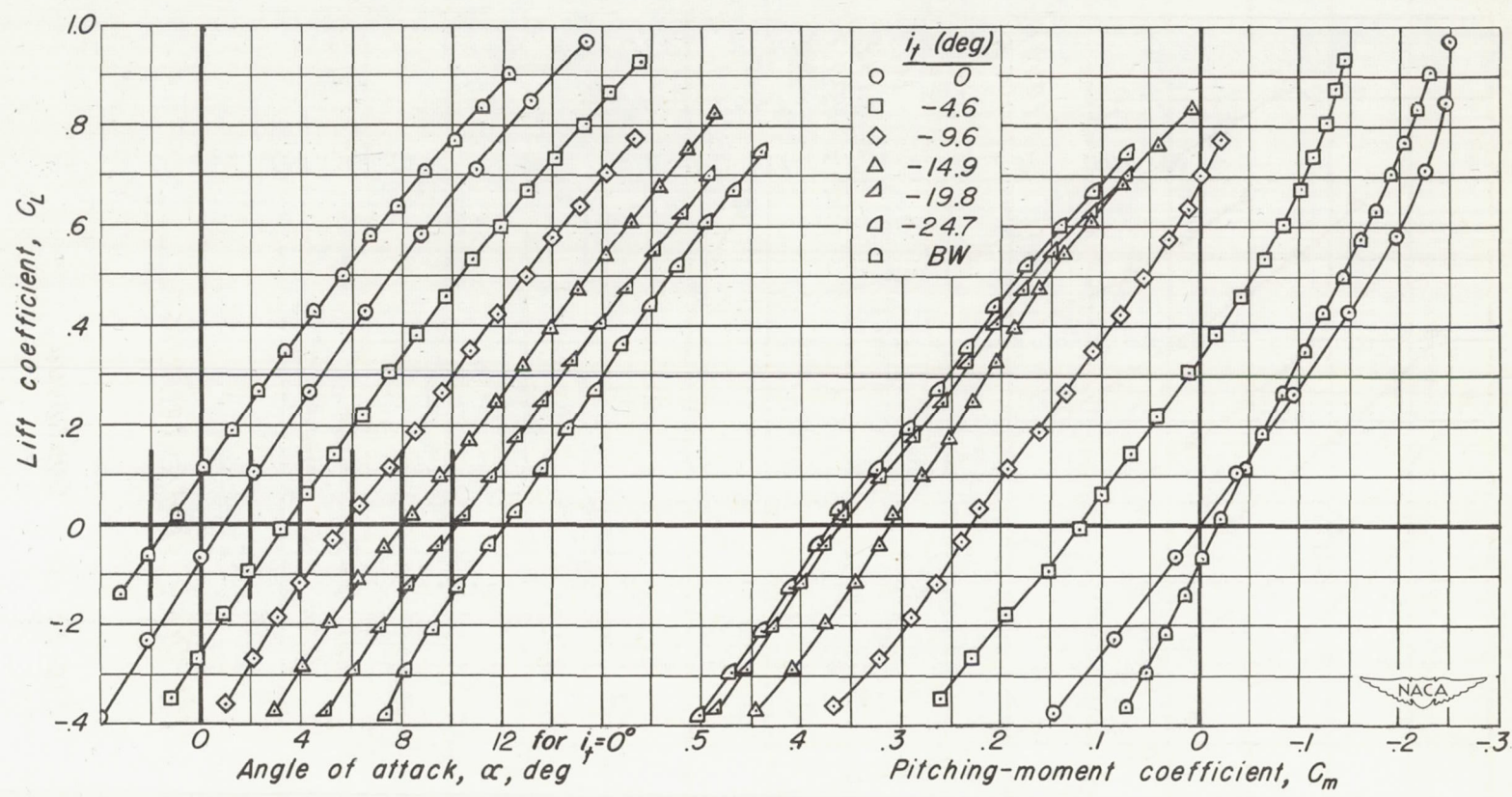
(b) Pitching-moment characteristics.

Figure 9.- Continued.



(c) Drag characteristics.

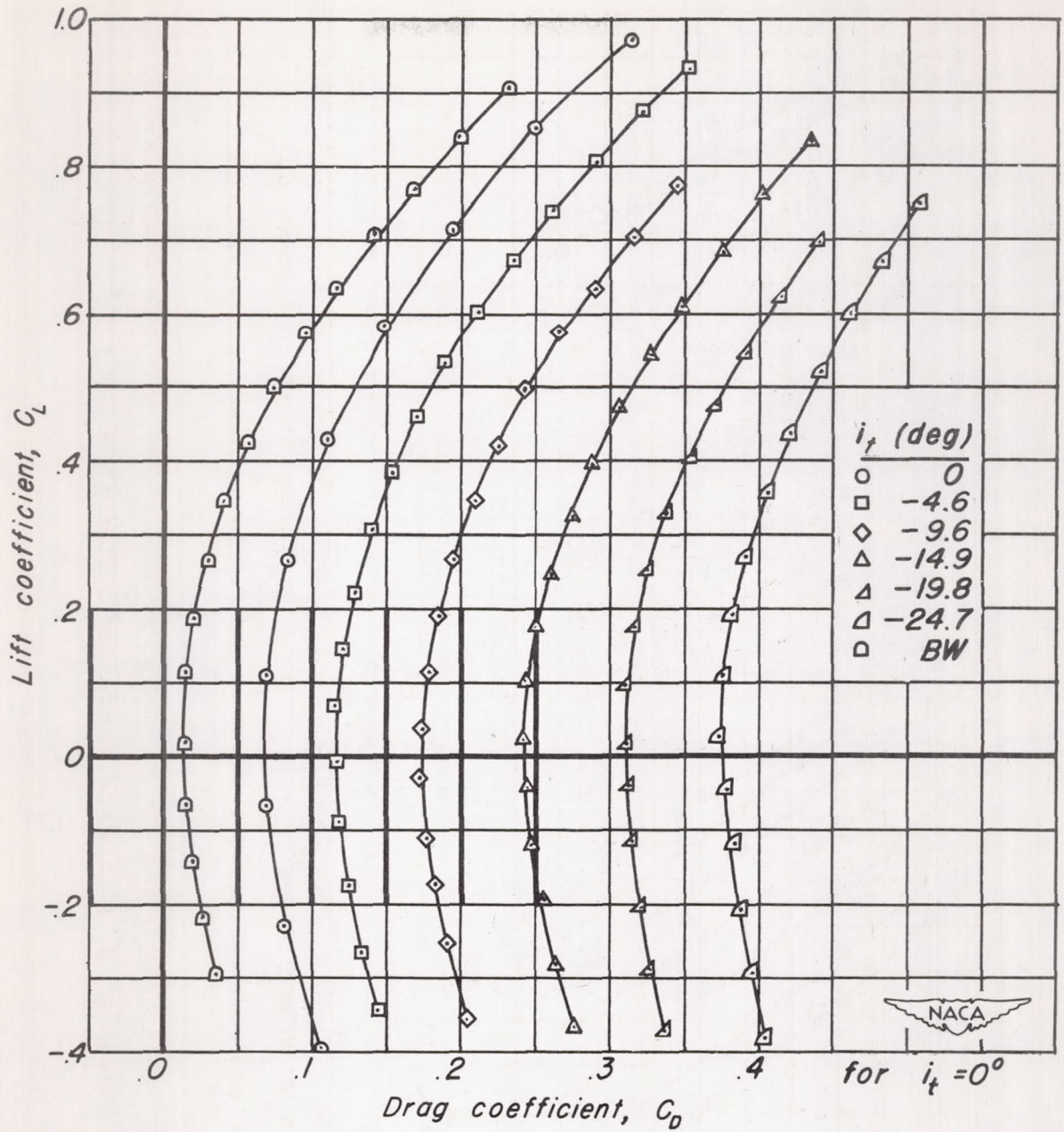
Figure 9.- Concluded.



(a) Lift characteristics.

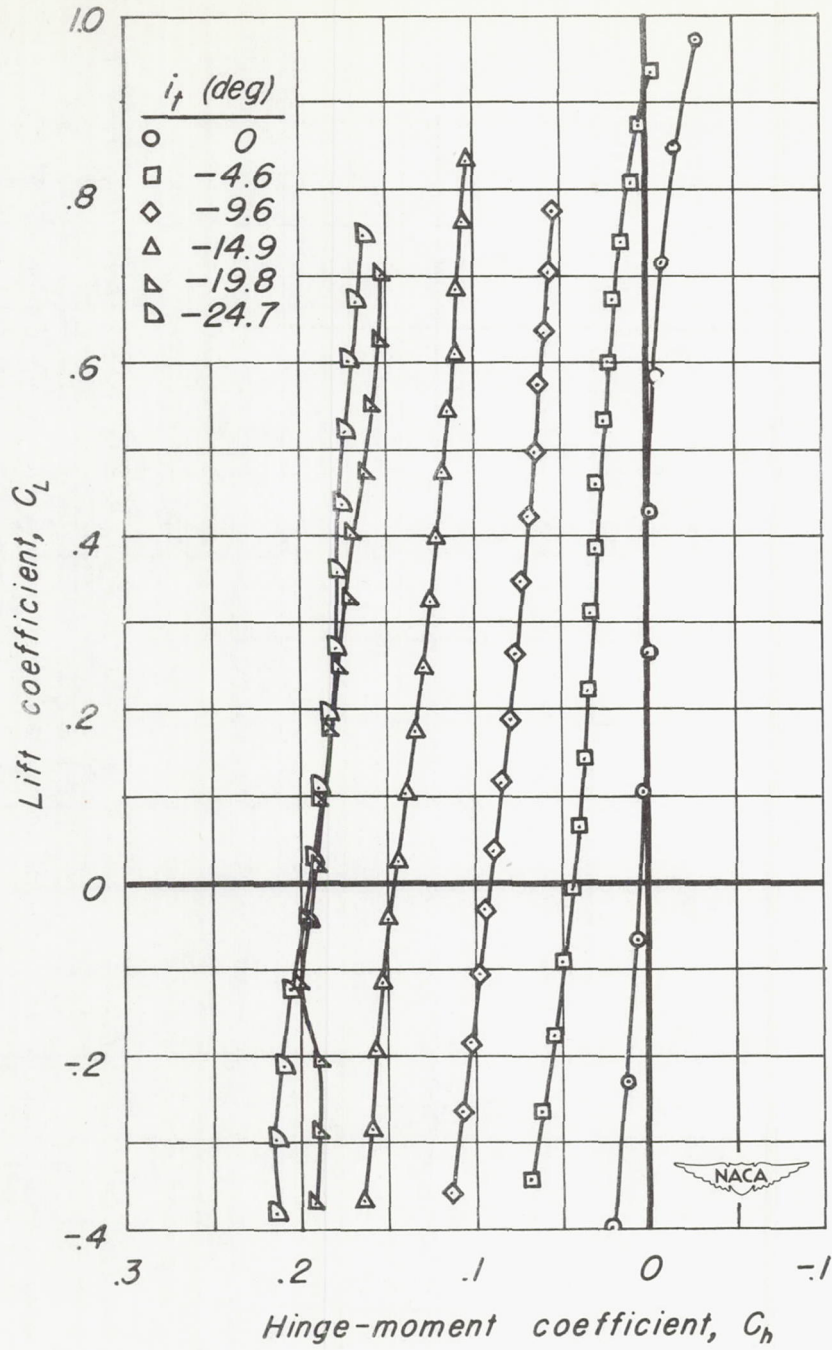
(b) Pitching-moment characteristics.

Figure 10. - Longitudinal stability and control characteristics of the 1/12-scale Douglas X-3 configuration A at a Mach number of 1.30. $R = 2.09 \times 10^6$.



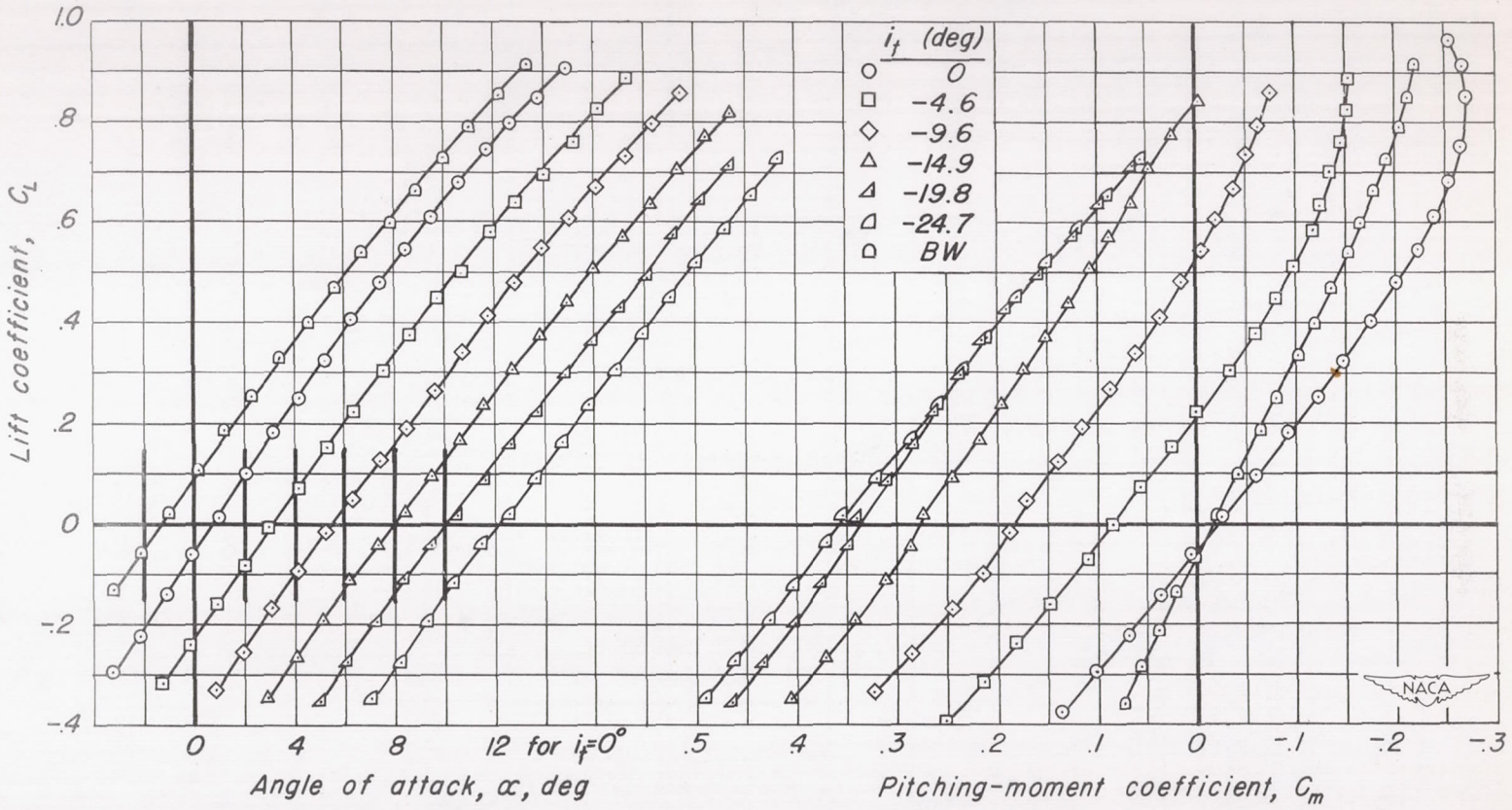
(c) Drag characteristics.

Figure 10. - Continued.



(d) Hinge-moment characteristics.

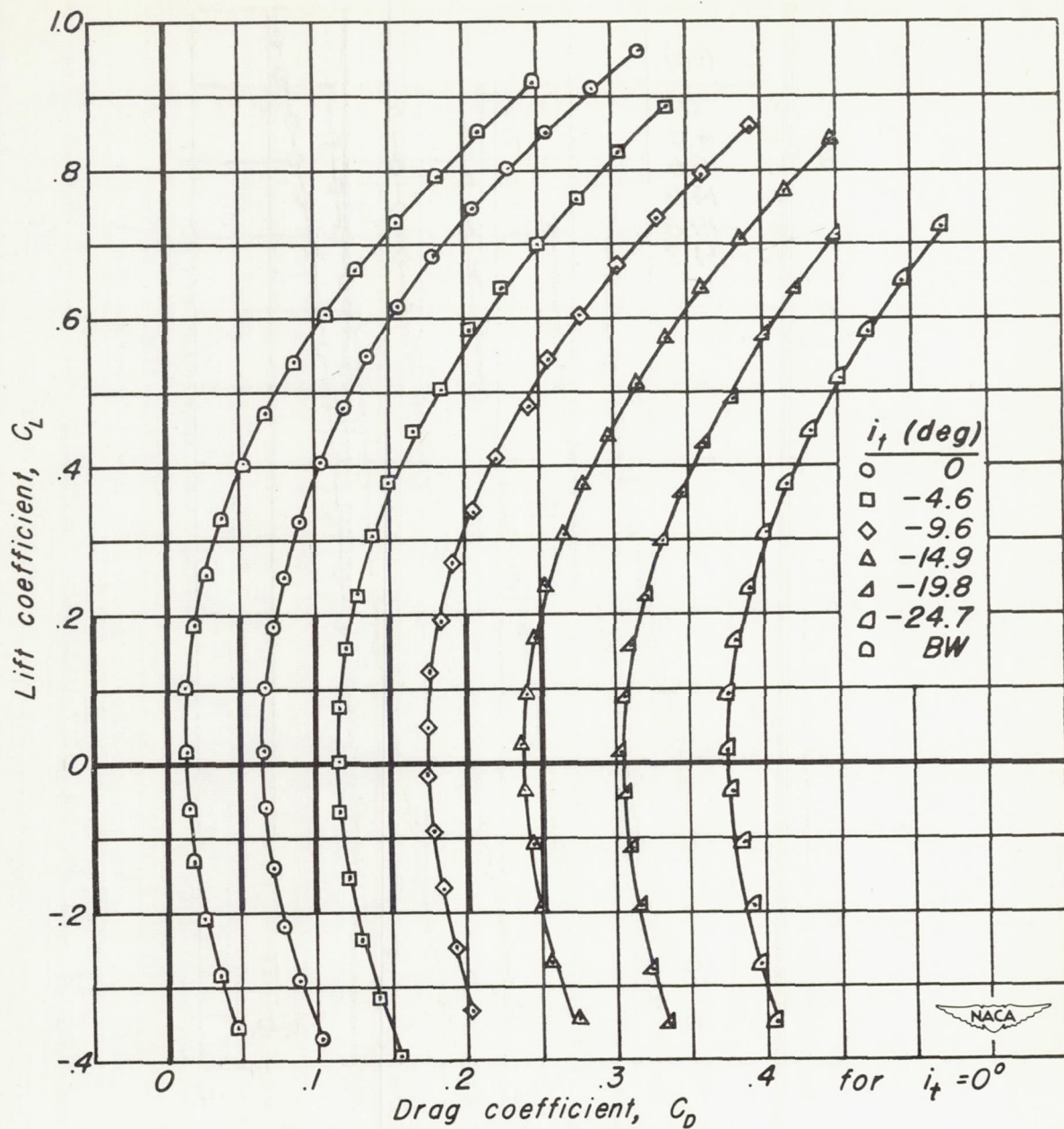
Figure 10.- Concluded.



(a) Lift characteristics.

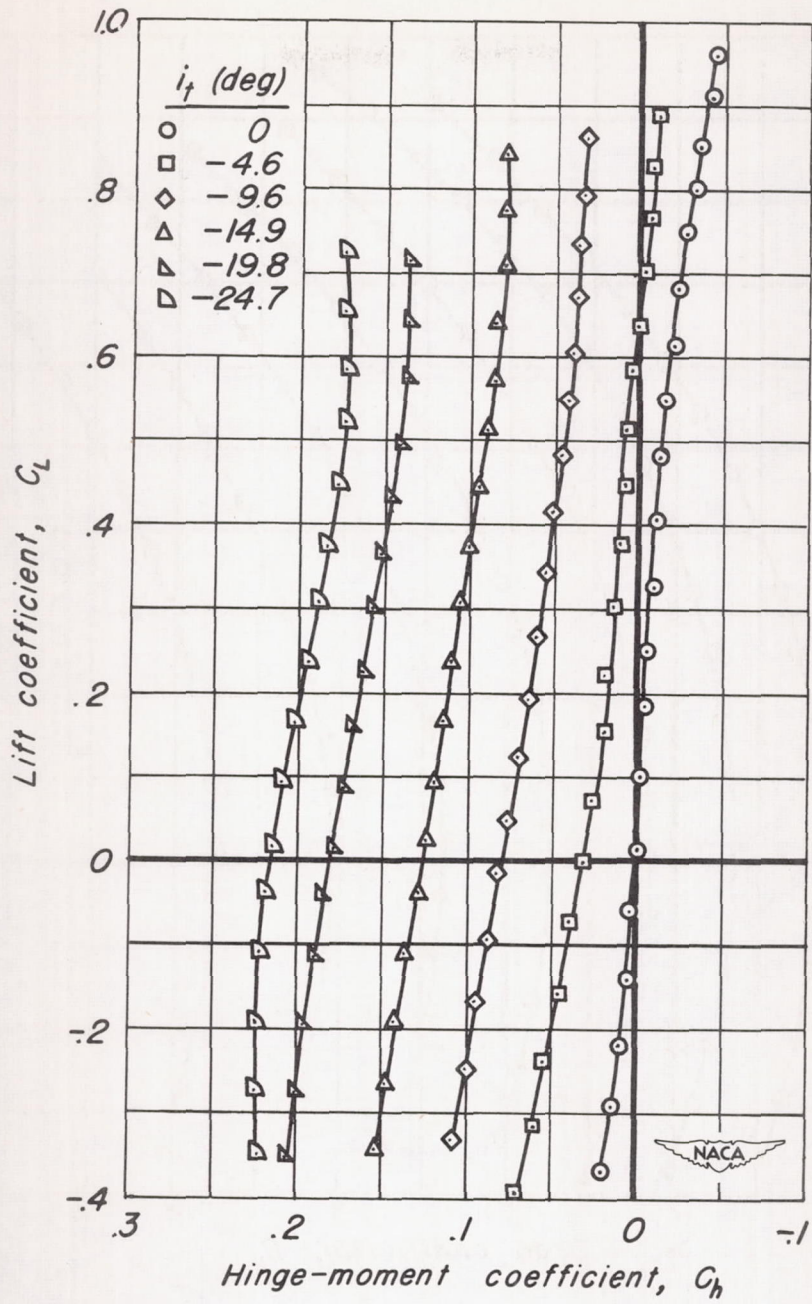
(b) Pitching-moment characteristics.

Figure 11.- Longitudinal stability and control characteristics of the 1/12-scale Douglas X-3 configuration A at a Mach number of 1.40. $R = 2.09 \times 10^6$.



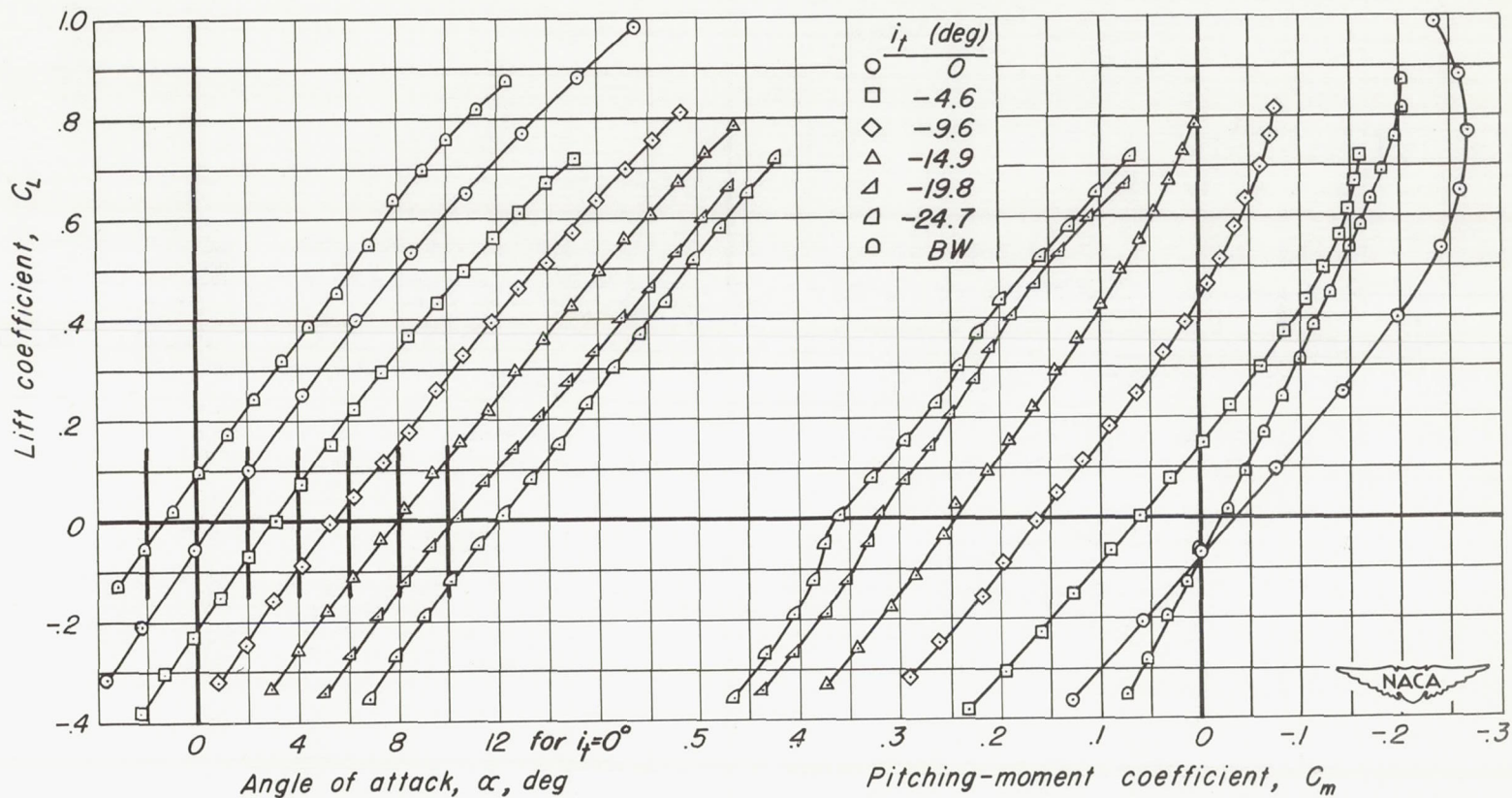
(c) Drag characteristics.

Figure 11. - Continued.



(d) Hinge-moment characteristics .

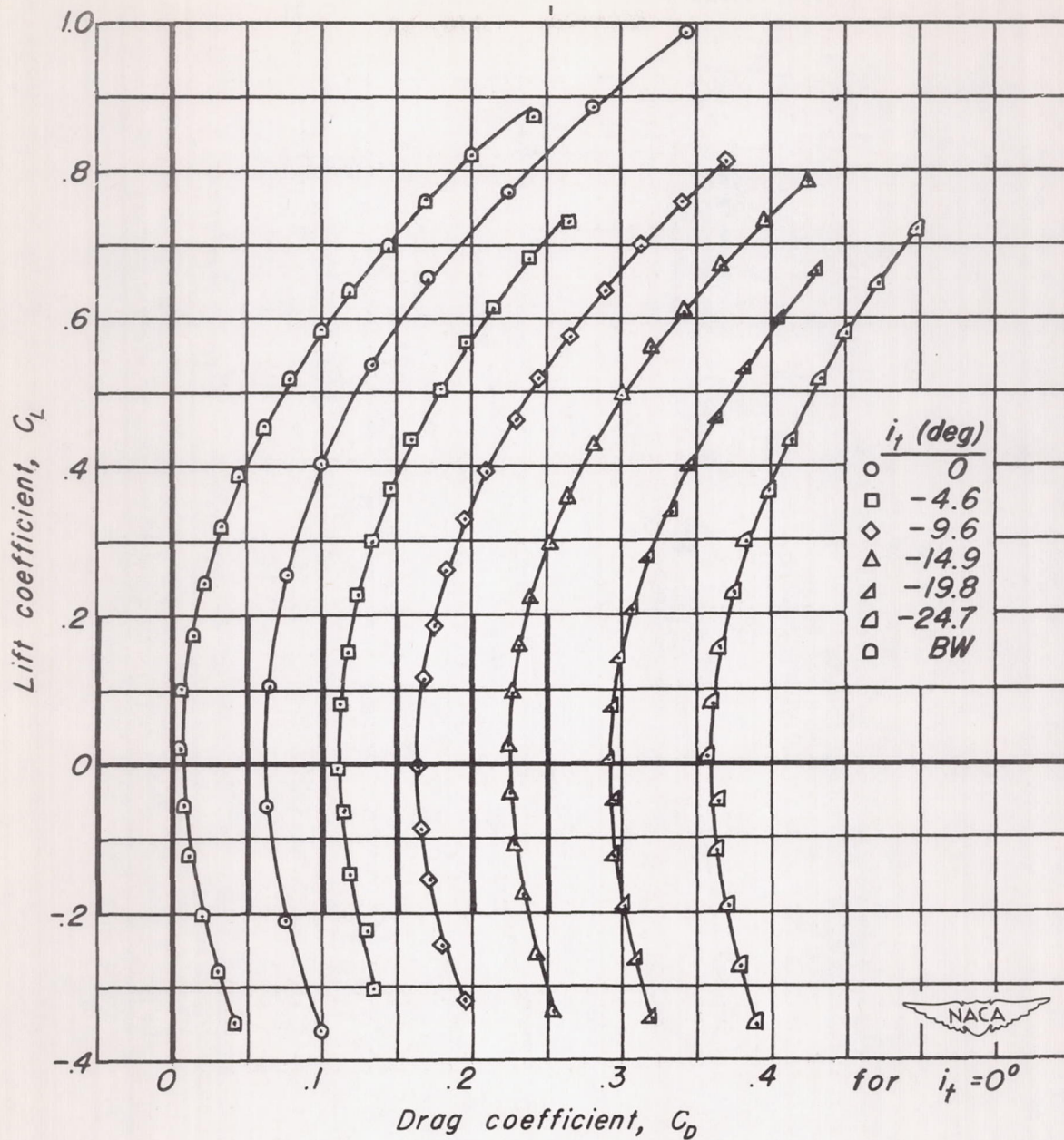
Figure 11.- Concluded.



(a) Lift characteristics.

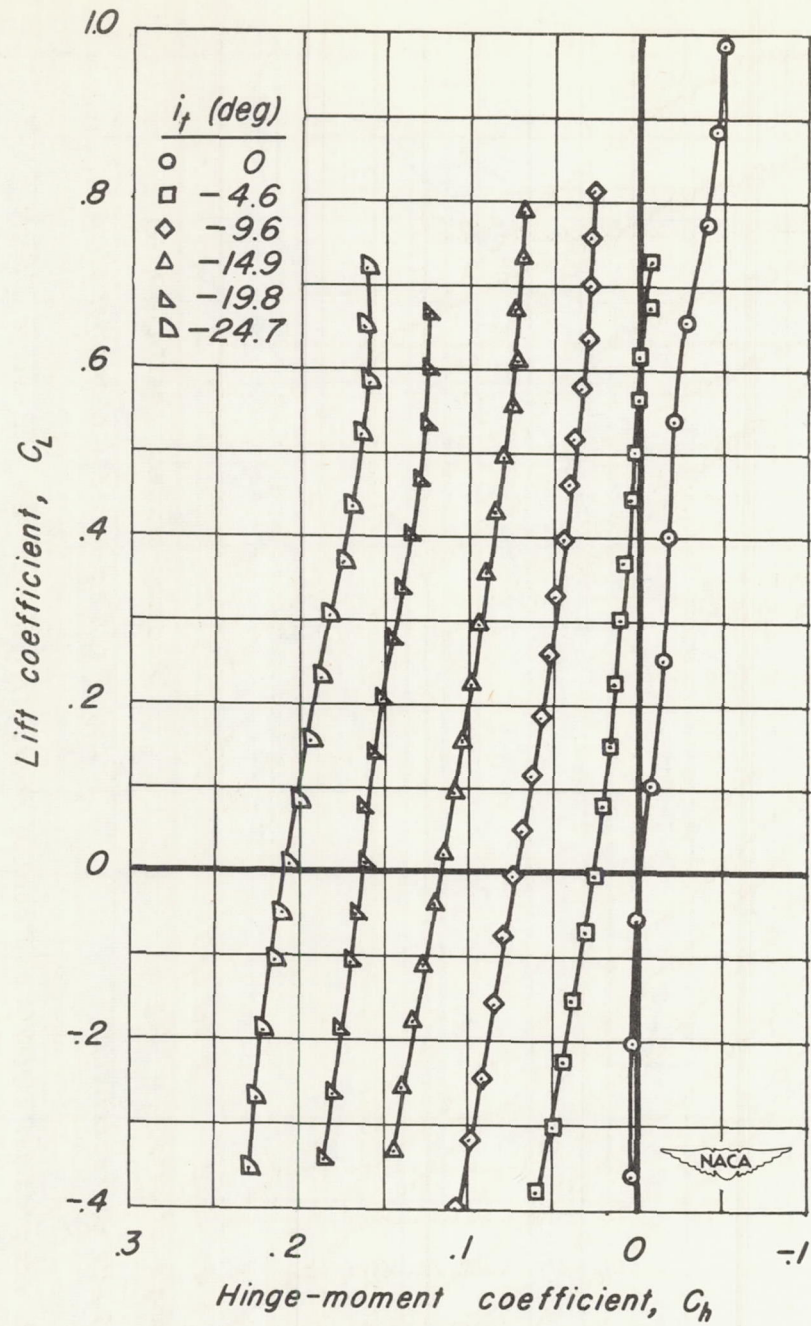
(b) Pitching-moment characteristics.

Figure 12.- Longitudinal stability and control characteristics of the 1/12-scale Douglas X-3 configuration A at a Mach number of 1.50. $R = 2.09 \times 10^6$.



(c) Drag characteristics.

Figure 12.- Continued.



(d) Hinge-moment characteristics

Figure 12.- Concluded.

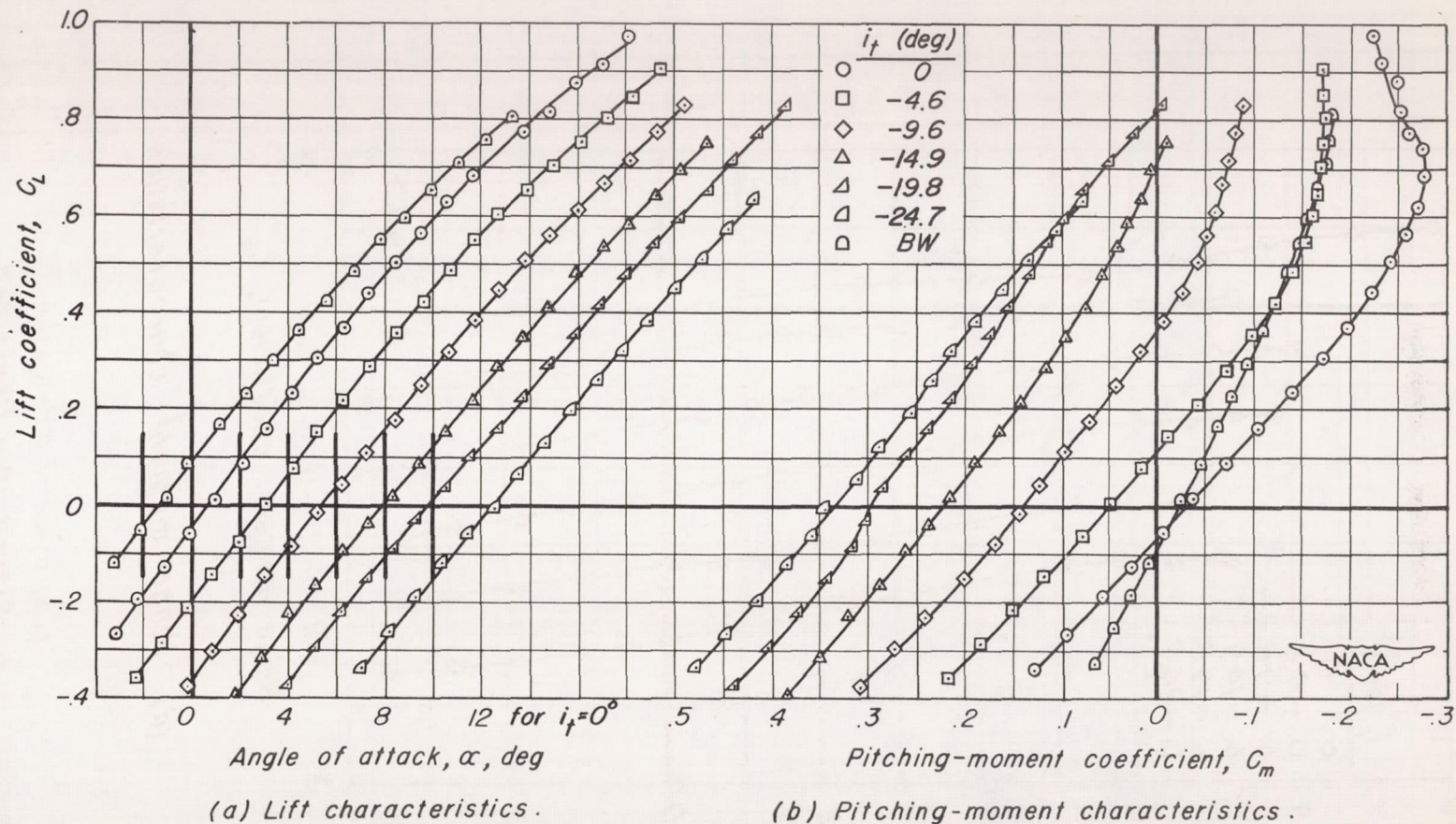
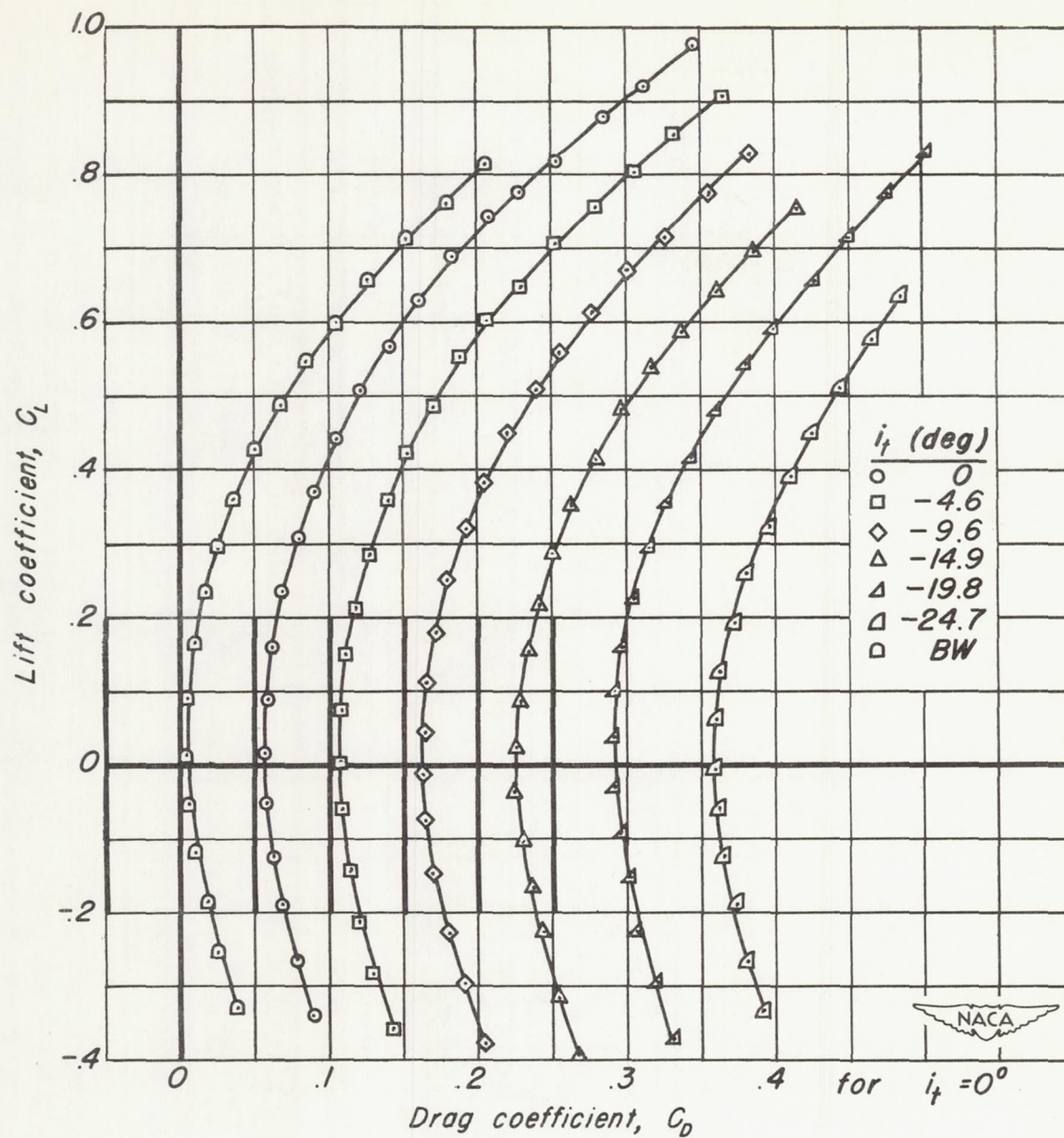
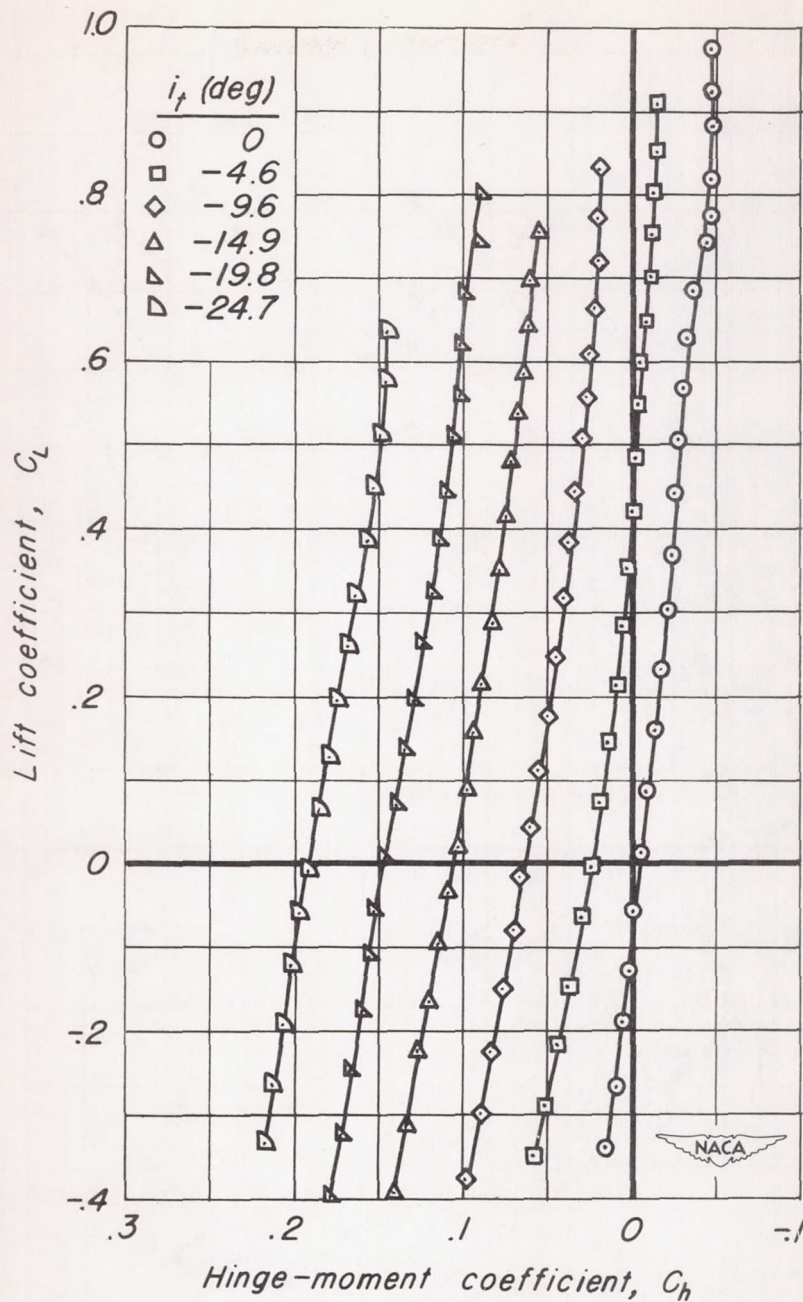


Figure 13.- Longitudinal stability and control characteristics of the 1/12-scale Douglas X-3 configuration A at a Mach number of 1.60. $R=2.09 \times 10^6$.



(c) Drag characteristics.

Figure 13.- Continued.



(d) Hinge-moment characteristics.

Figure 13.- Concluded.

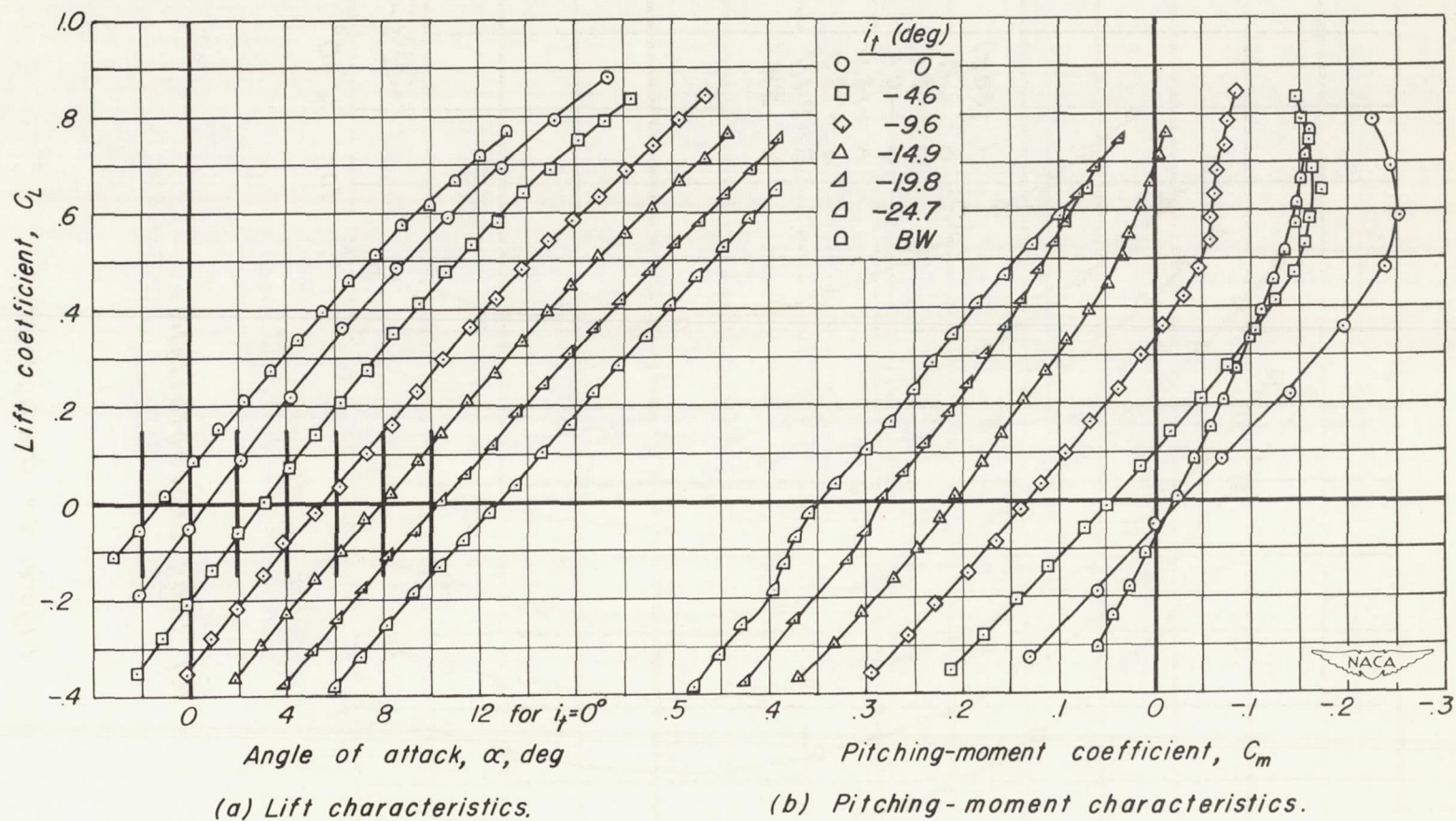
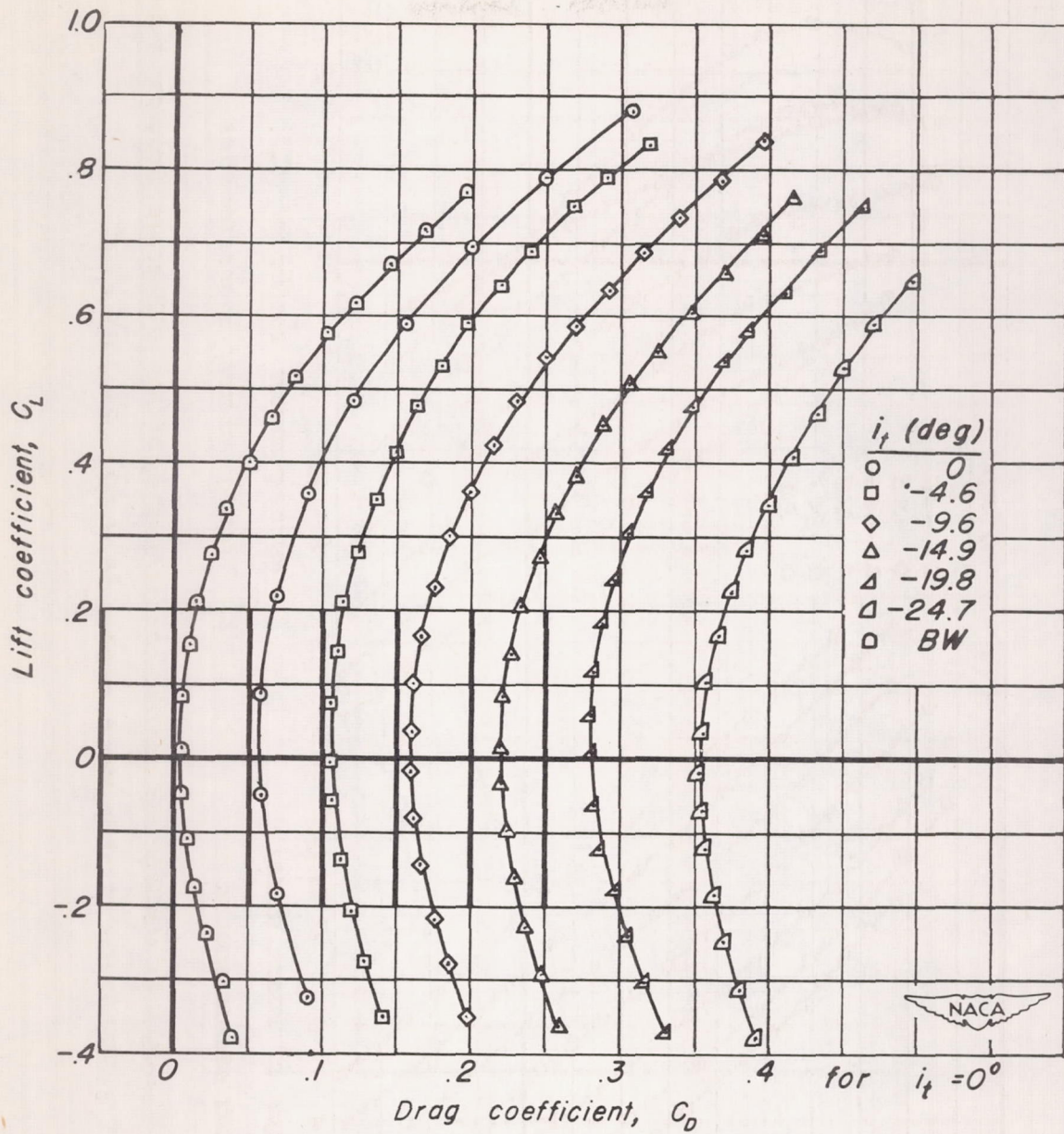
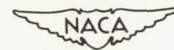
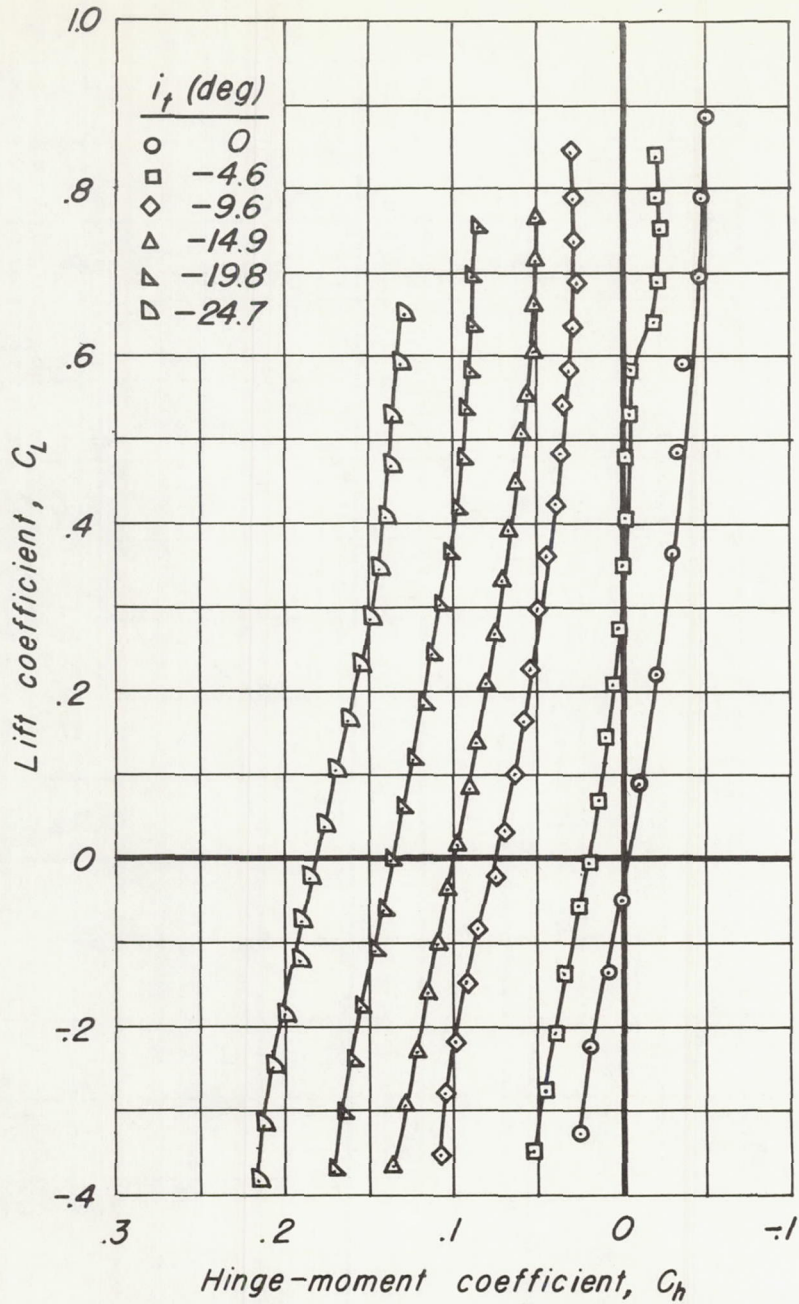


Figure 14.- Longitudinal stability and control characteristics of the 1/12-scale Douglas X-3 configuration A at a Mach number of 1.70. $R = 2.09 \times 10^6$.



(c) Drag characteristics.

Figure 14.- Continued.



(d) Hinge-moment characteristics.

Figure 14. - Concluded.

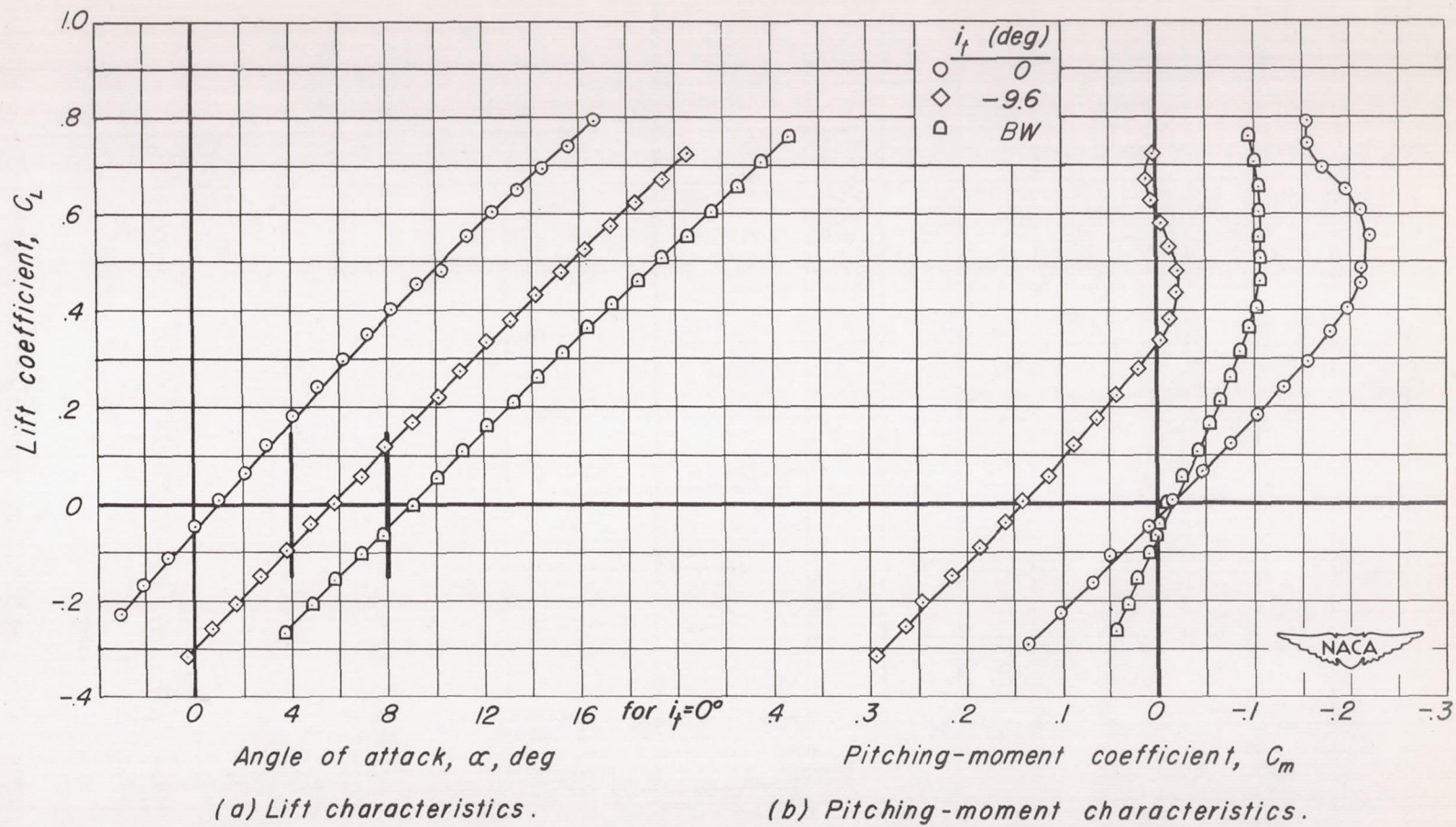
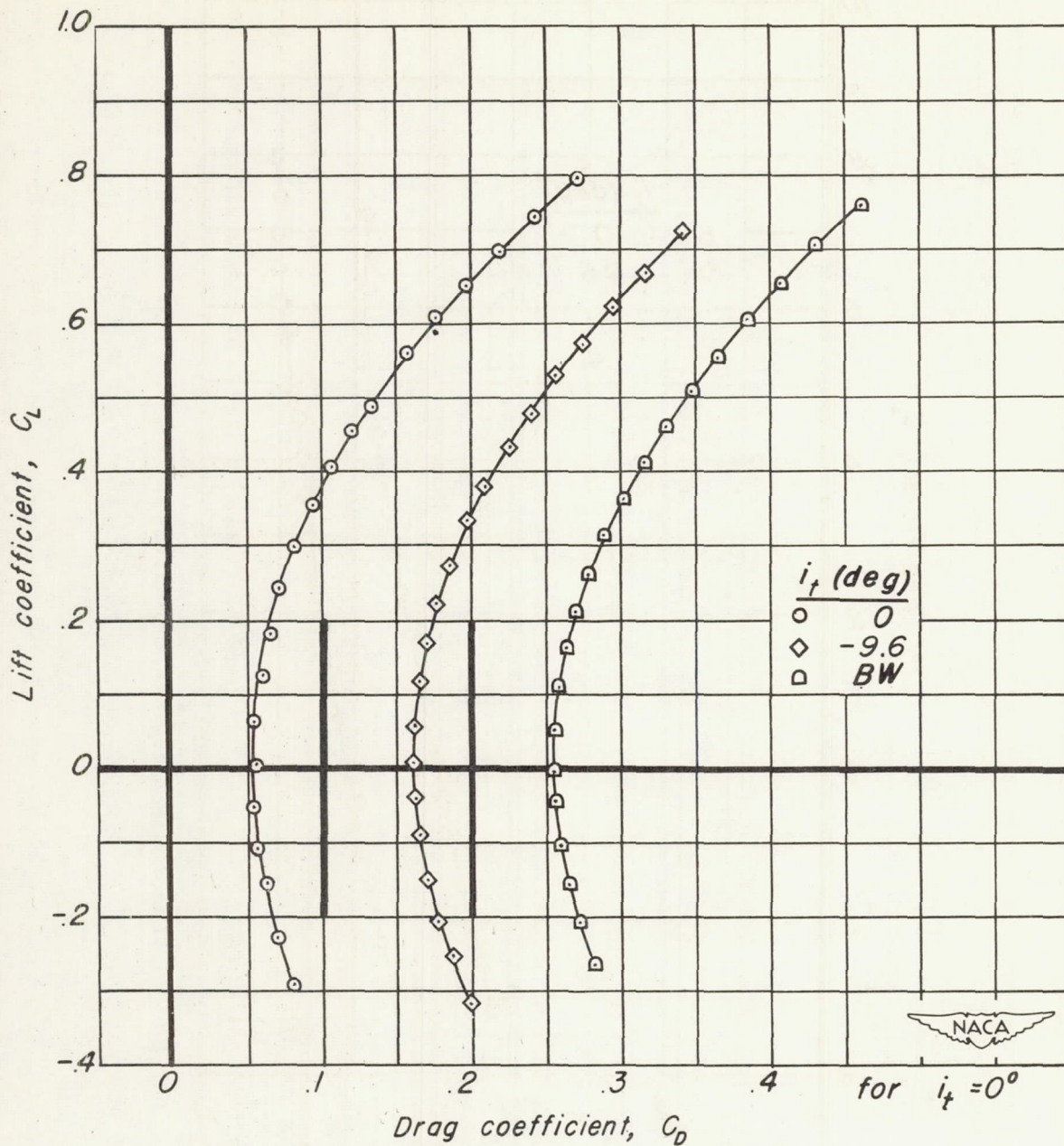
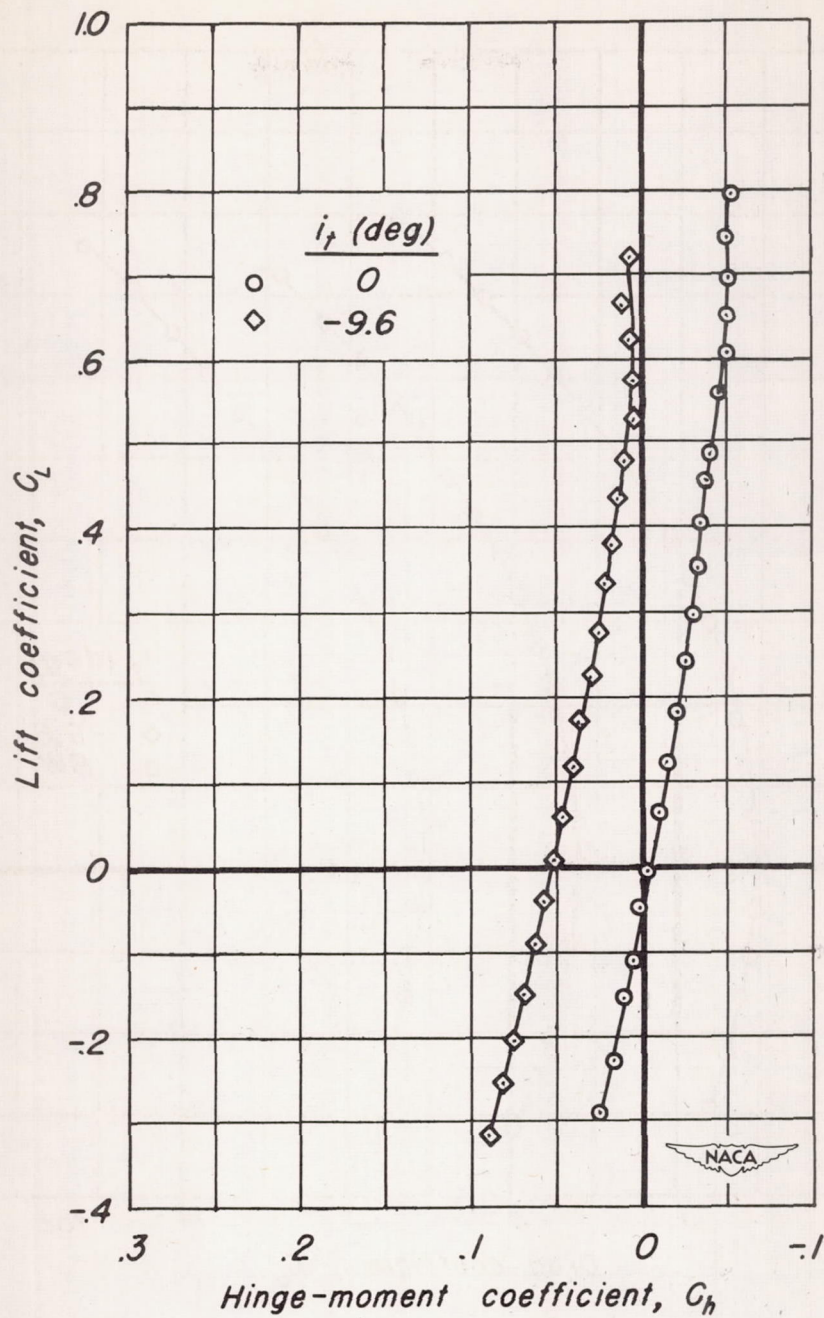


Figure 15. - Longitudinal stability and control characteristics of the 1/12-scale Douglas X-3 configuration A at a Mach number of 1.91. $R = 0.98 \times 10^6$.



(c) Drag characteristics.

Figure 15.- Continued.



(d) Hinge-moment characteristics.

Figure 15.- Concluded.

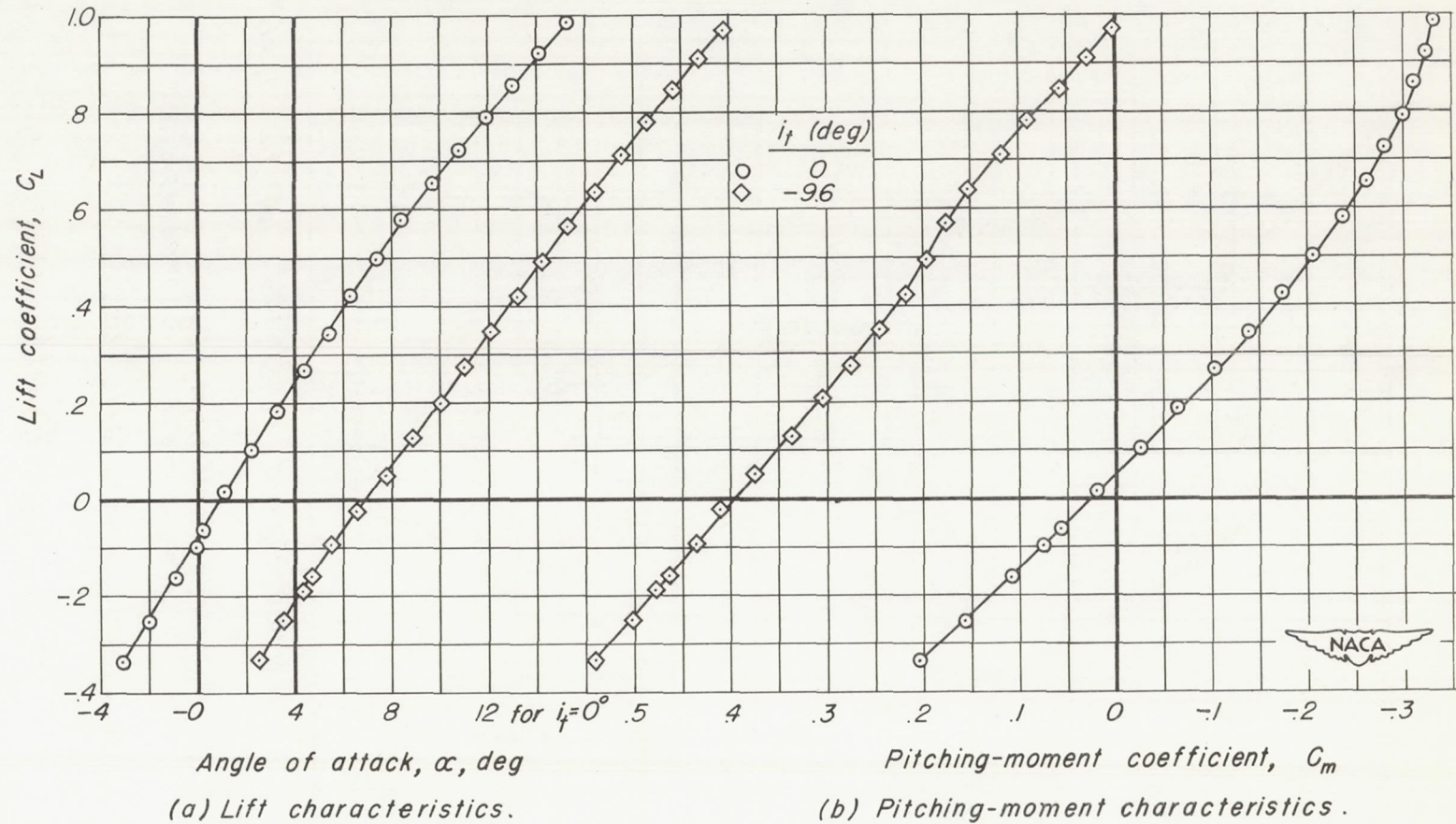
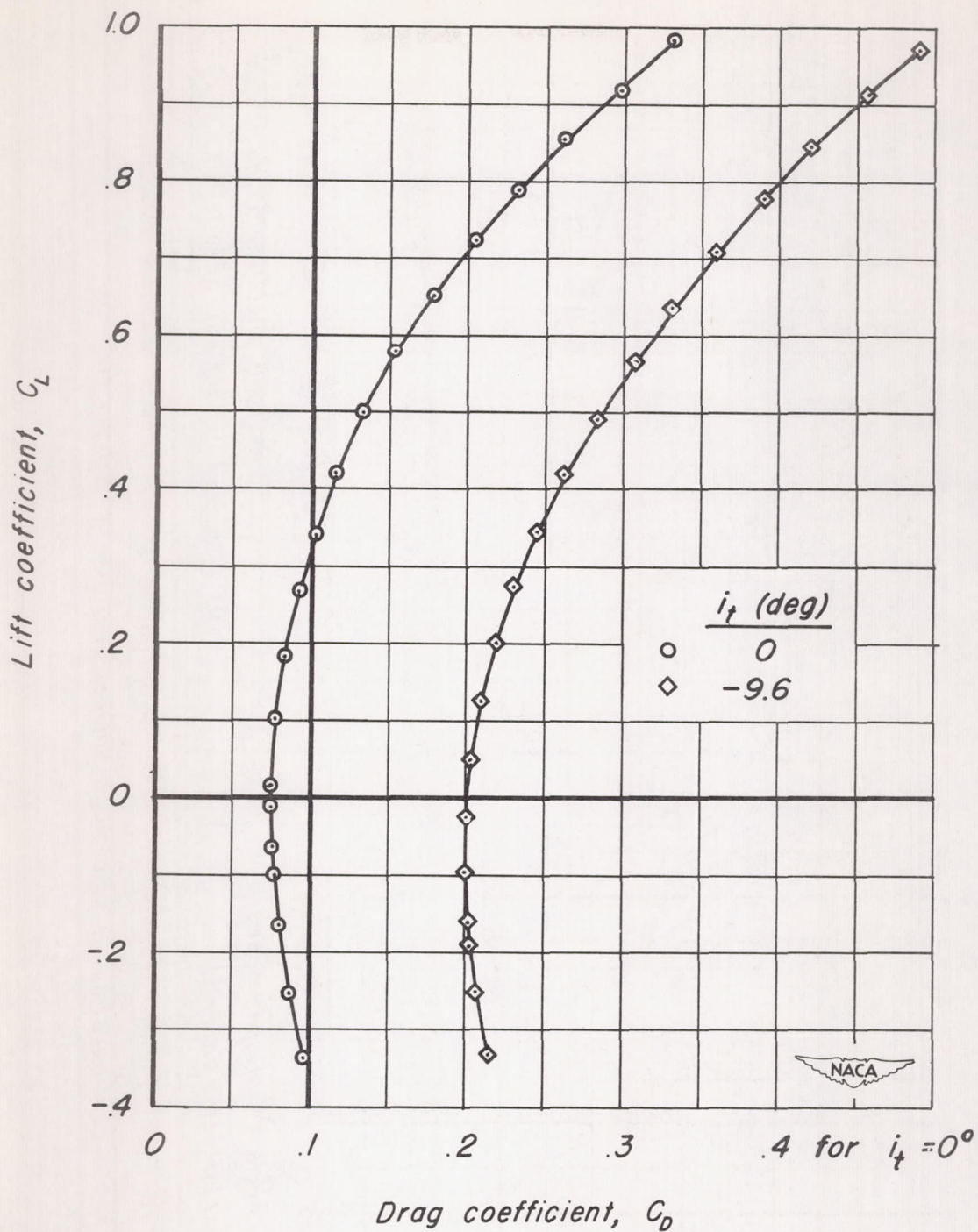
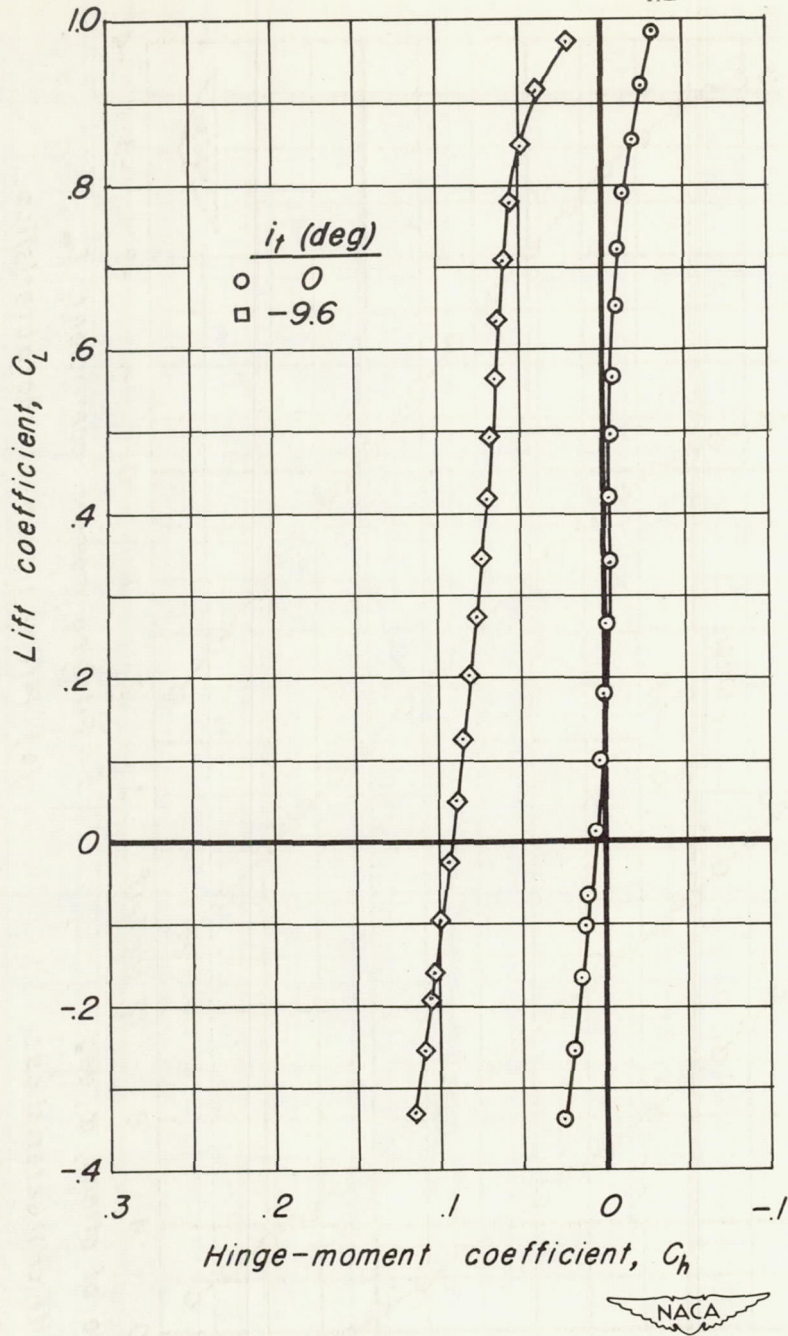


Figure 16.- Longitudinal stability and control characteristics of the 1/12-scale Douglas X-3 configuration B at a Mach number of 1.30. $R = 2.09 \times 10^6$.



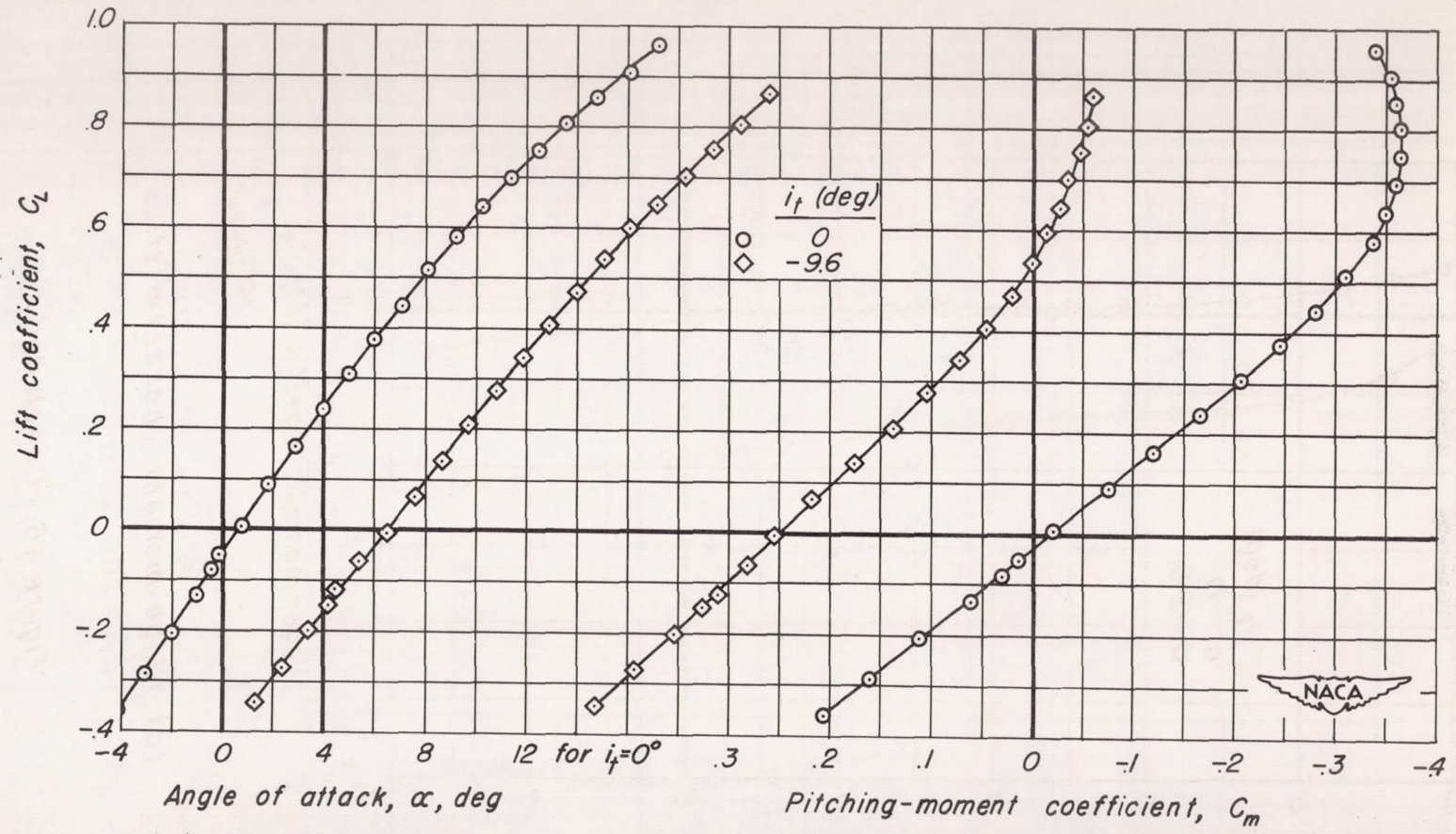
(c) Drag characteristics.

Figure 16.- Continued.

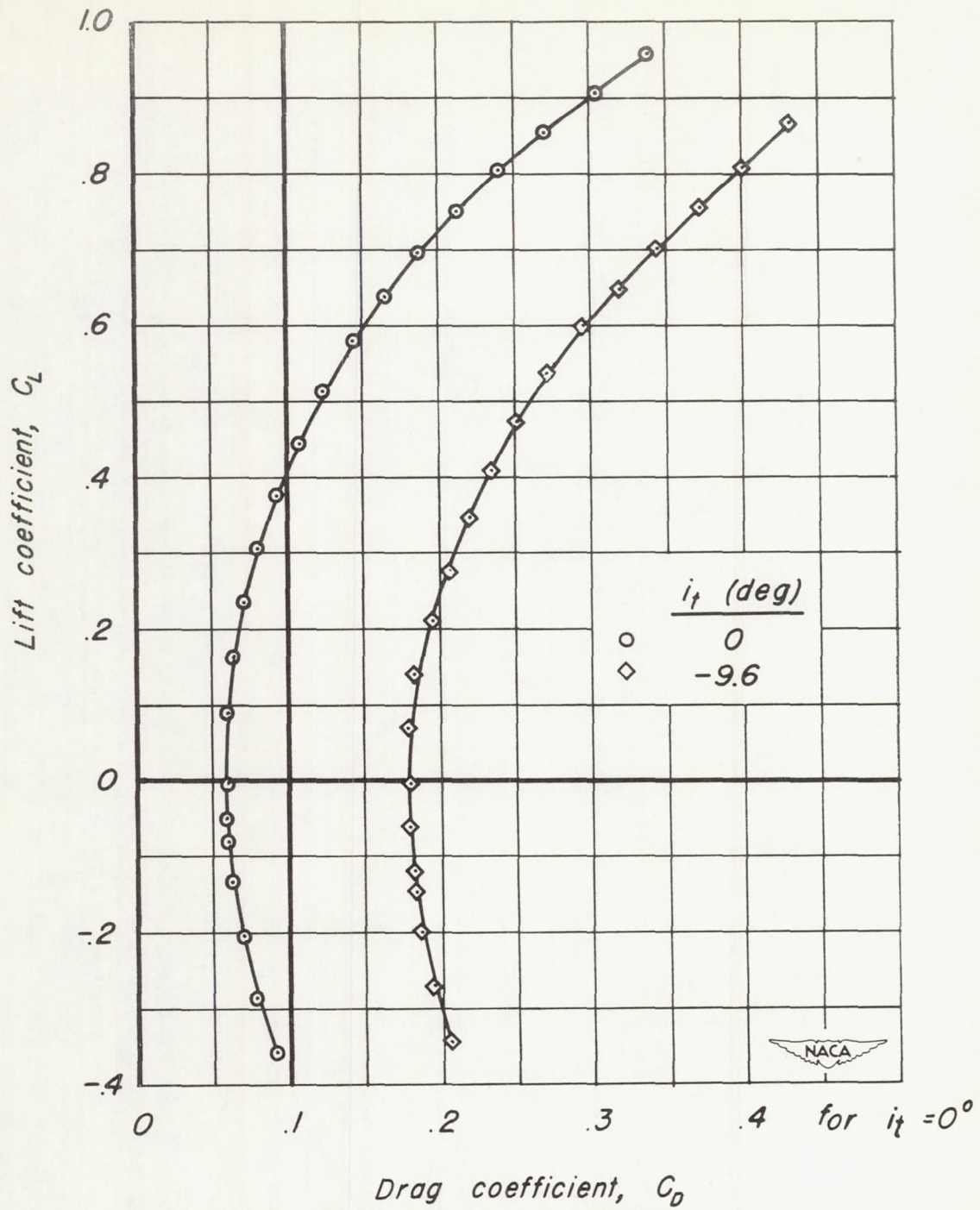


(d) Hinge-moment characteristics.

Figure 16.- Concluded.

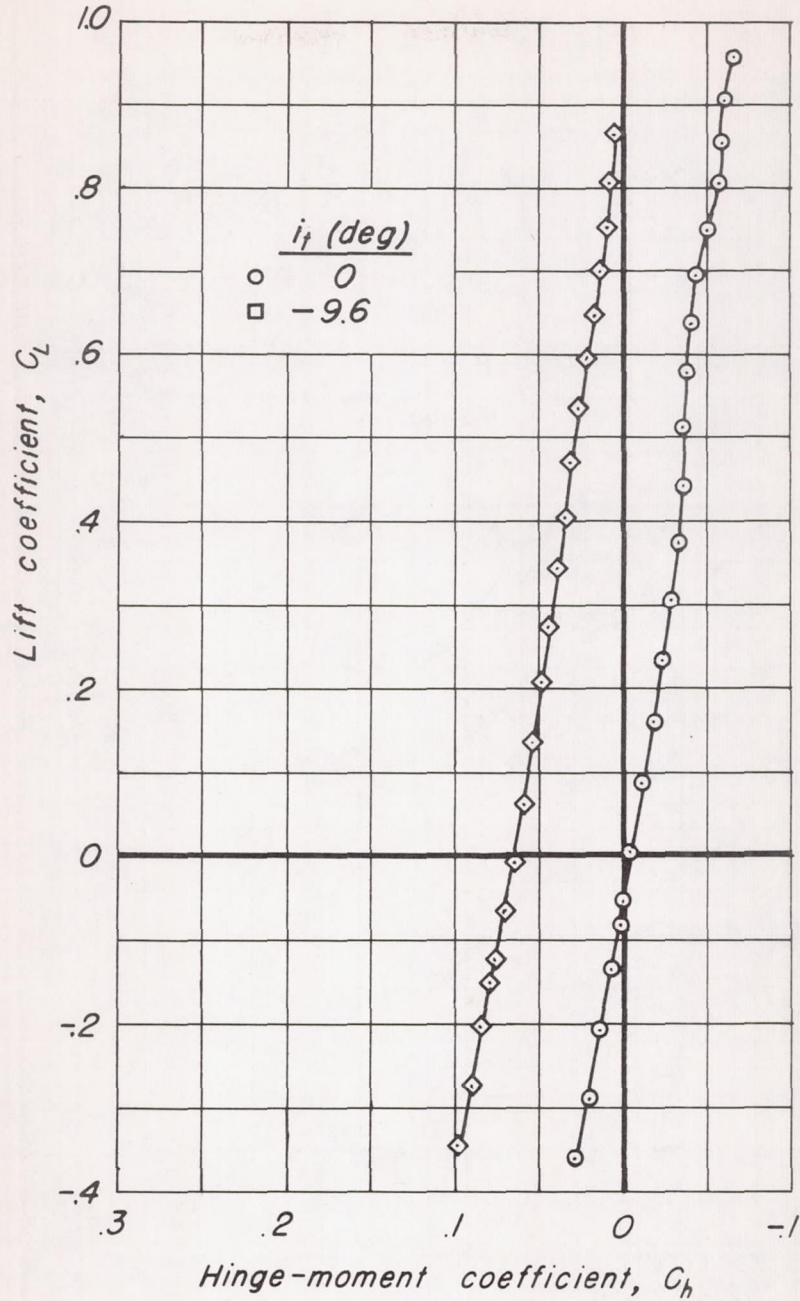


(a) Lift characteristics. (b) Pitching-moment characteristics.
 Figure 17.- Longitudinal stability and control characteristics of the 1/12-scale Douglas X-3 configuration B at a Mach number of 1.60. $R = 2.09 \times 10^6$.



(c) Drag characteristics.

Figure 17.- Continued.



(d) Hinge-moment characteristics.

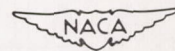


Figure 17.- Concluded

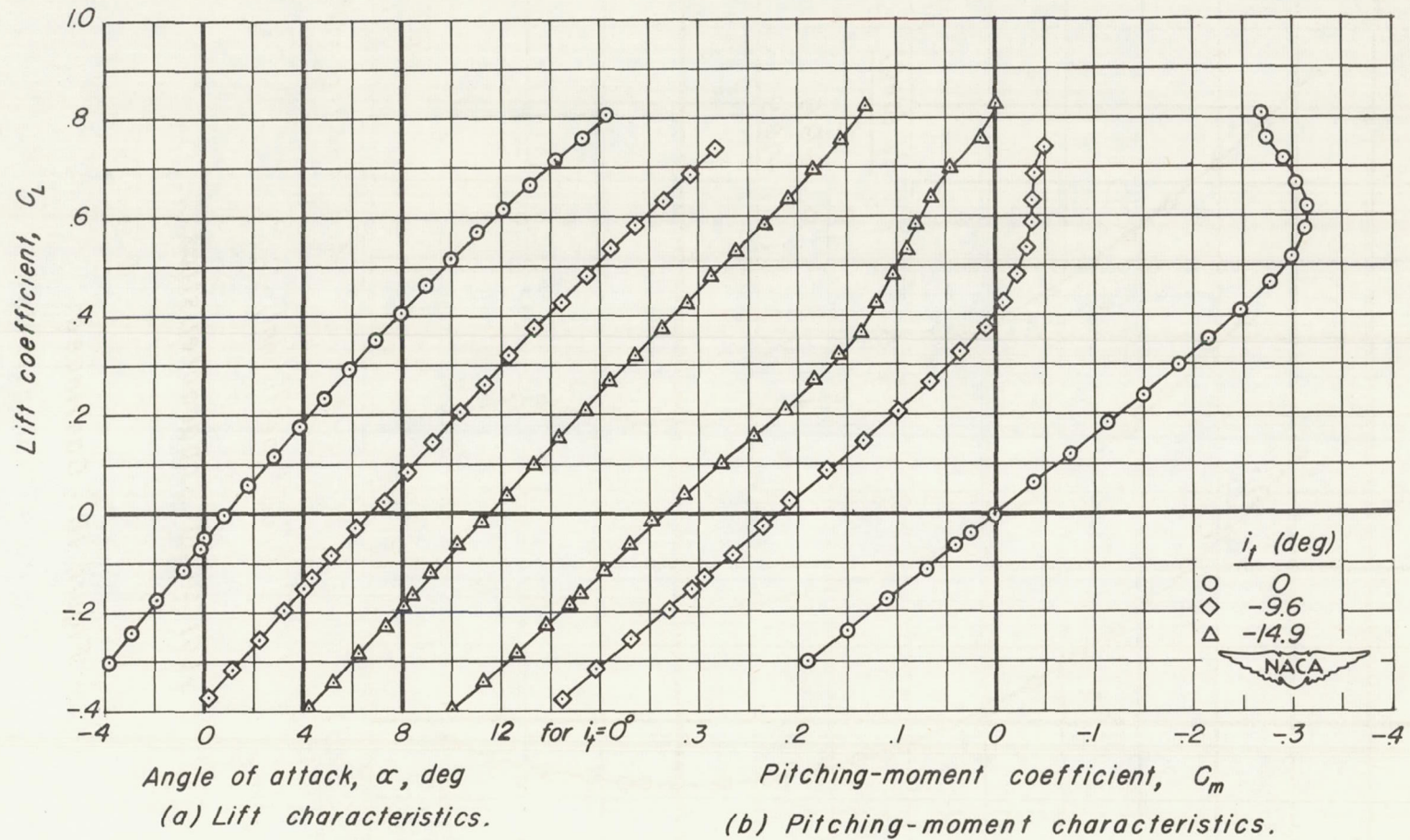
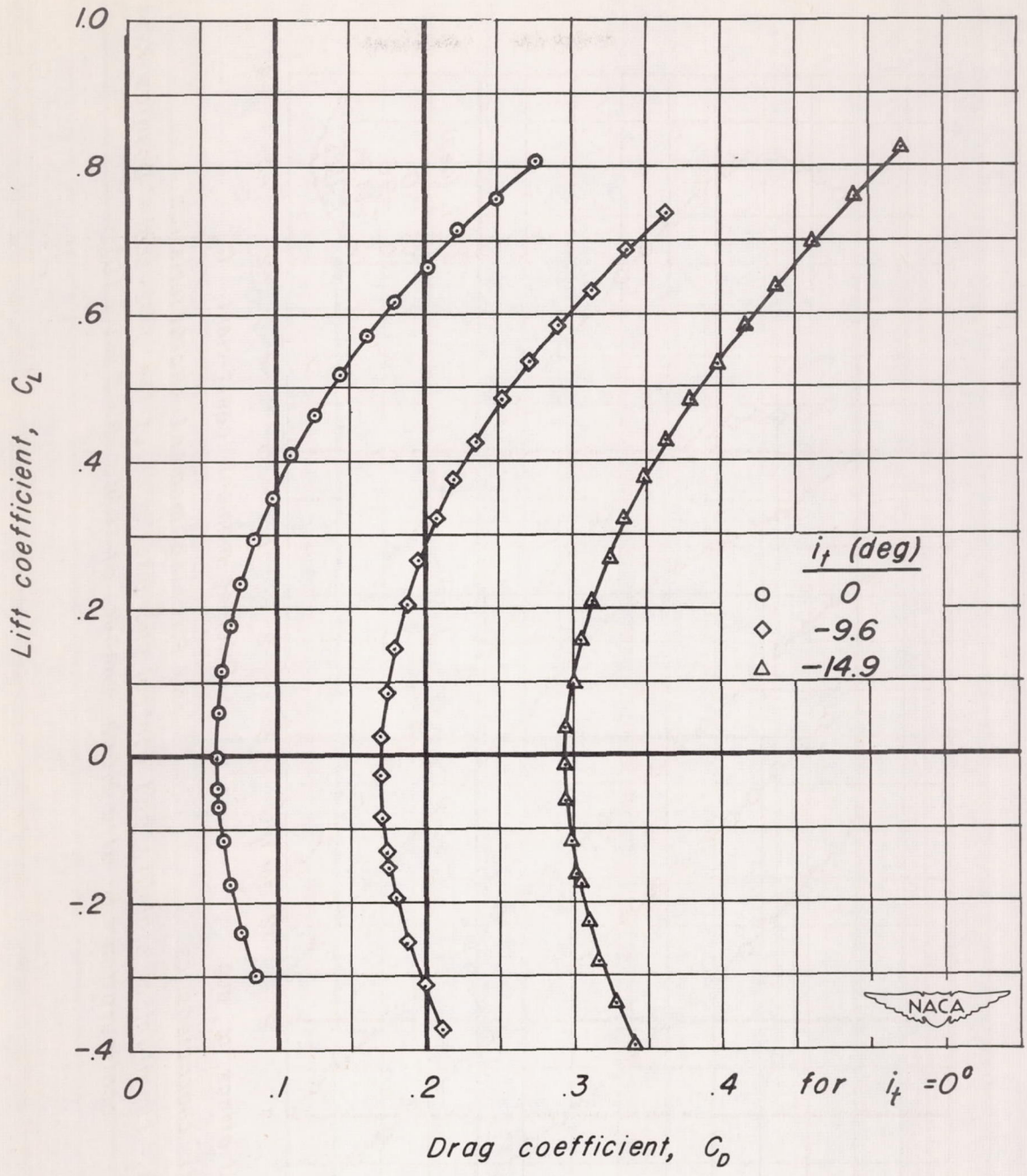
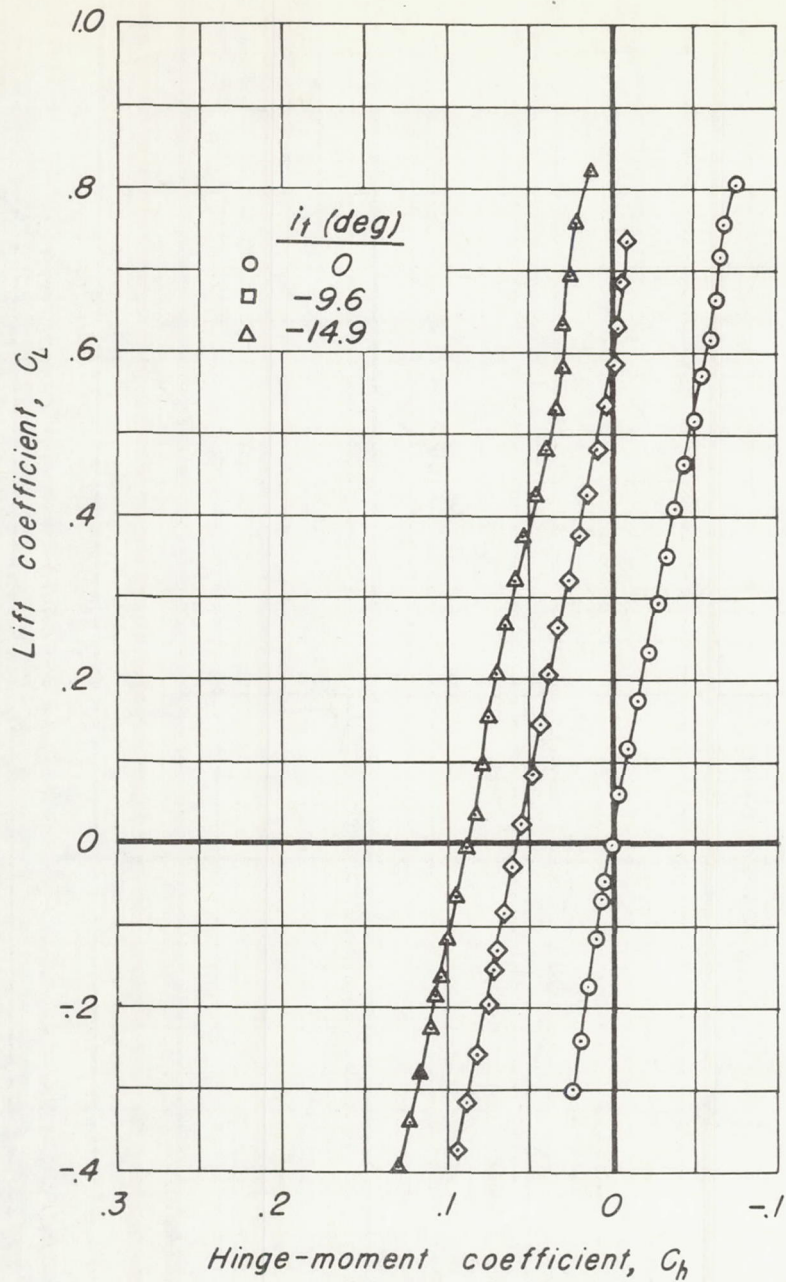


Figure 18.- Longitudinal stability and control characteristics of the 1/12-scale Douglas X-3 configuration B at a Mach number of 1.91. $R = 0.98 \times 10^6$.



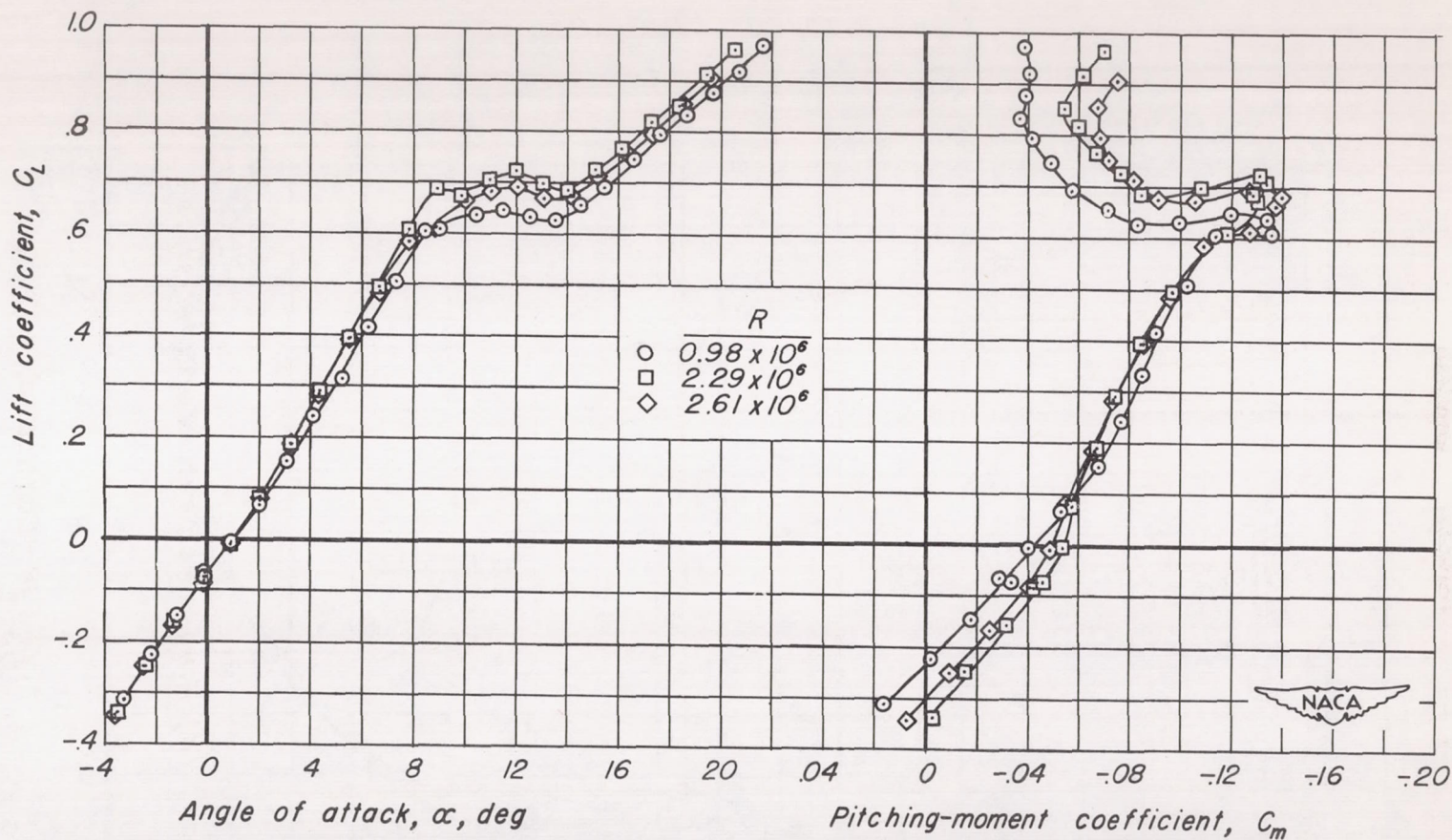
(c) Drag characteristics.

Figure 18.- Continued.

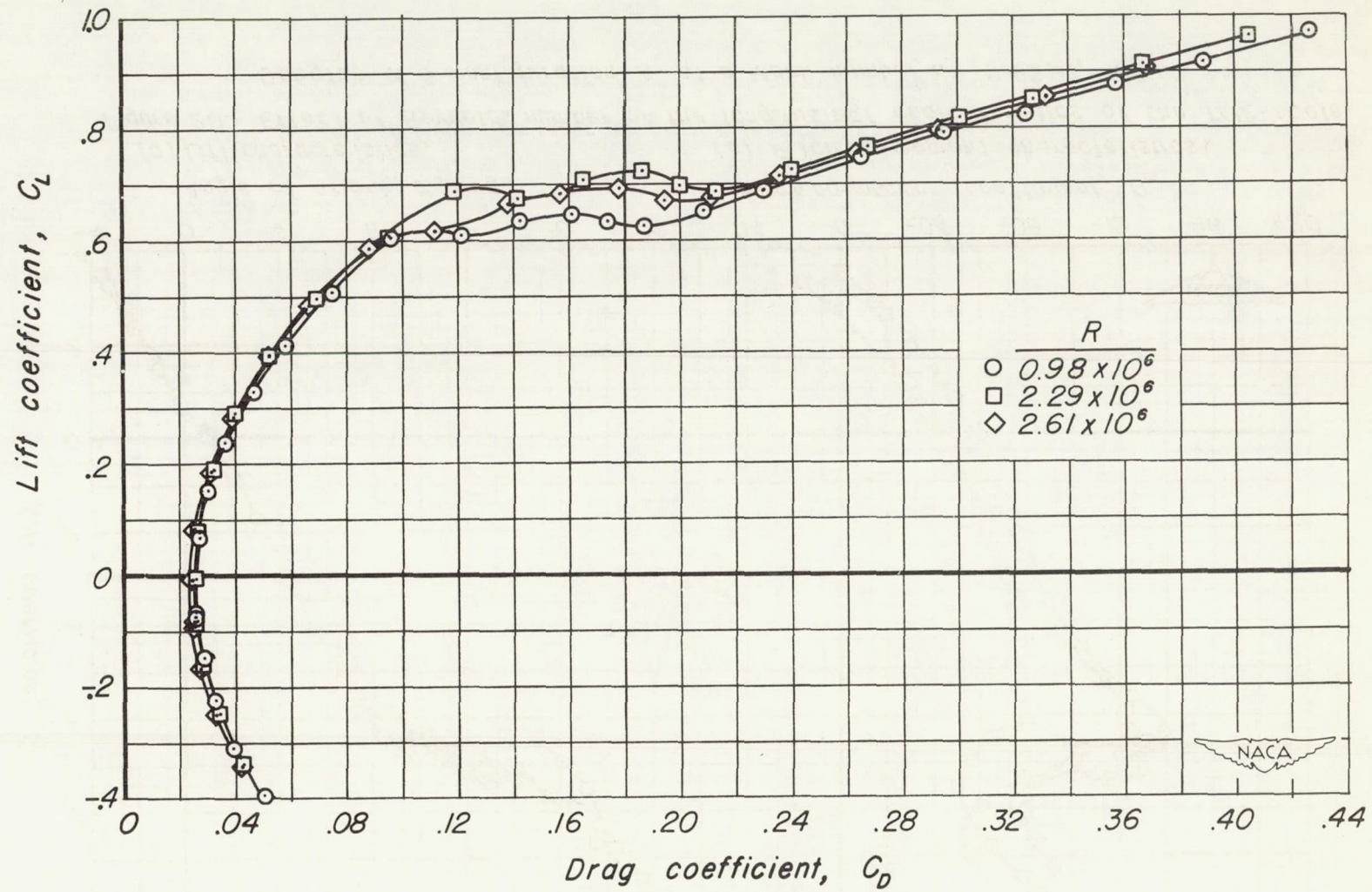


(d) Hinge-moment characteristics.

Figure 18.-Concluded.

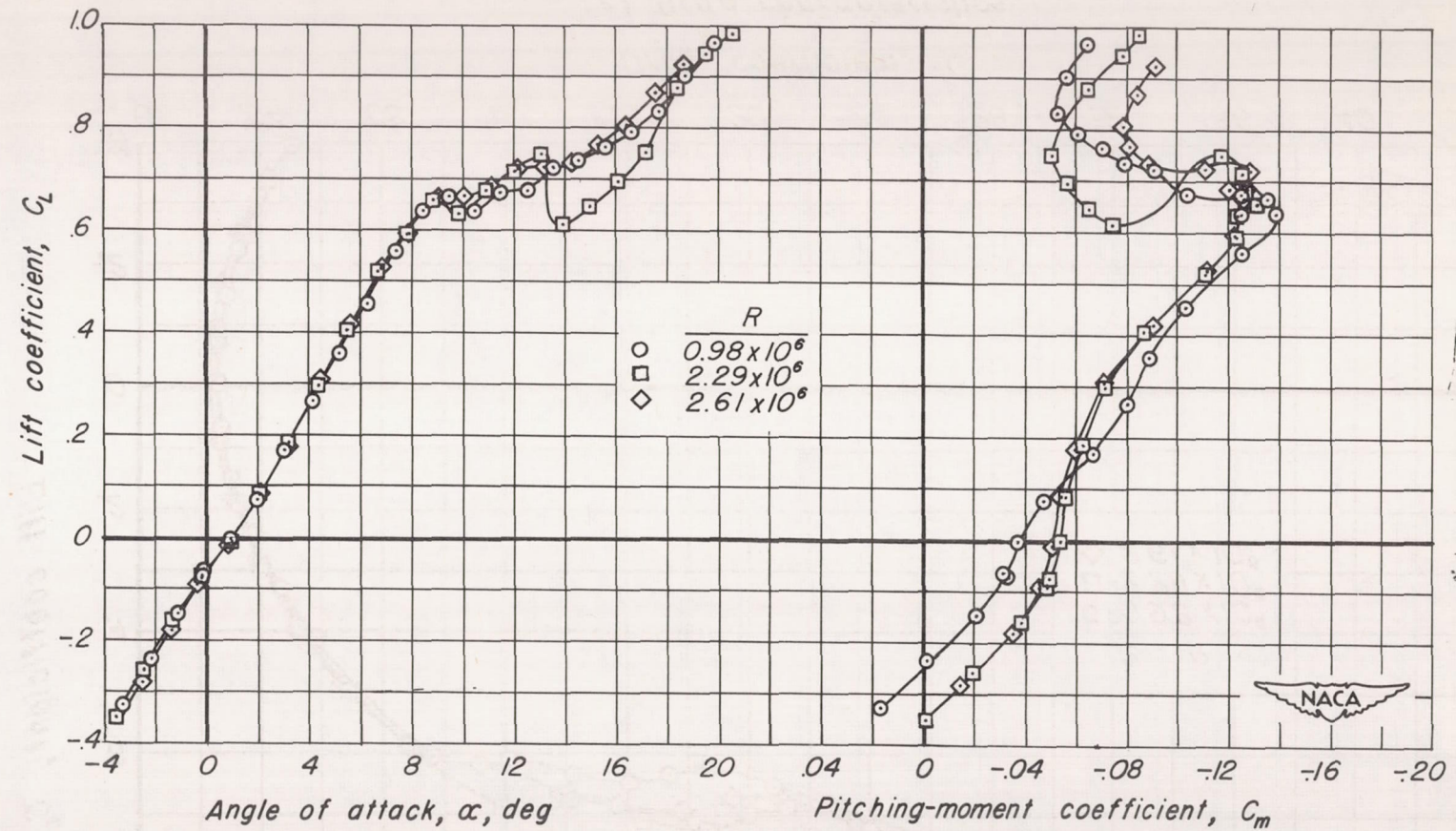


(a) Lift characteristics. (b) Pitching-moment characteristics.
 Figure 19.- Effect of Reynolds number on the longitudinal characteristics of the 1/12-scale Douglas X-3 configuration A at a Mach number of 0.80. $i_t = 0^\circ$.

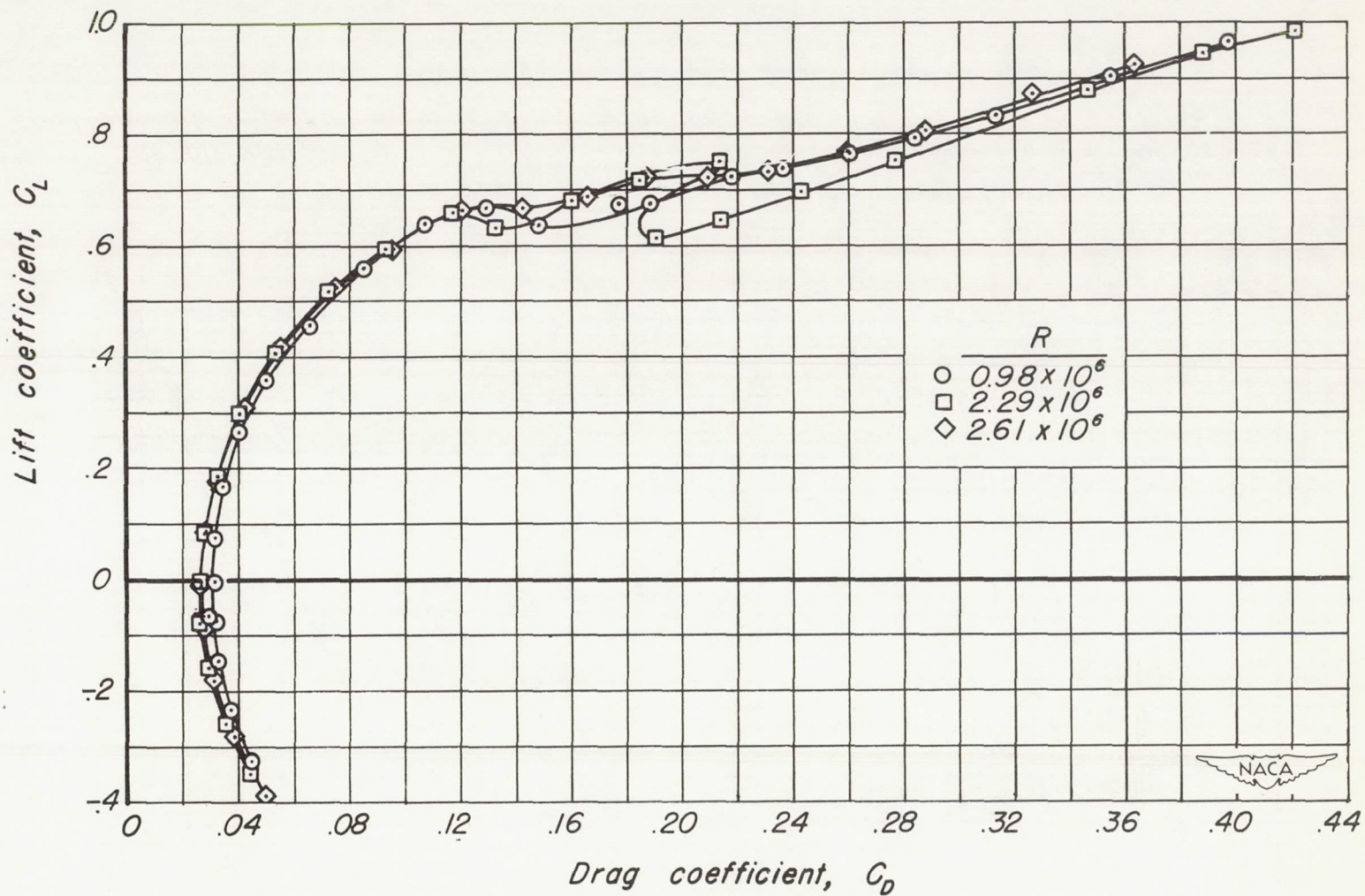


(c) Drag characteristics.

Figure 19. - Concluded.

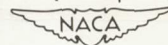


(a) Lift characteristics. (b) Pitching-moment characteristics.
 Figure 20.- Effect of Reynolds number on the longitudinal characteristics of the 1/12-scale Douglas X-3 configuration A at a Mach number of 0.85. $i_i = 0^\circ$.



(c) Drag characteristics.

Figure 20.- Concluded.



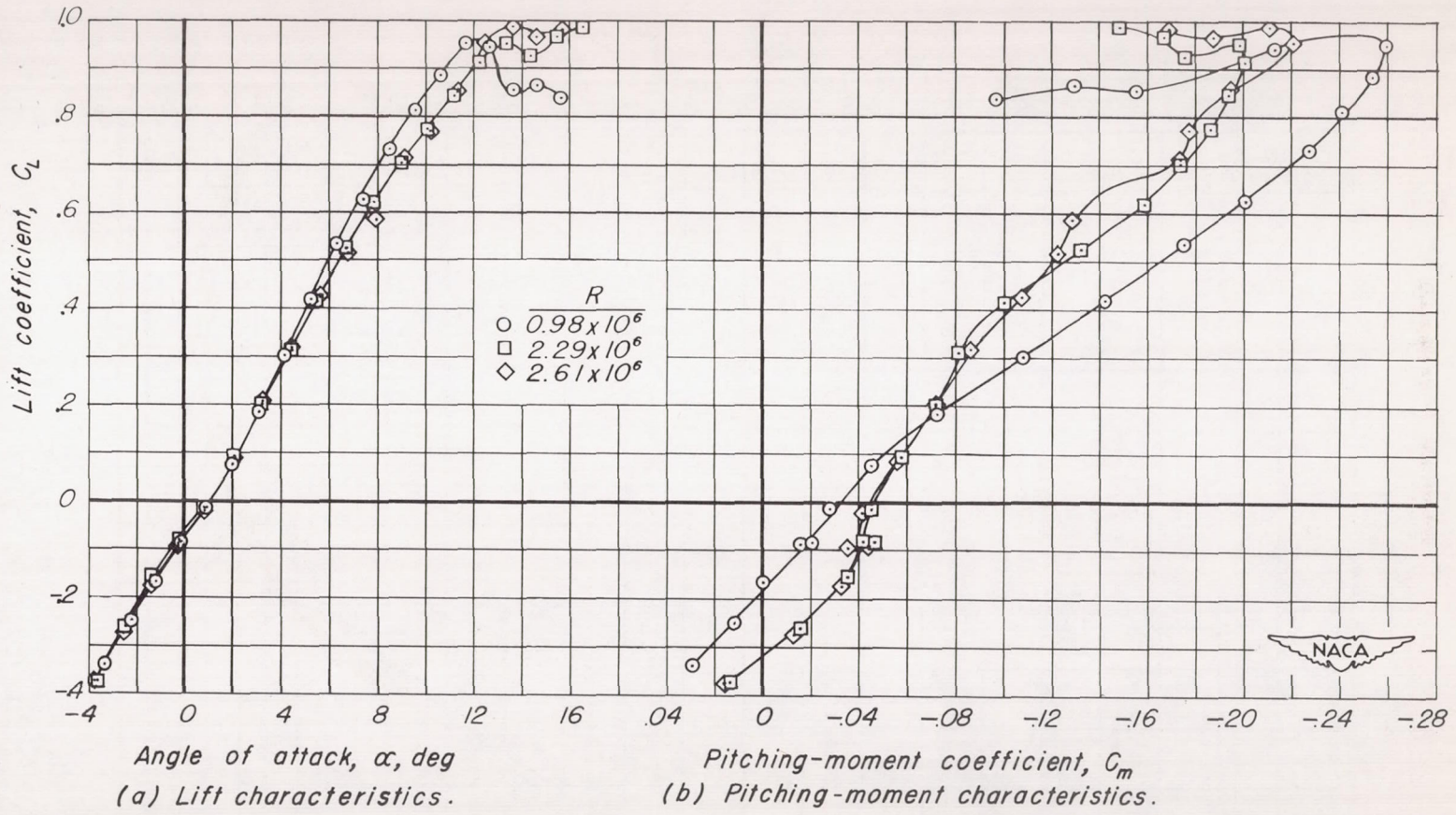
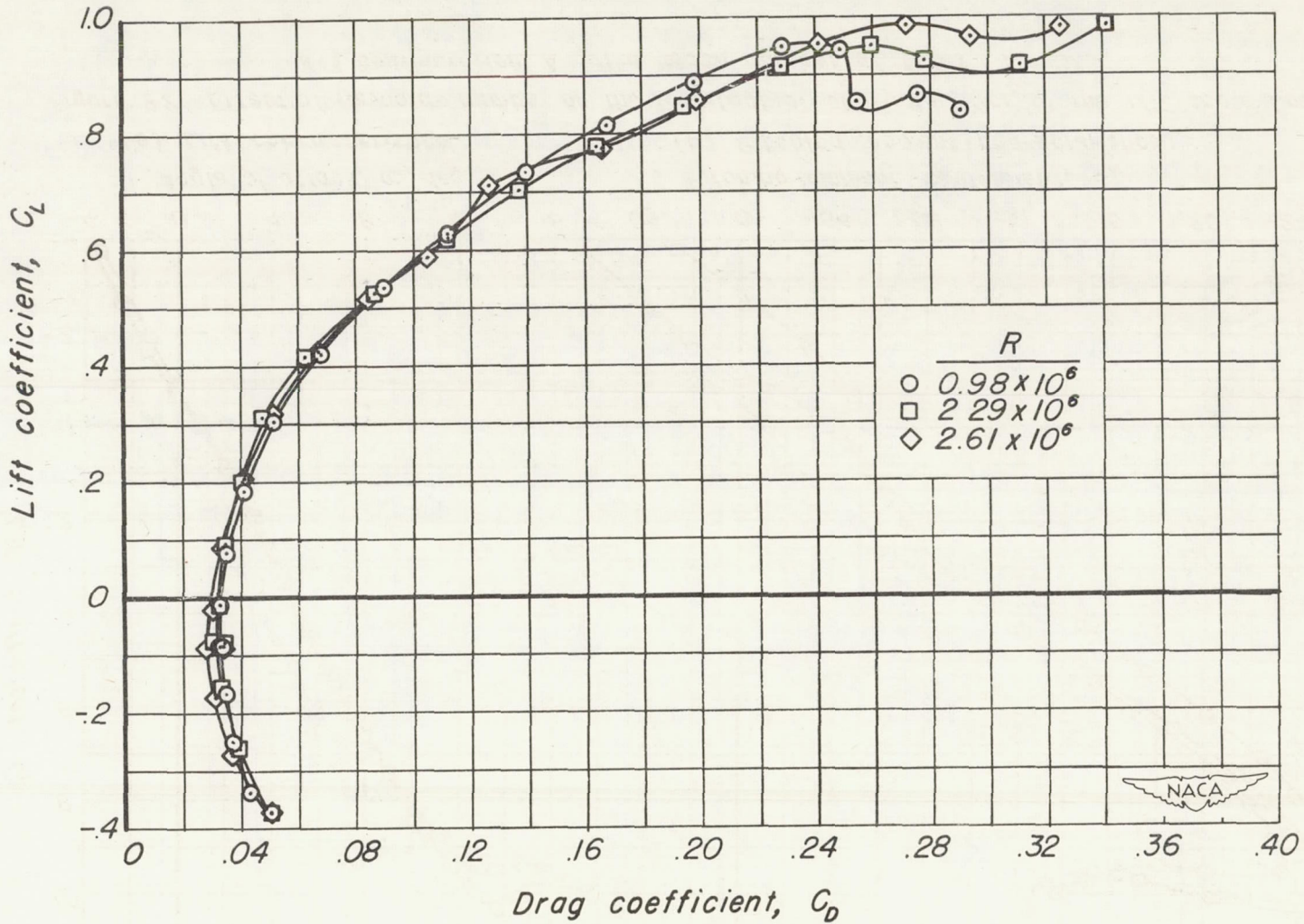


Figure 21.- Effect of Reynolds number on the longitudinal characteristics of the 1/12-scale Douglas X-3 configuration A at a Mach number of 0.90. $i_1 = 0^\circ$.



(c) Drag characteristics.

Figure 21.- Concluded.

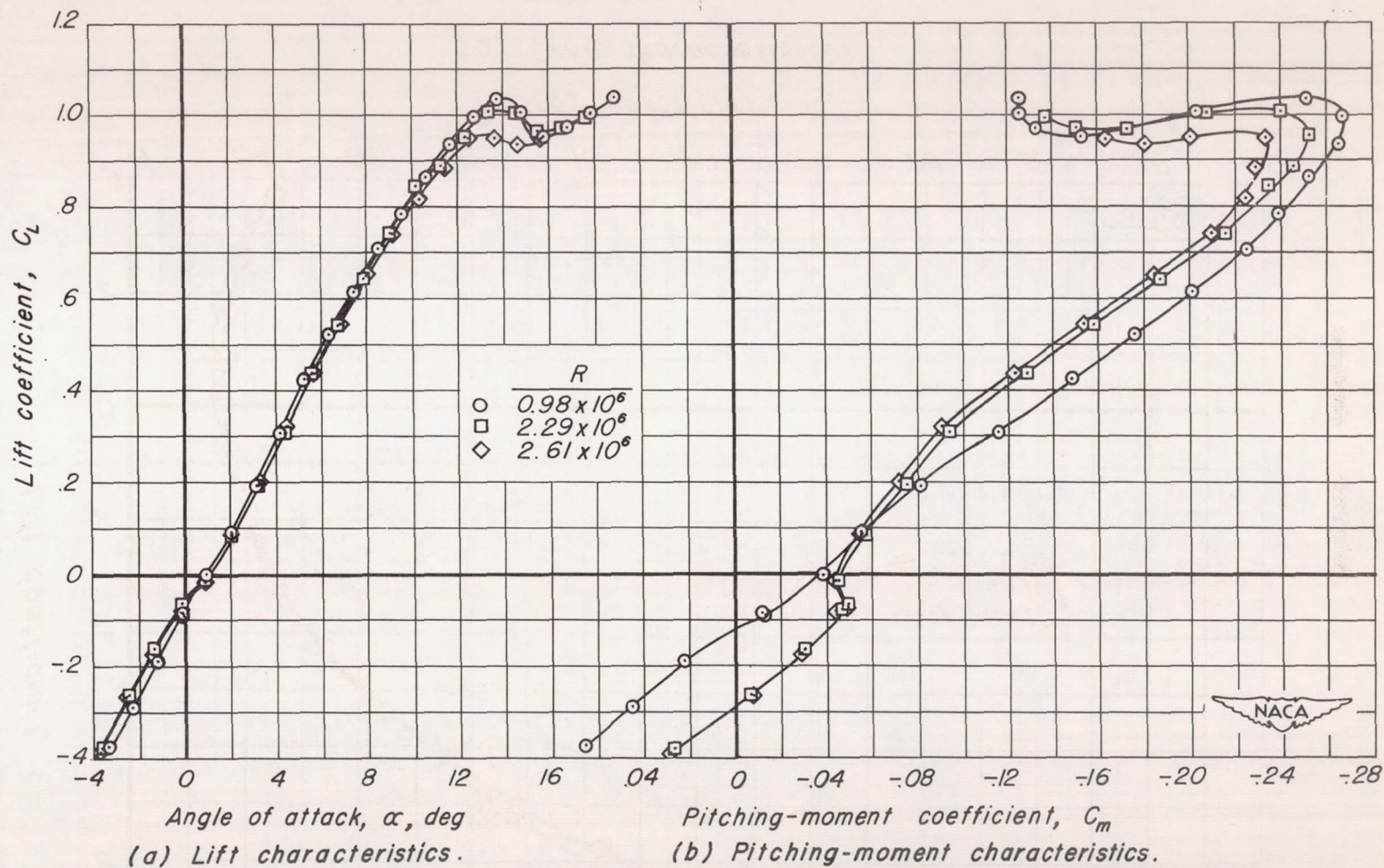
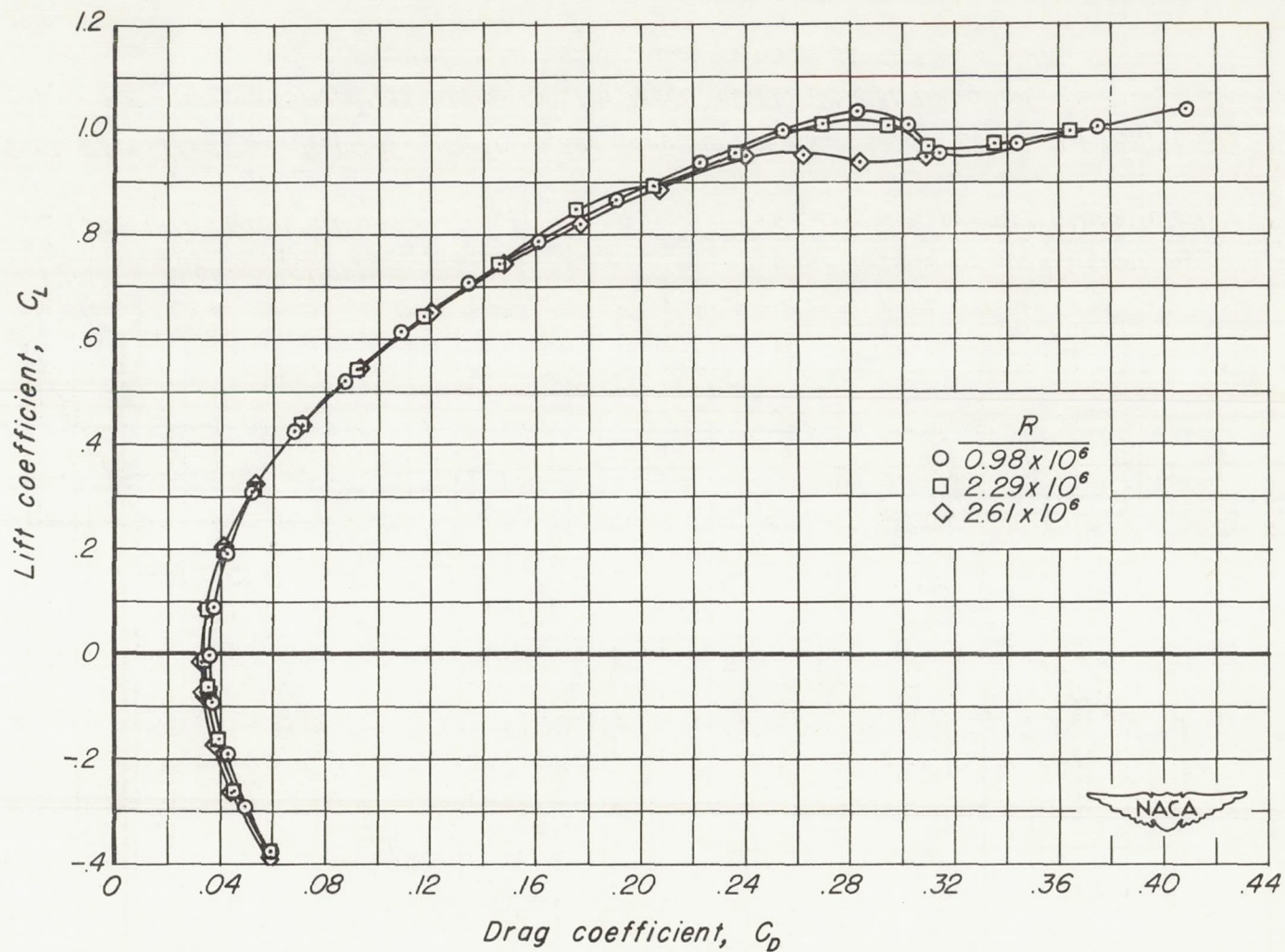
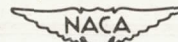


Figure 22.- Effect of Reynolds number on the longitudinal characteristics of the 1/12-scale Douglas X-3 configuration A at a Mach number of 0.93. $i_1 = 0^\circ$.



Drag coefficient, C_D
 (c) Drag characteristics.

Figure 22.- Concluded.



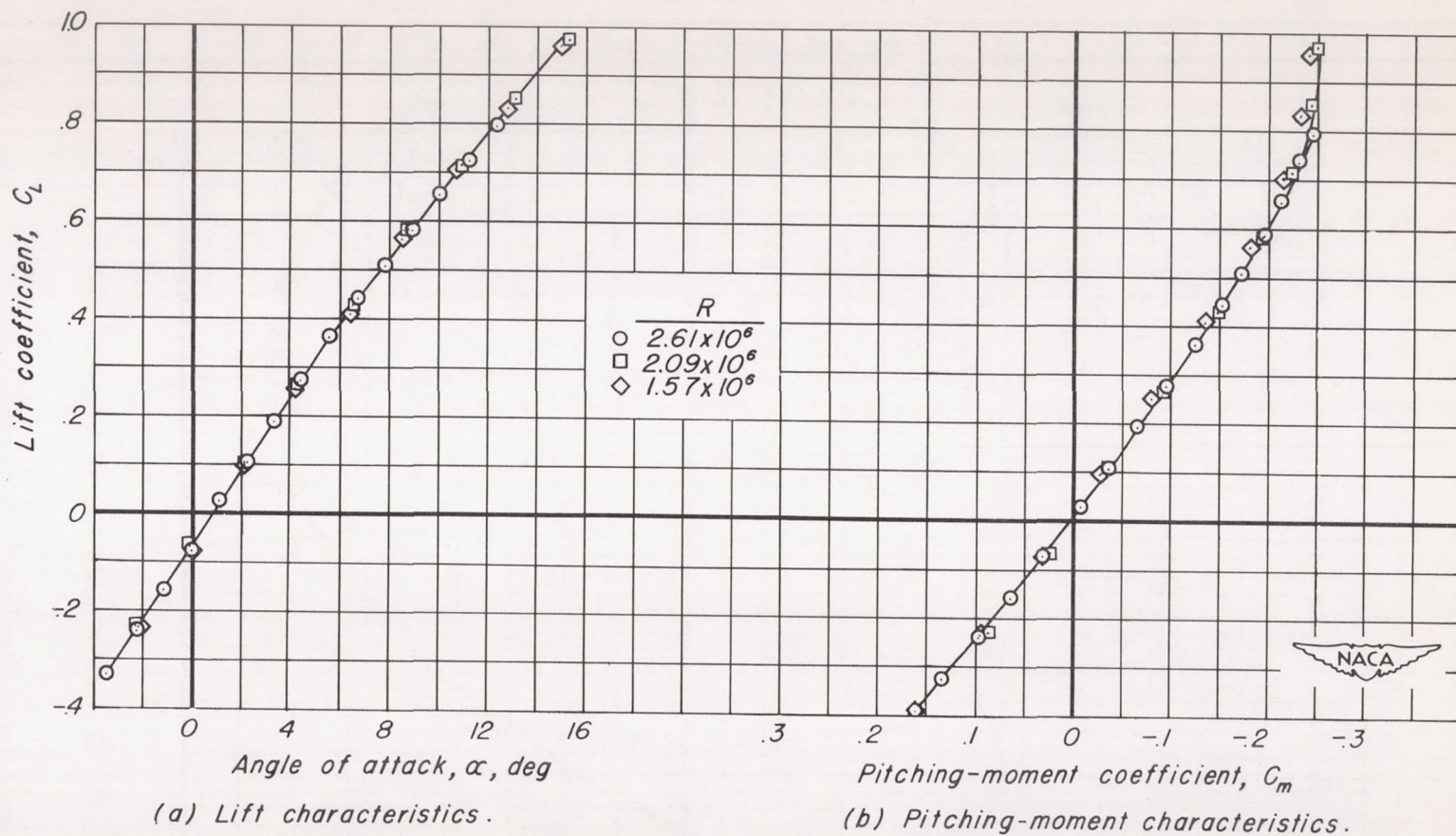
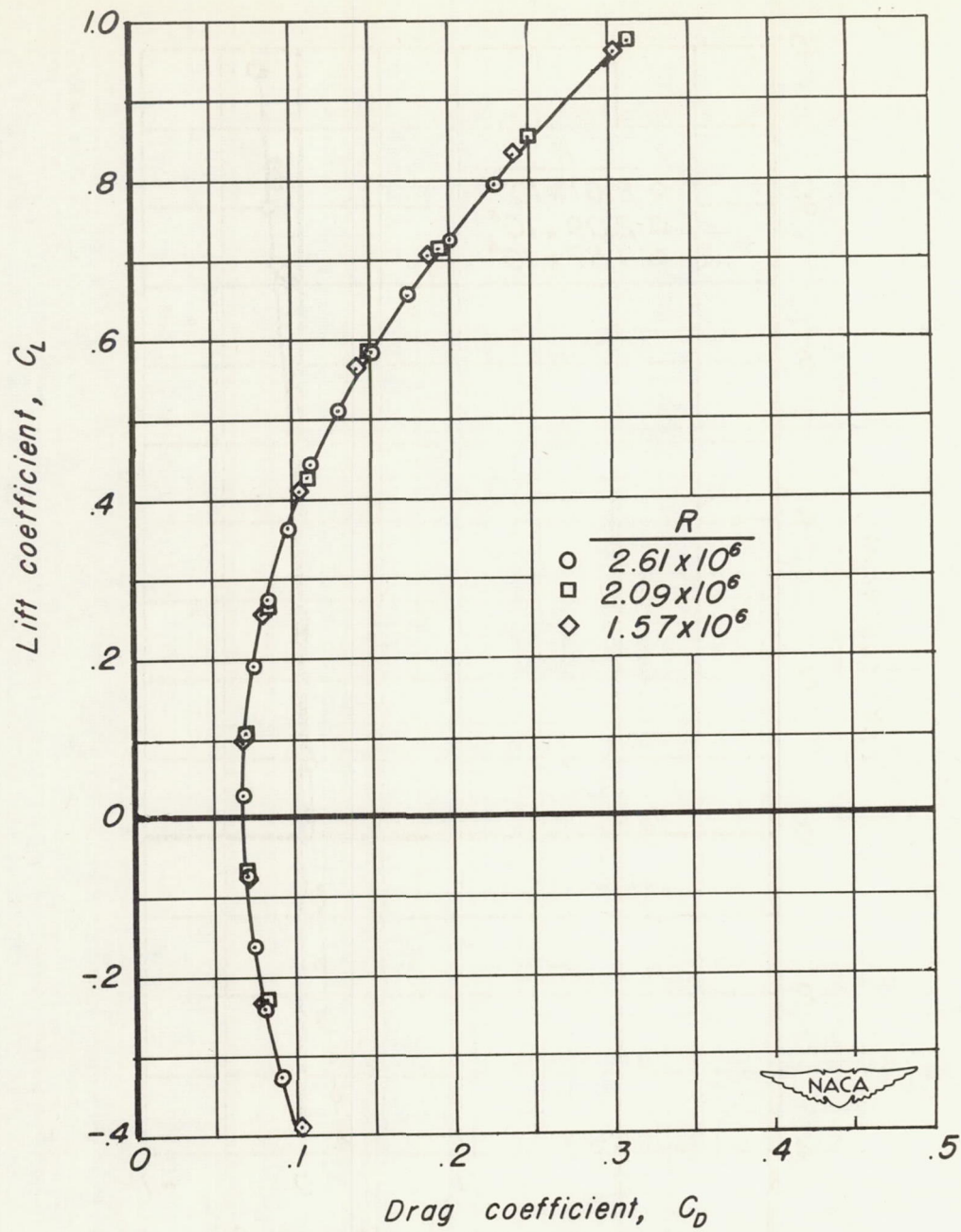
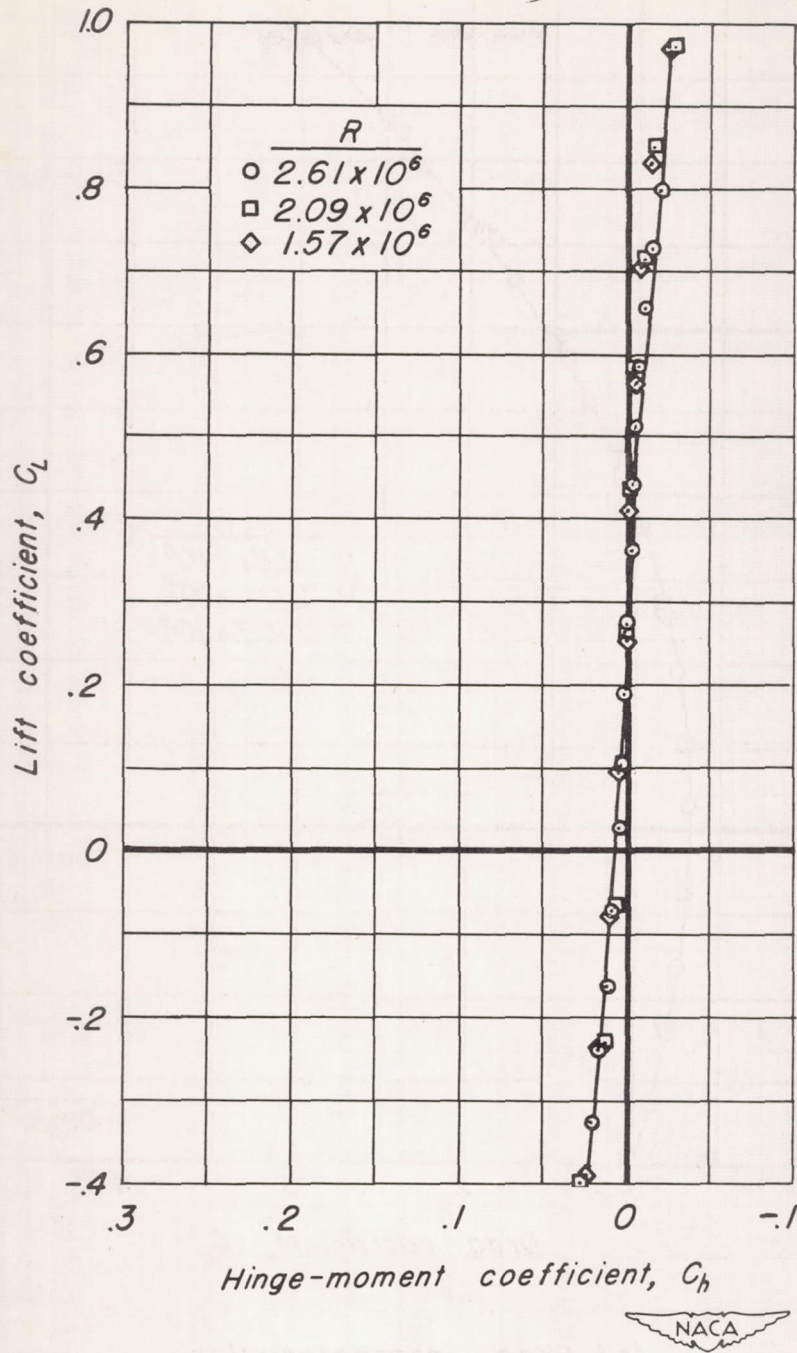


Figure 23.- Effect of Reynolds number on the longitudinal characteristics of the 1/12-scale Douglas X-3 configuration A at a Mach number of 1.30. $i_f = 0^\circ$.



(c) Drag characteristics.

Figure 23.-Continued.



(d) Hinge-moment characteristics.

Figure 23.- Concluded.

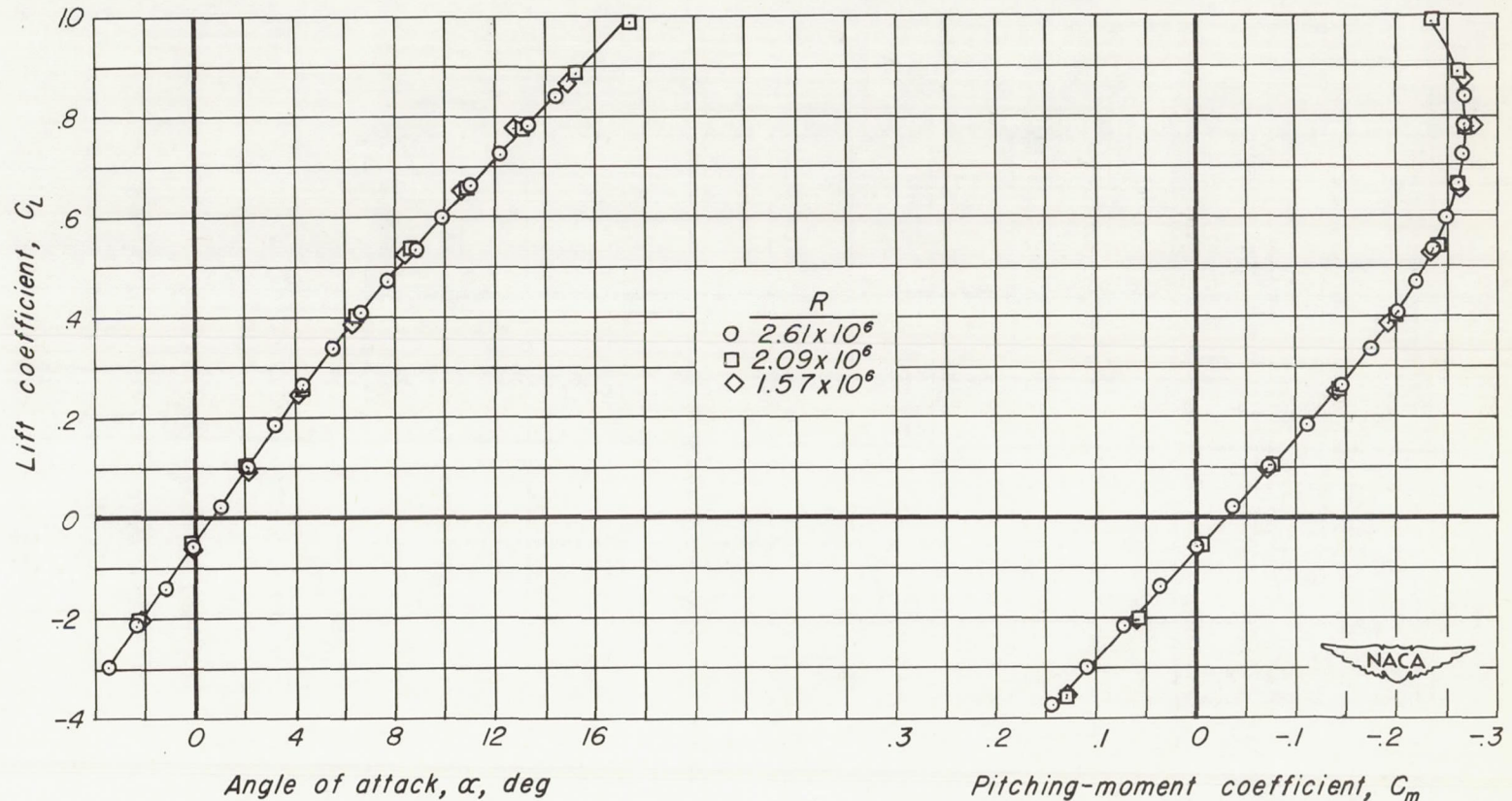
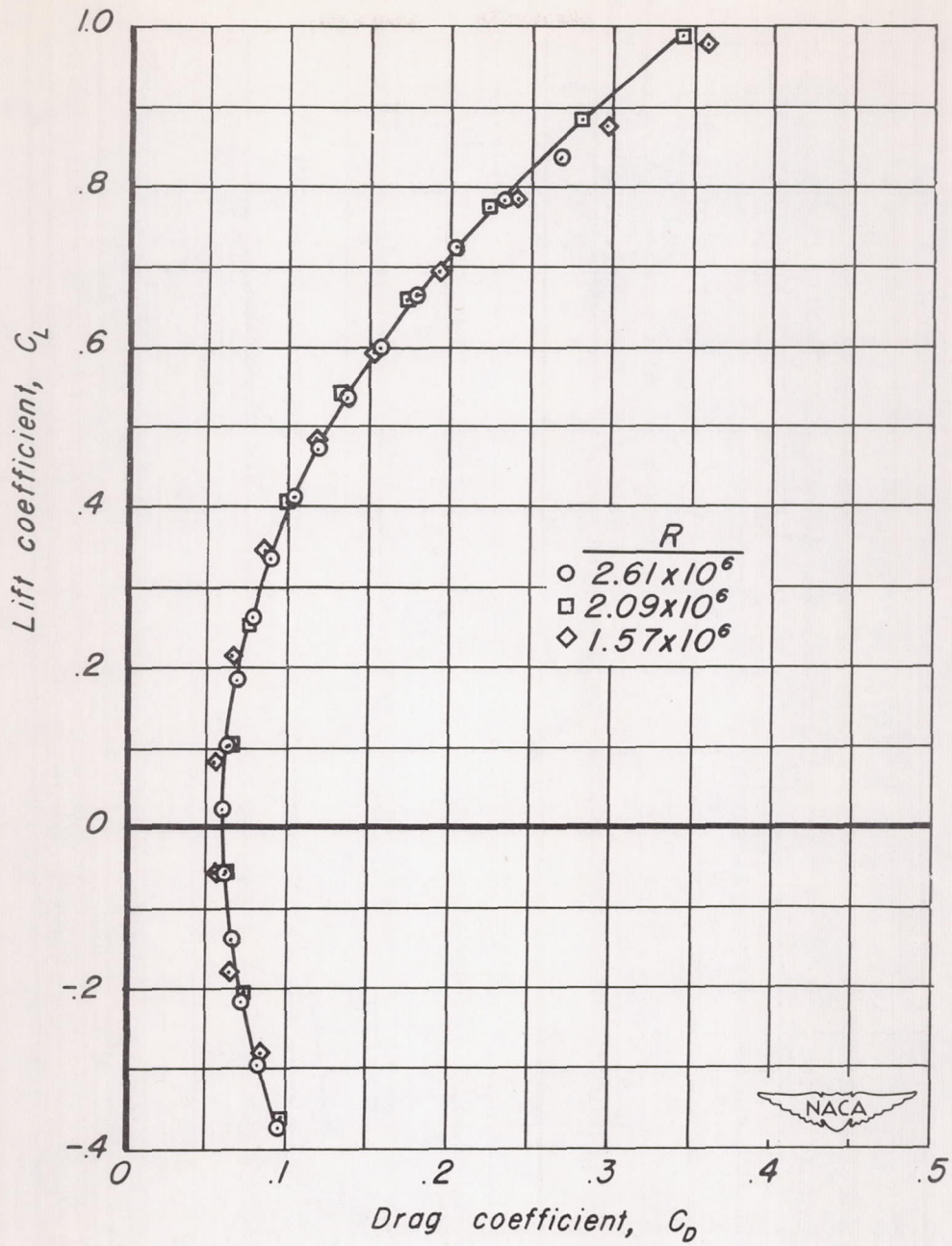
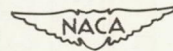
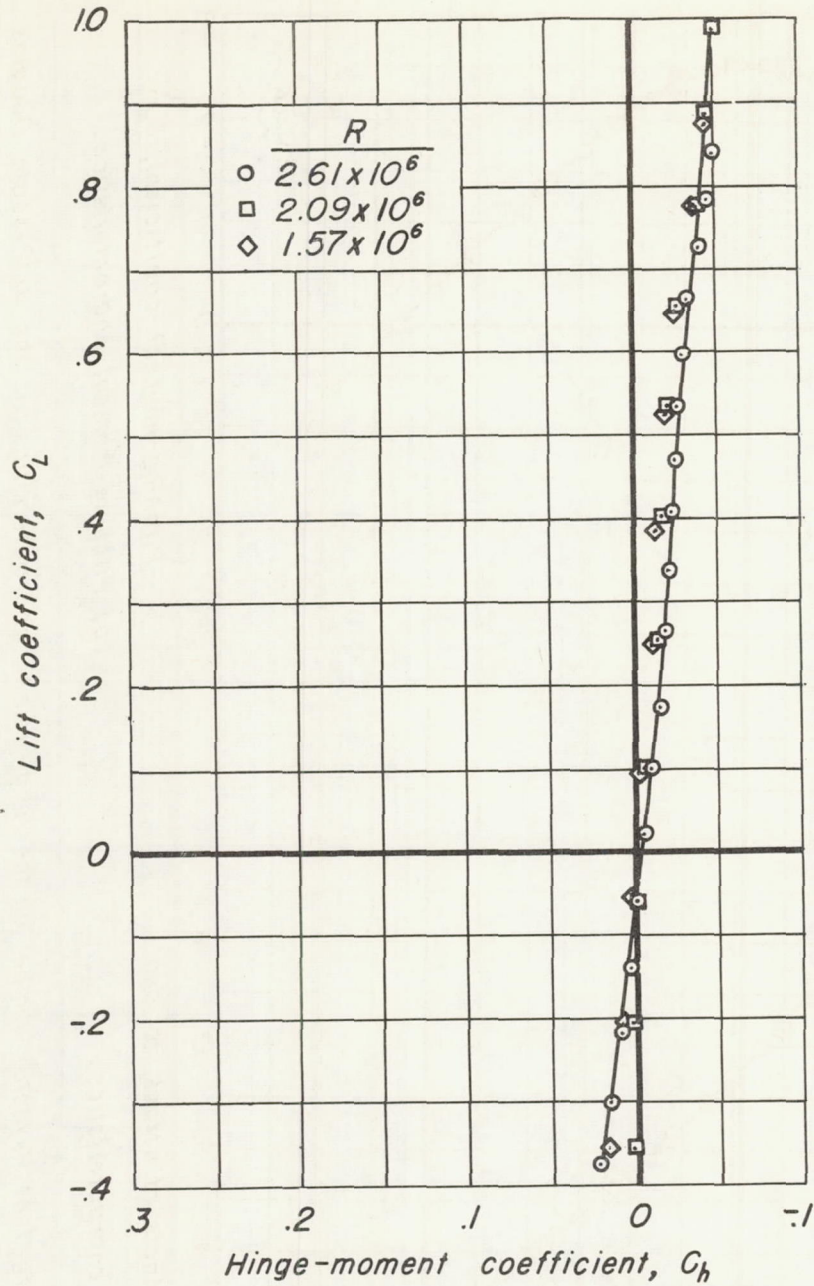


Figure 24.- Effect of Reynolds number on the longitudinal characteristics of the 1/12-scale Douglas X-3 configuration A at a Mach number of 1.50. $i_t = 0^\circ$.



(c) Drag characteristics.

Figure 24.- Continued.



(d) Hinge-moment characteristics.

Figure 24.- Concluded.

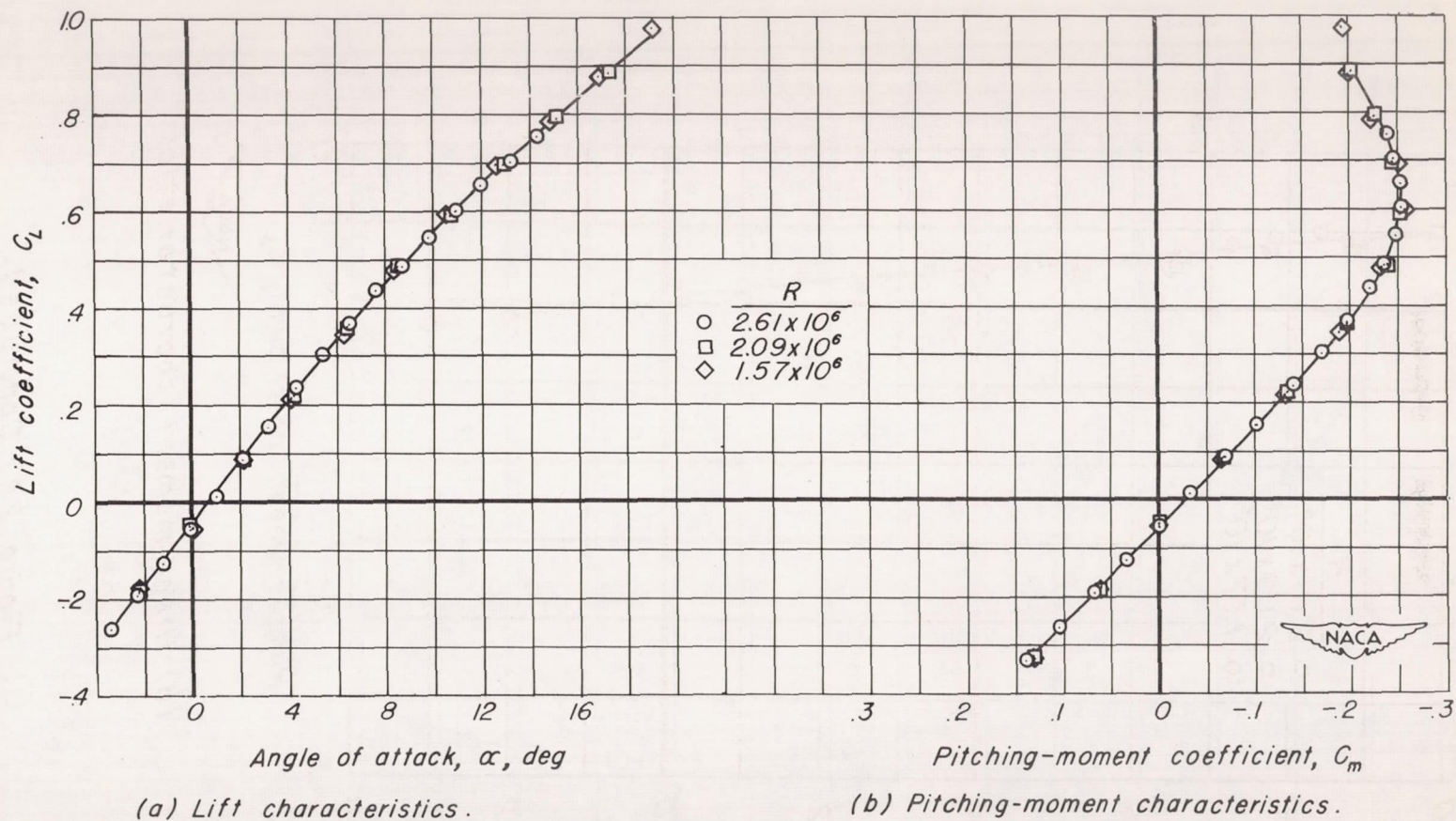
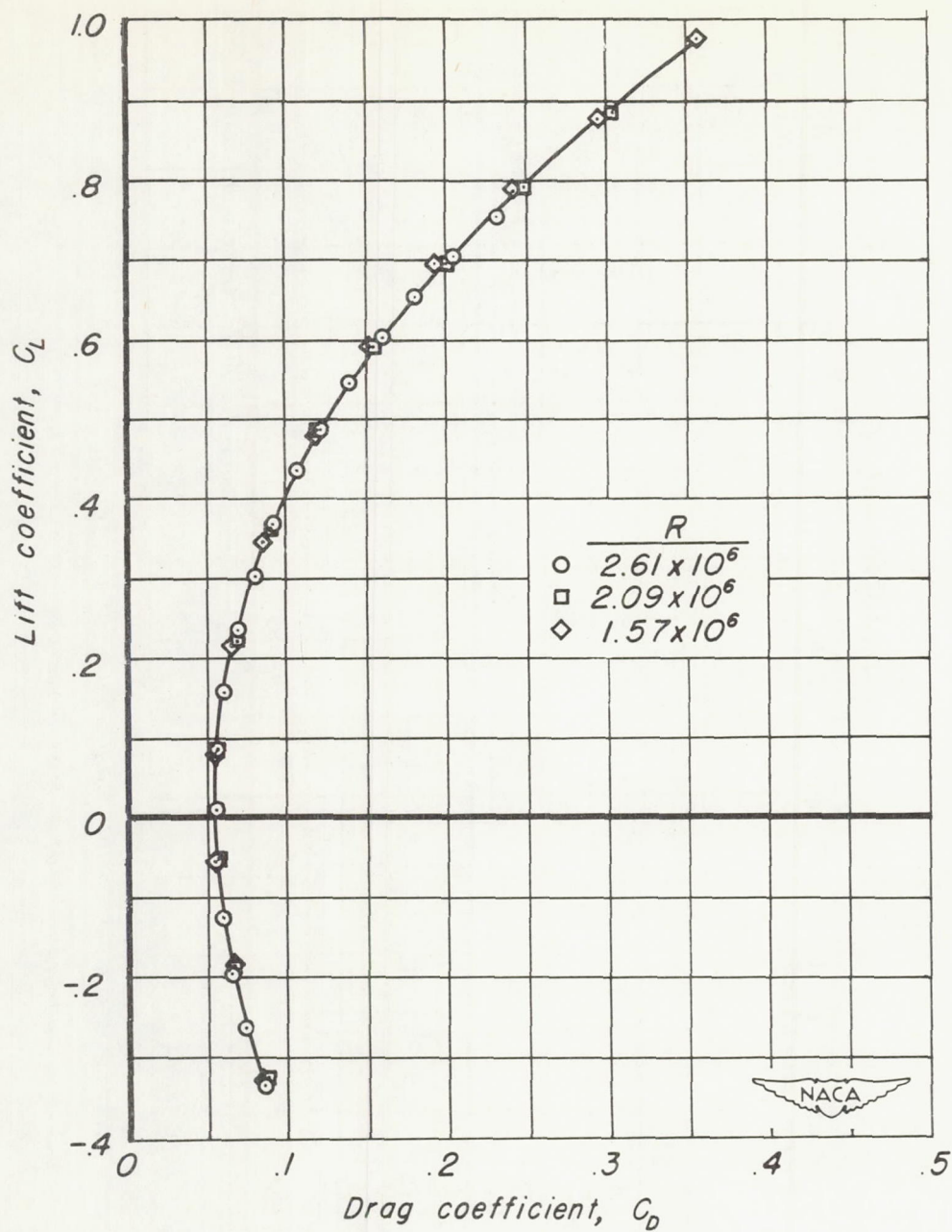
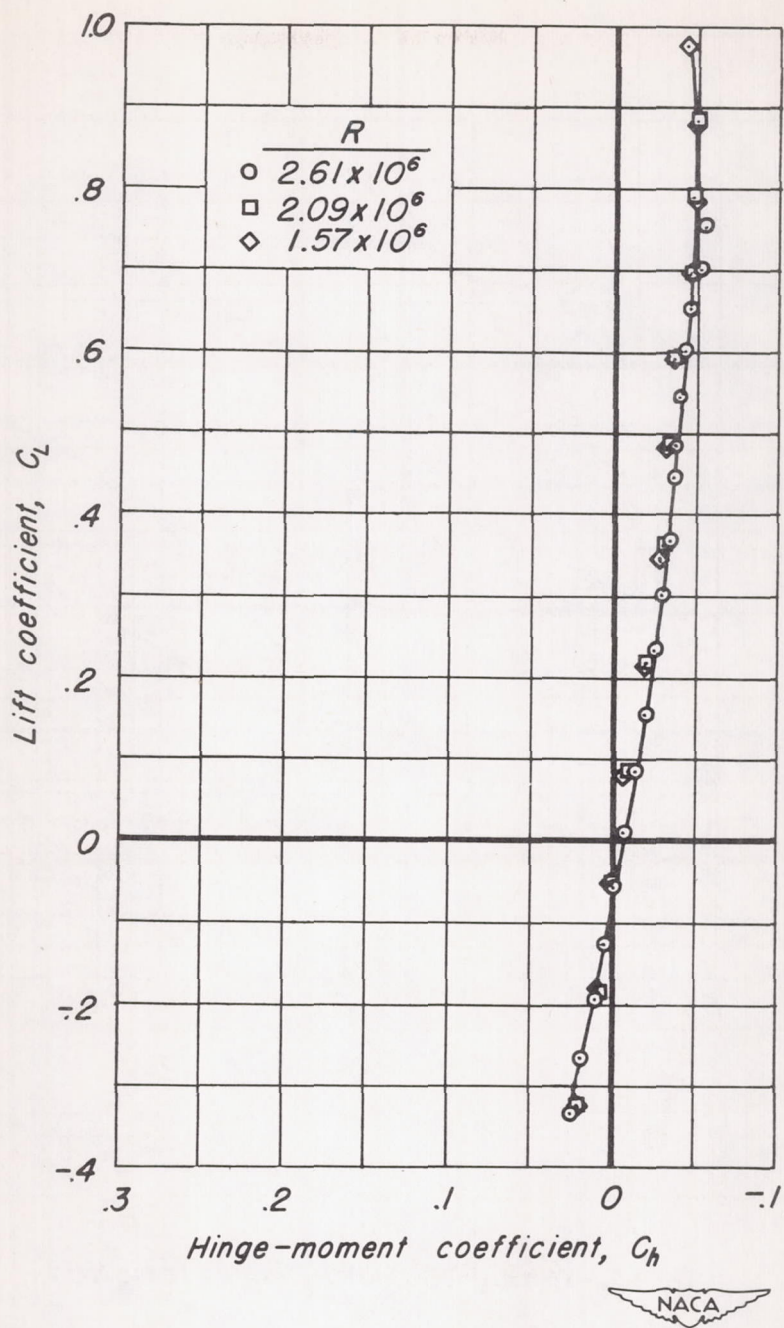


Figure 25.- Effect of Reynolds number on the longitudinal characteristics of the 1/12-scale Douglas X-3 configuration A at a Mach number of 1.70. $i_1 = 0^\circ$.



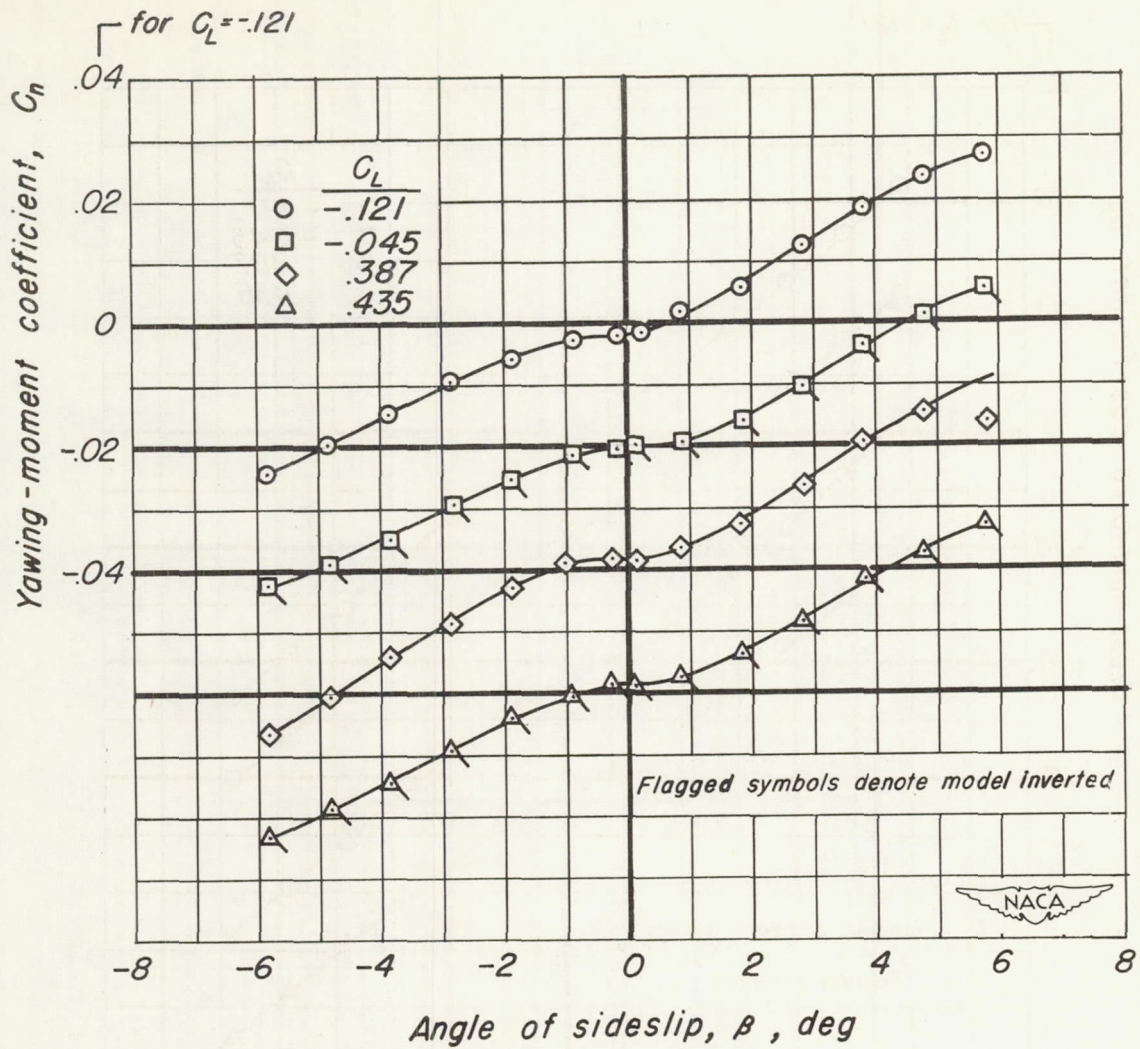
(c) Drag characteristics.

Figure 25.-Continued.



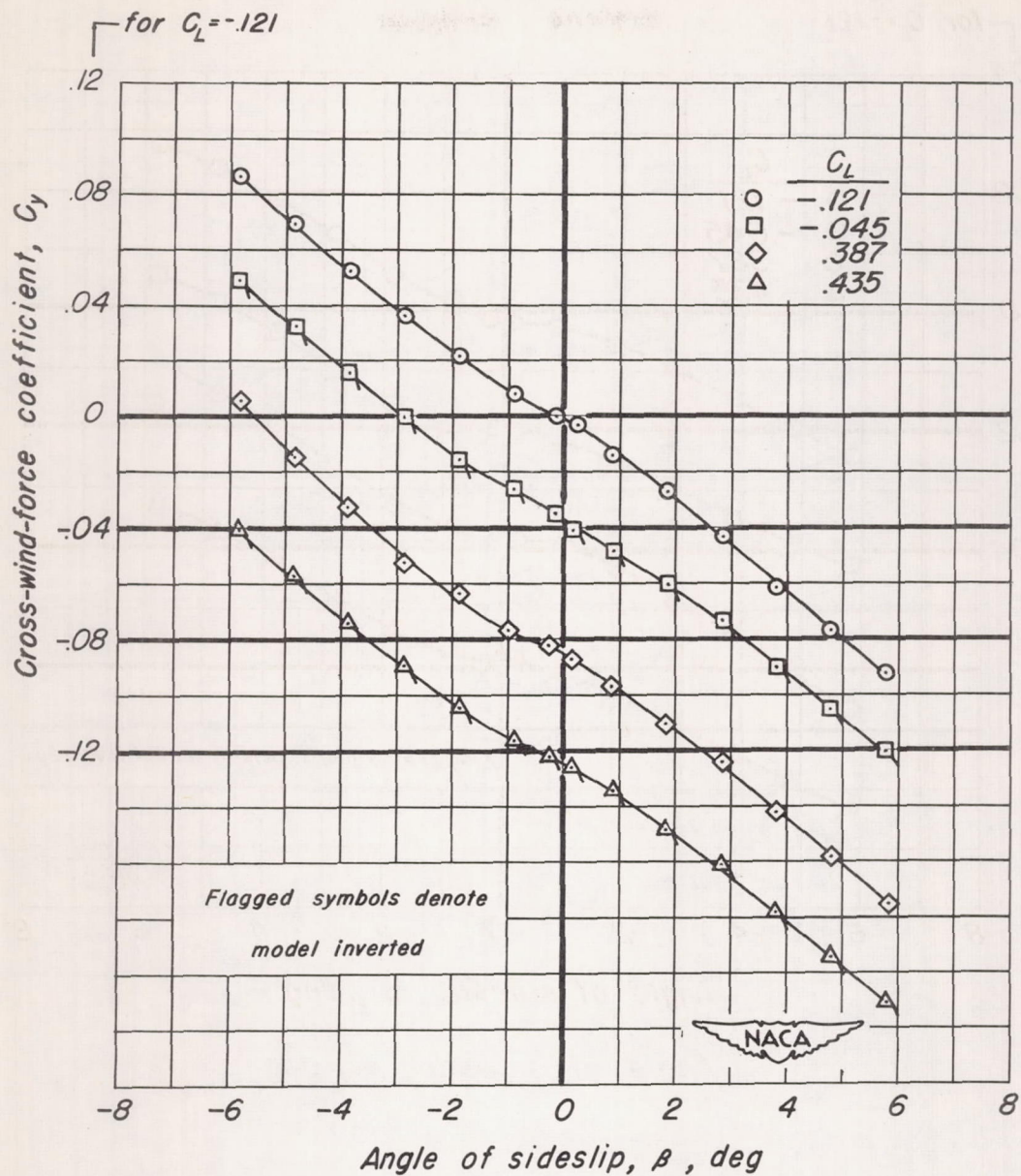
(d) Hinge-moment characteristics.

Figure 25.- Concluded.



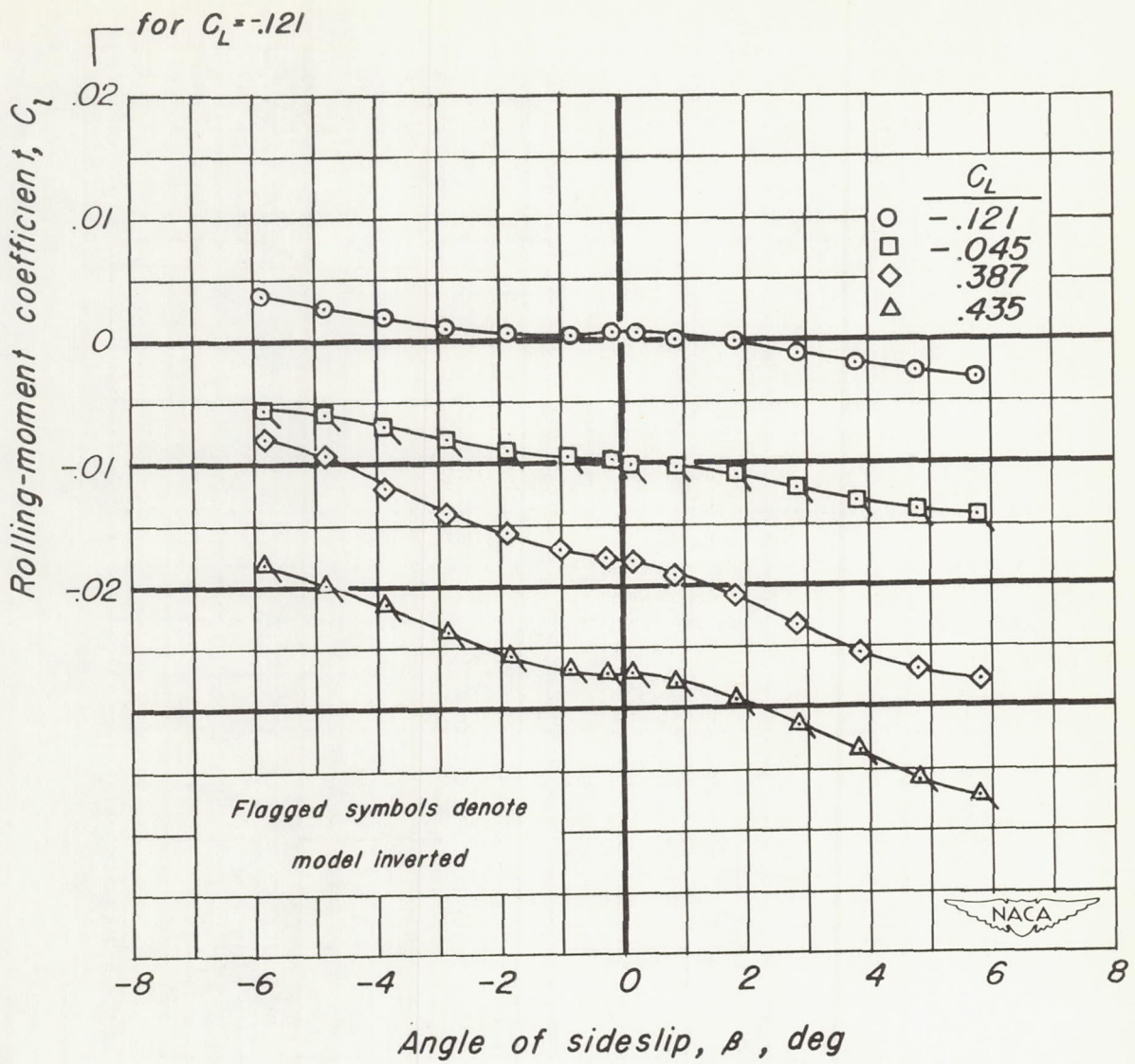
(a) Yawing-moment characteristics.

Figure 26.- Lateral and directional stability characteristics of the 1/12-scale Douglas X-3 configuration A at a Mach number of 0.90. $R = 2.29 \times 10^6$.



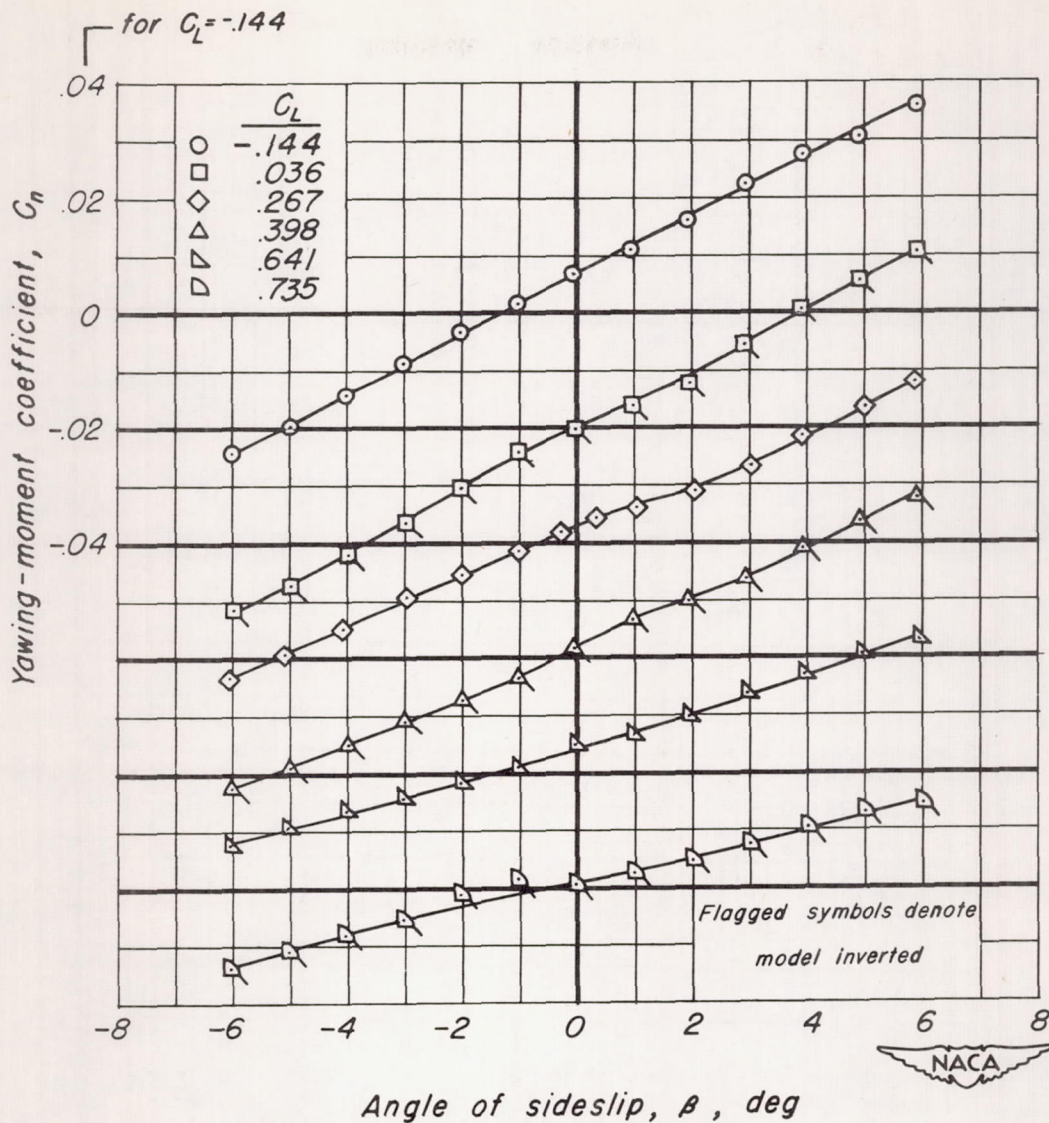
(b) Side-force characteristics.

Figure 26.- Continued.



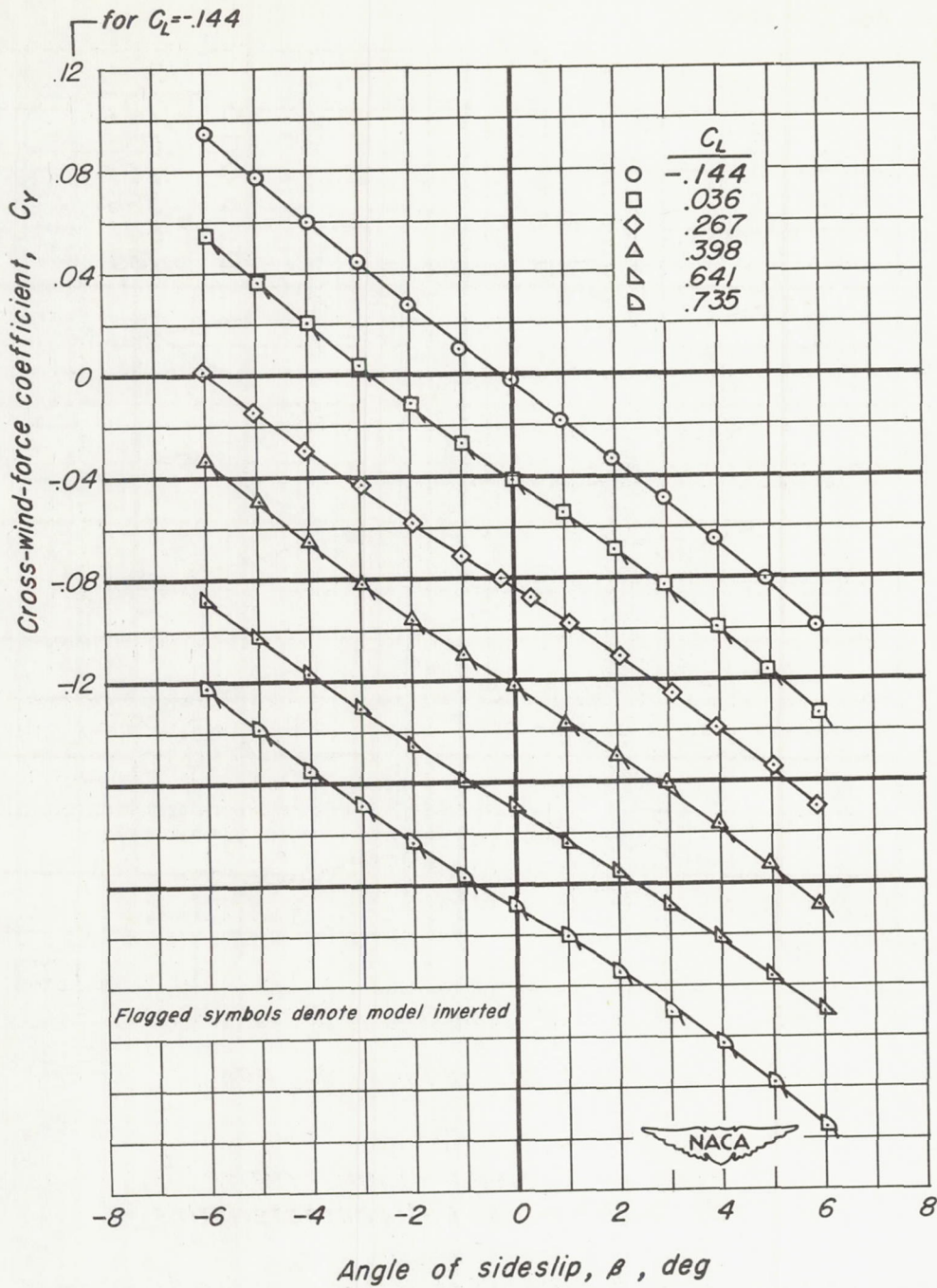
(c) Rolling-moment characteristics.

Figure 26.- Concluded.



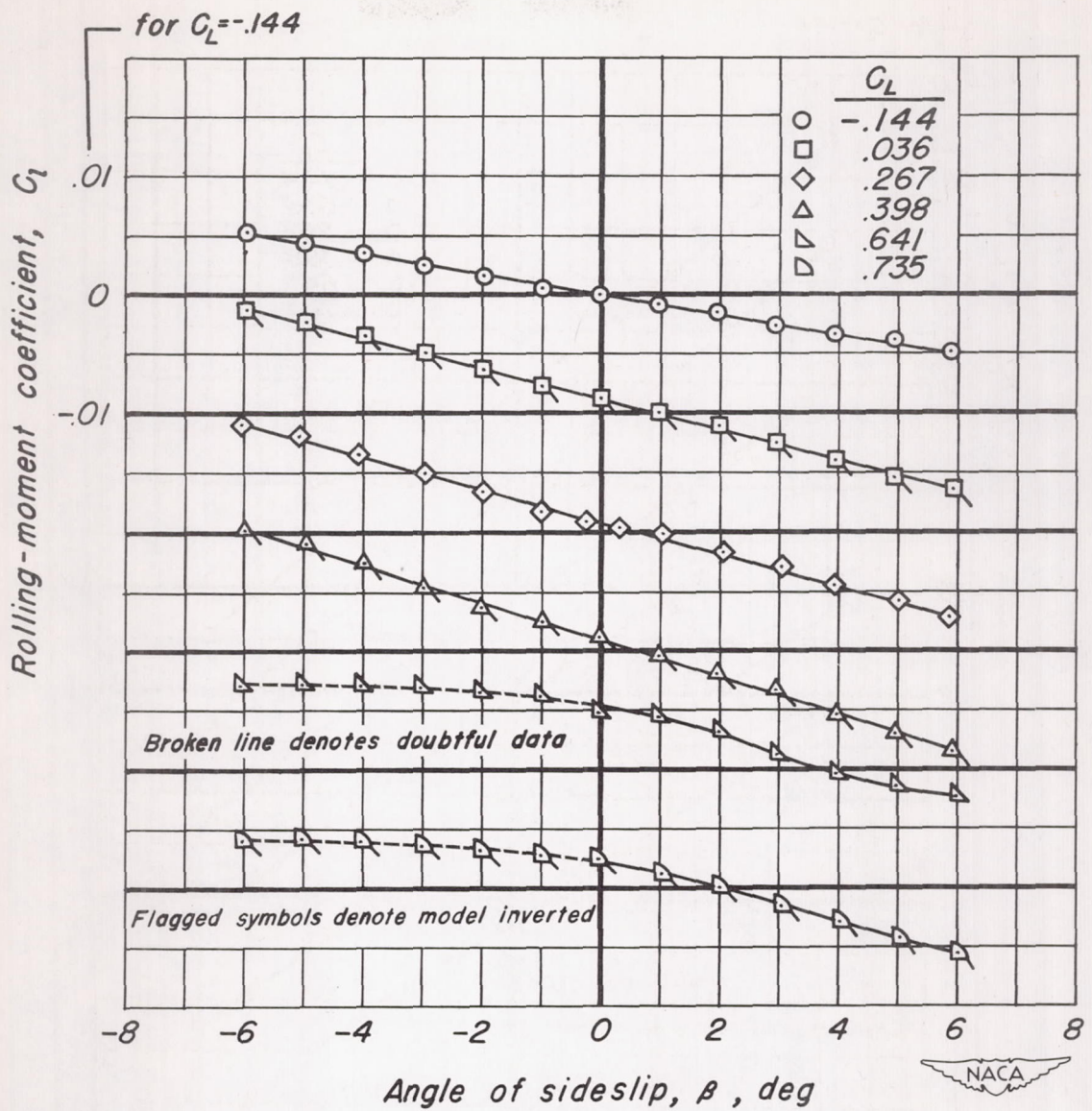
(a) Yawing-moment characteristics.

Figure 27.- Lateral and directional stability characteristics of the 1/12-scale Douglas X-3 configuration A at a Mach number of 1.40. $R = 2.09 \times 10^6$



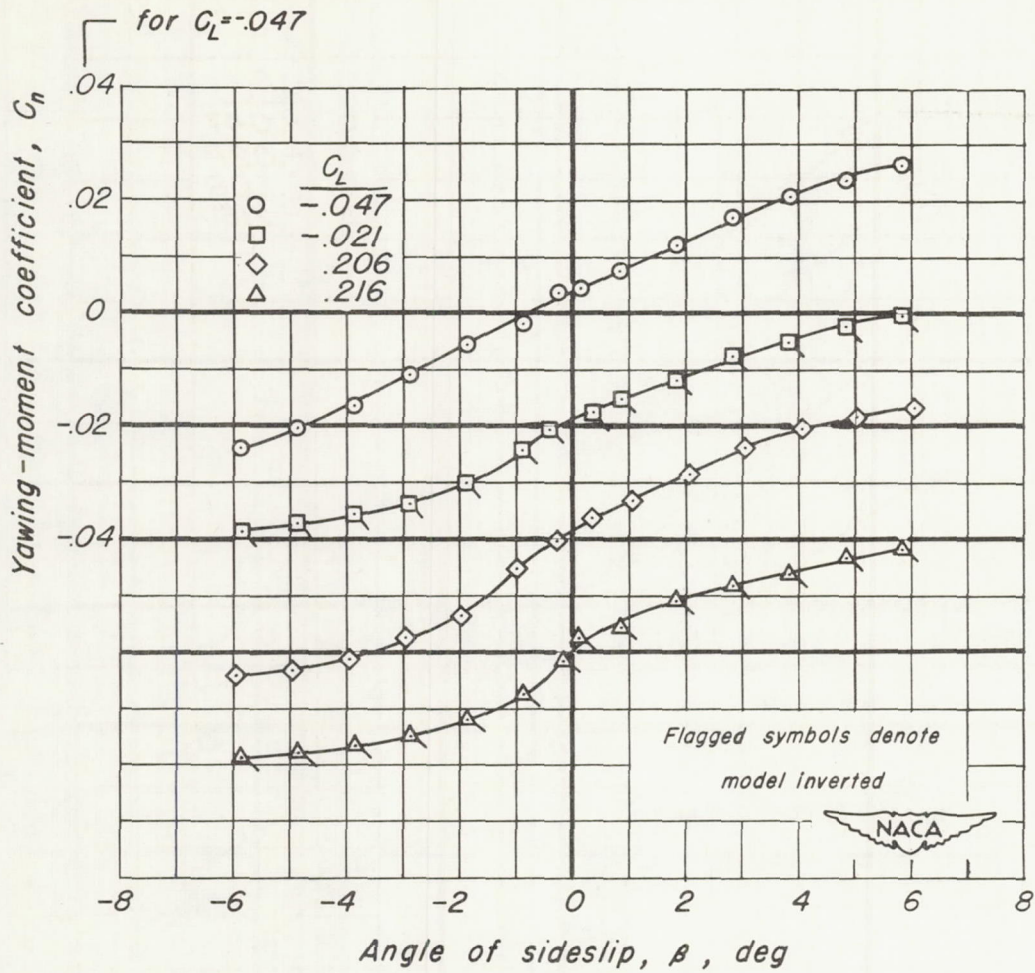
(b) Side-force characteristics.

Figure 27.- Continued.



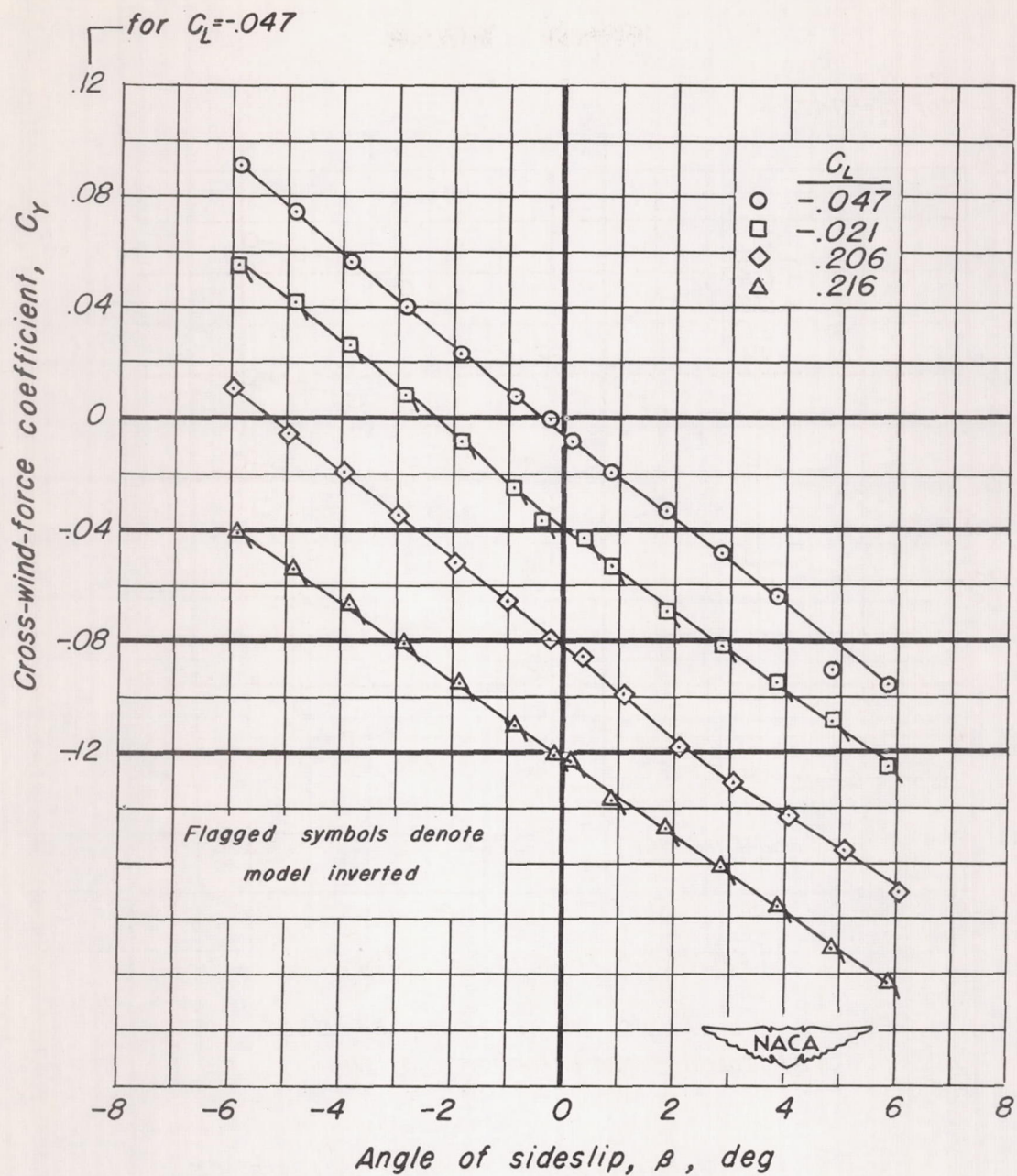
(c) Rolling-moment characteristics.

Figure 27.- Concluded.



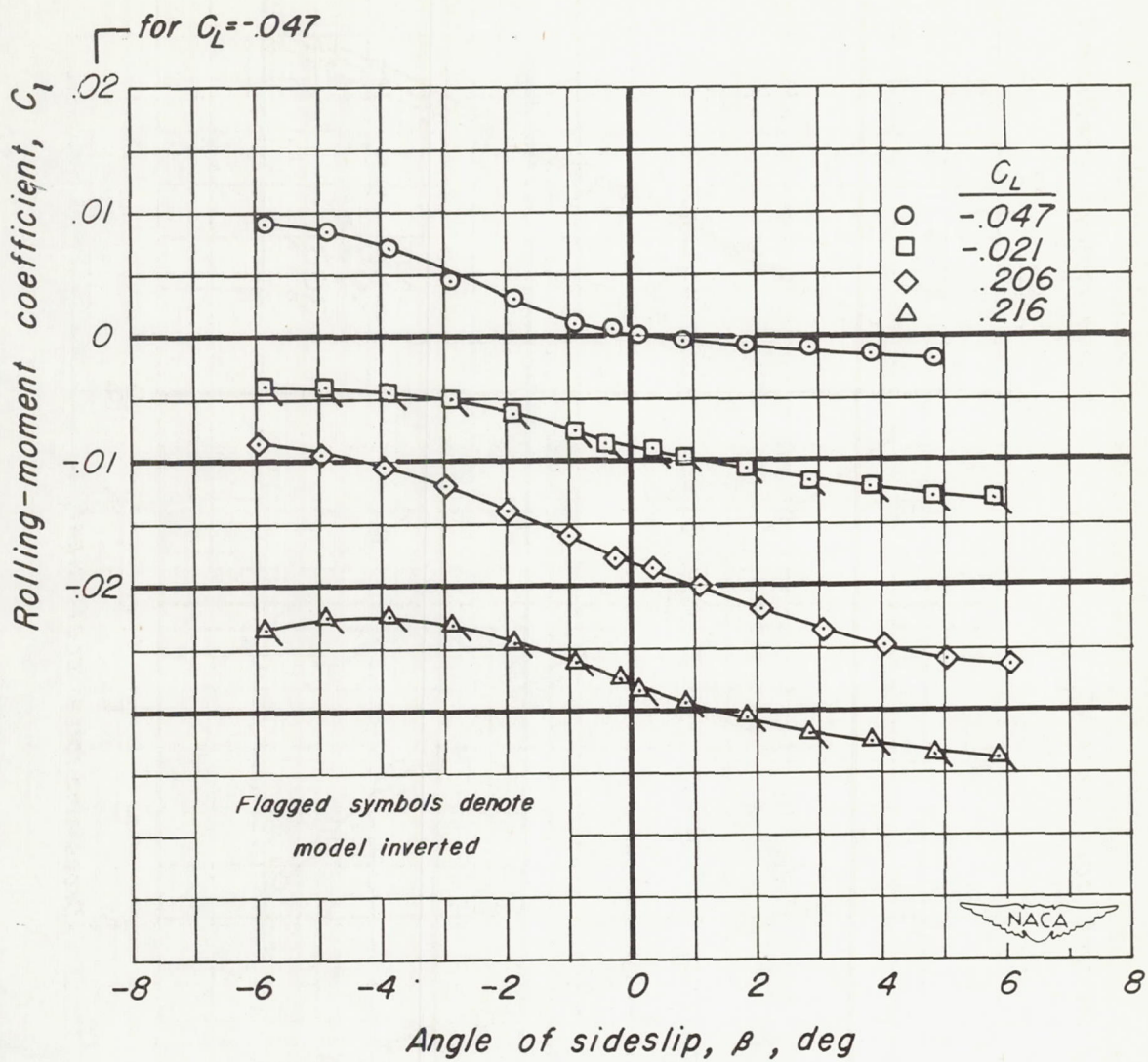
(a) Yawing-moment characteristics.

Figure 28.- Lateral and directional stability characteristics of the 1/12-scale Douglas X-3 configuration A at a Mach number of 1.91. $R = 0.98 \times 10^6$.



(b) Side-force characteristics.

Figure 28.- Continued.



(c) Rolling-moment characteristics.

Figure 28.- Concluded.

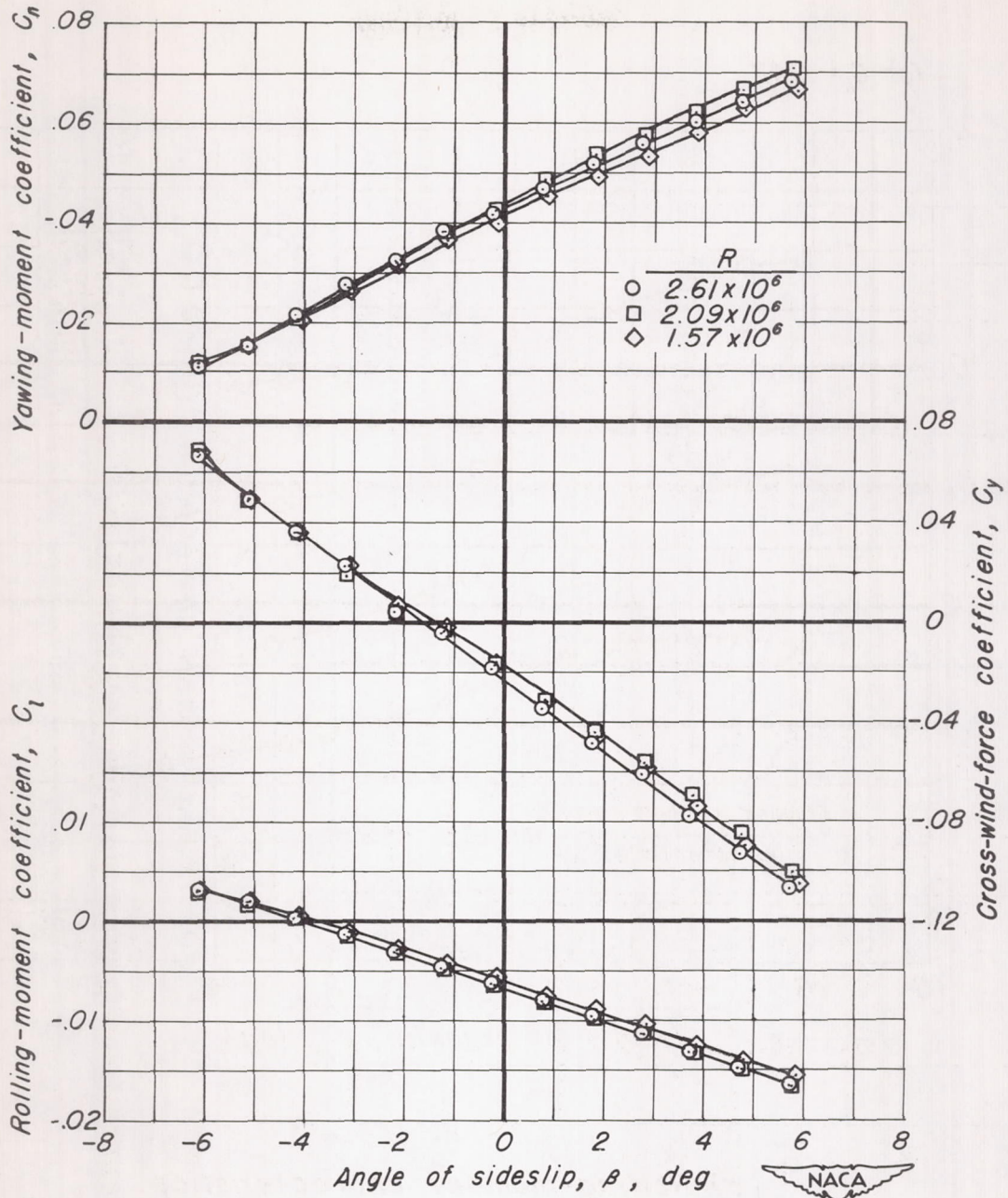
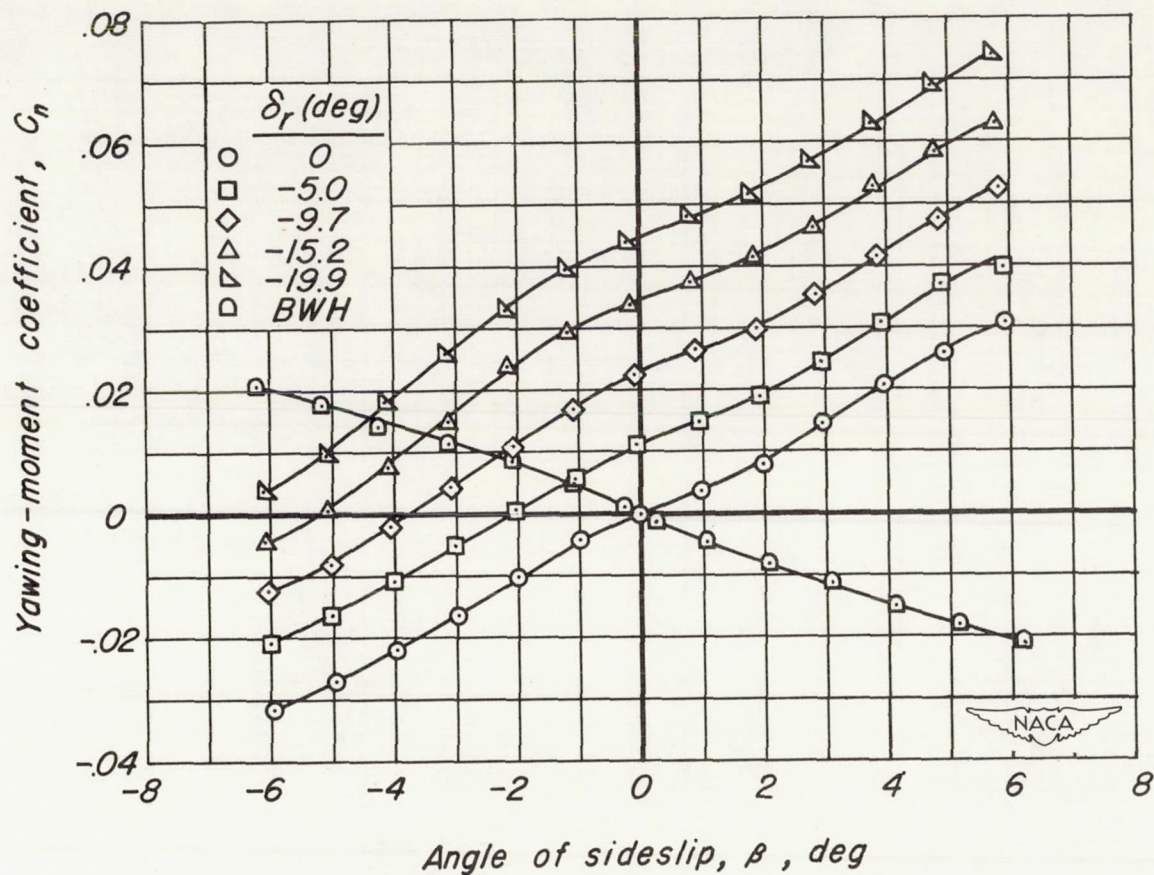
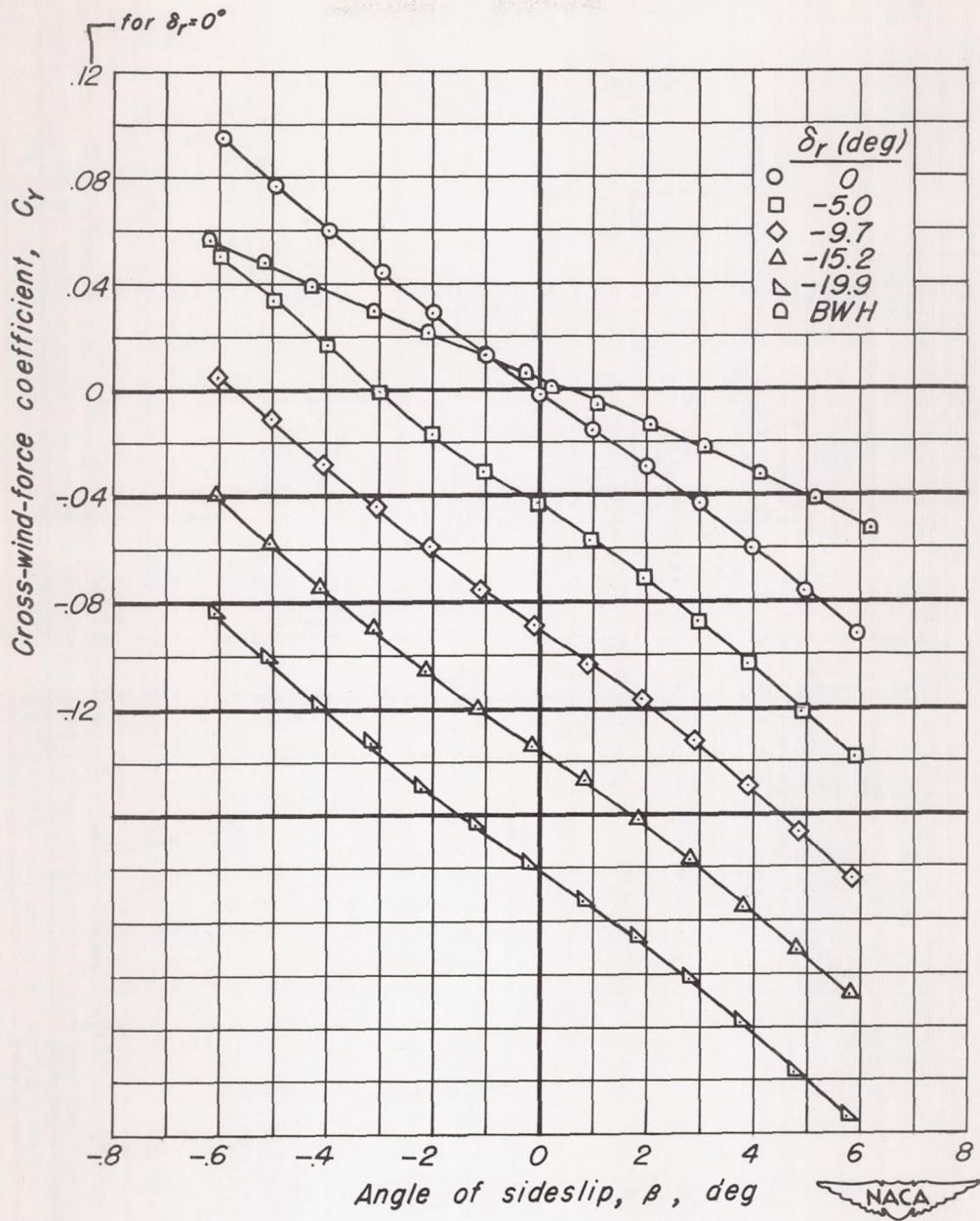


Figure 29.- Effect of Reynolds number on the lateral and directional characteristics of the 1/12-scale Douglas X-3 configuration A .
 $M = 1.40$; $\delta_r = -19.9^\circ$.



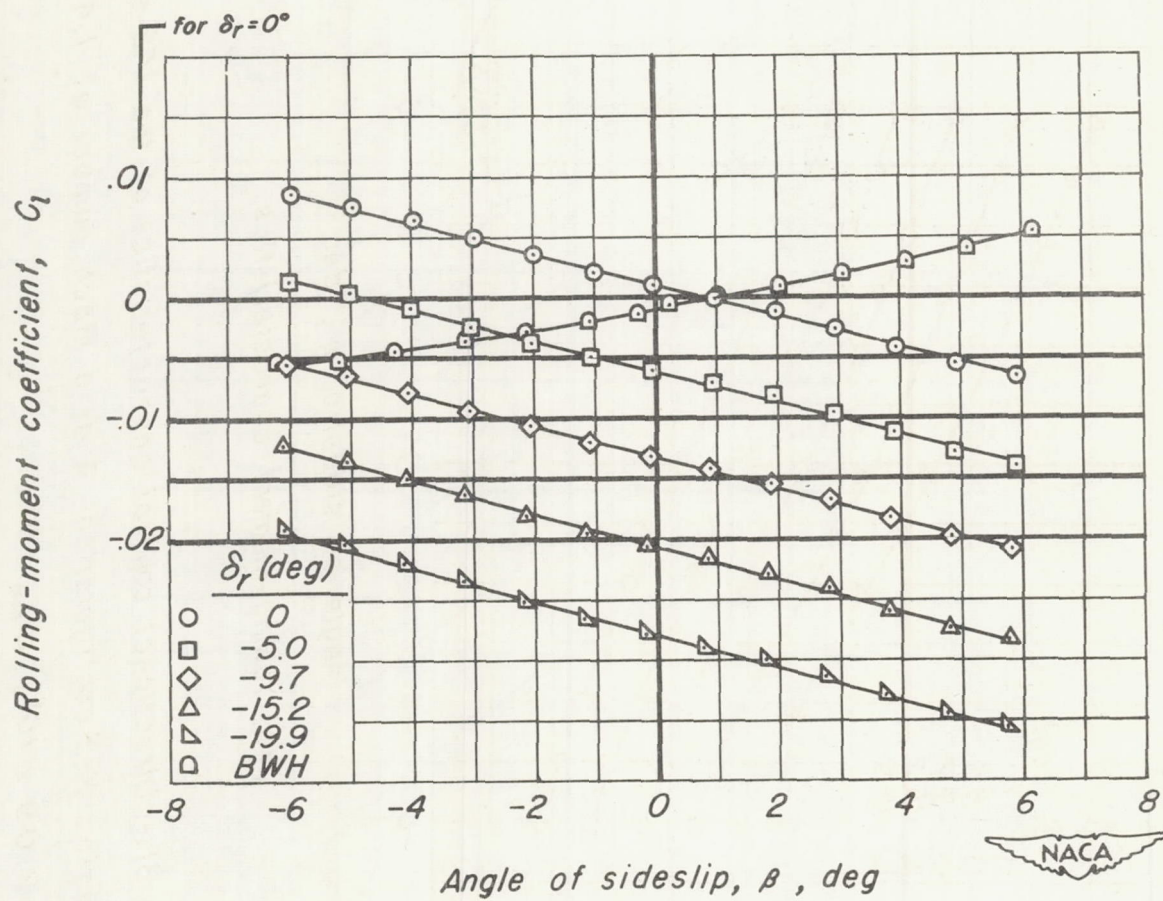
(a) Yawing-moment characteristics.

Figure 30.- Directional control characteristics of the 1/12-scale Douglas X-3 configuration A at a Mach number of 1.40. $R = 2.09 \times 10^6$; $\alpha_{nom} = 0^\circ$.



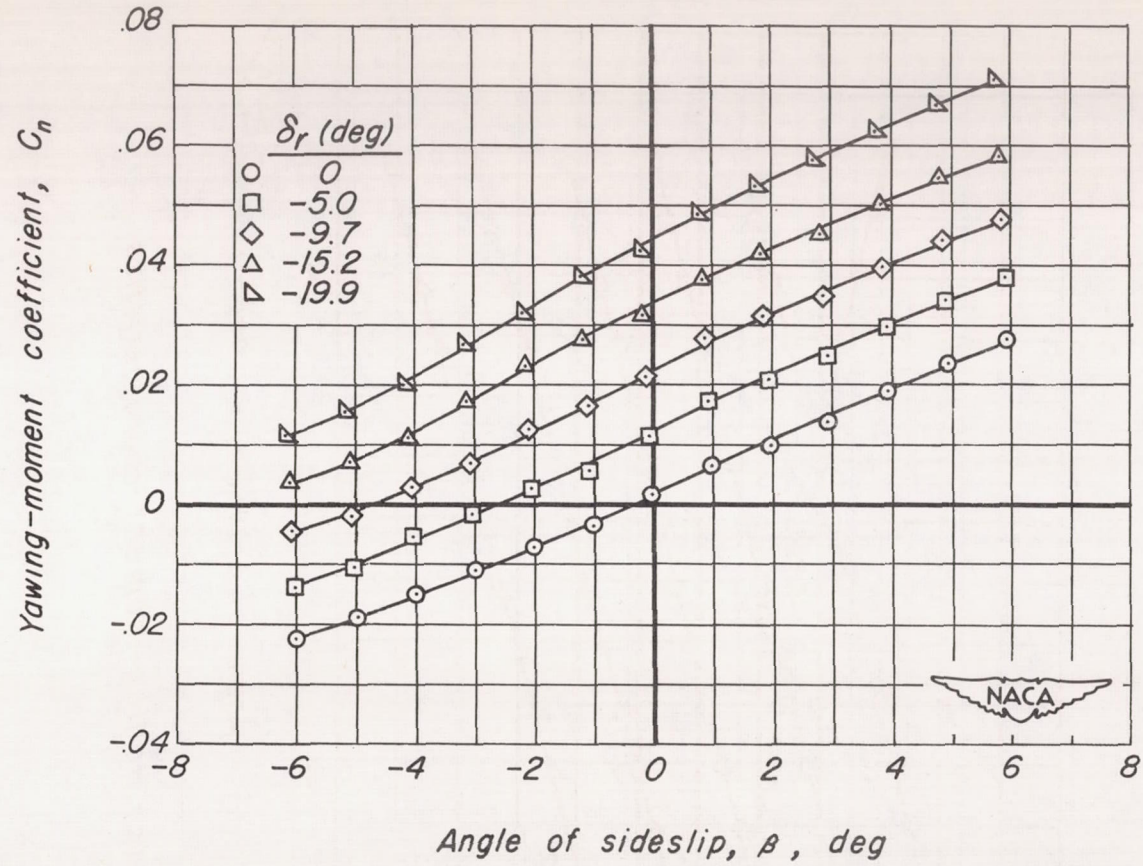
(b) Side-force characteristics.

Figure 30. - Continued.



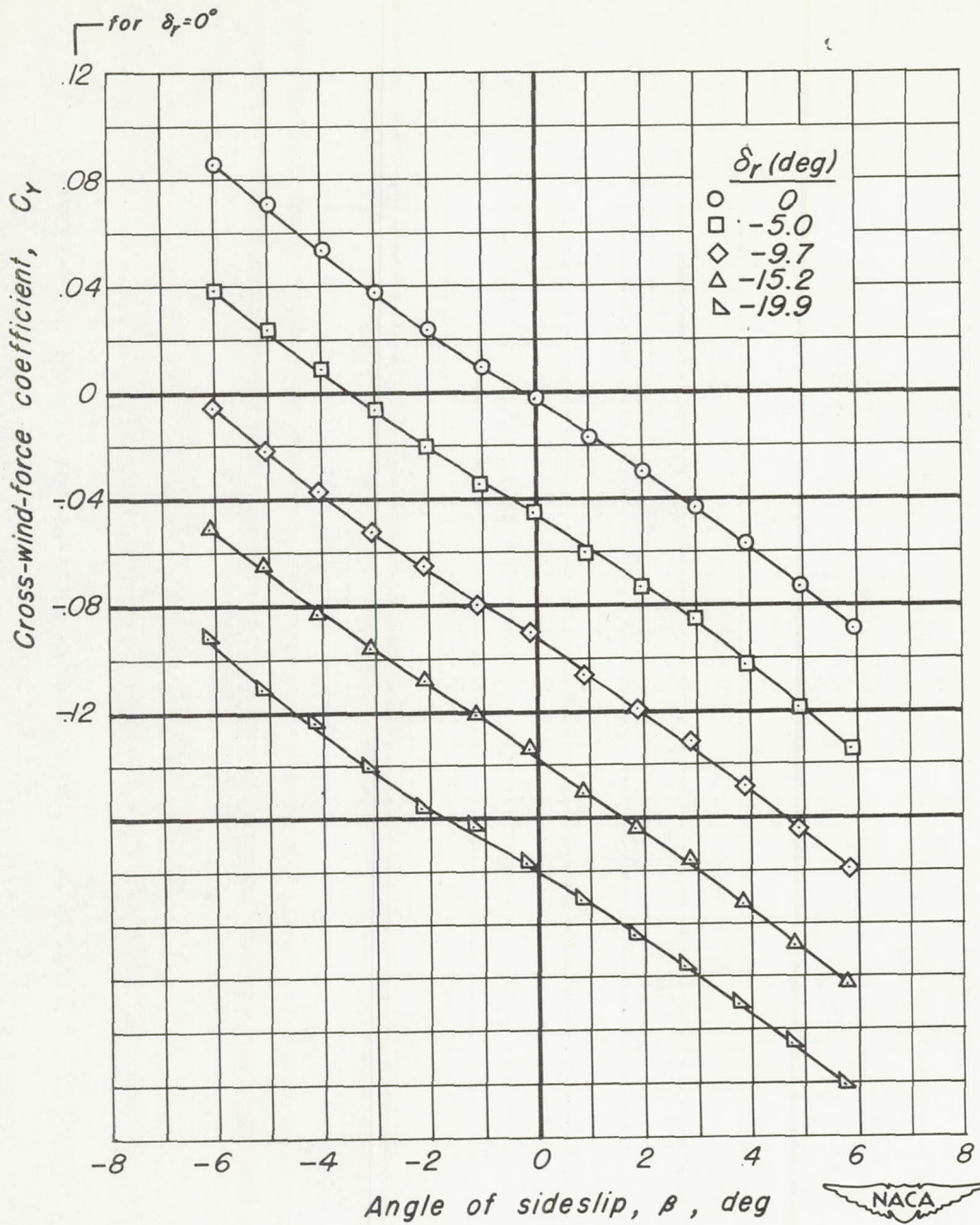
(c) Rolling-moment characteristics.

Figure 30.- Concluded.



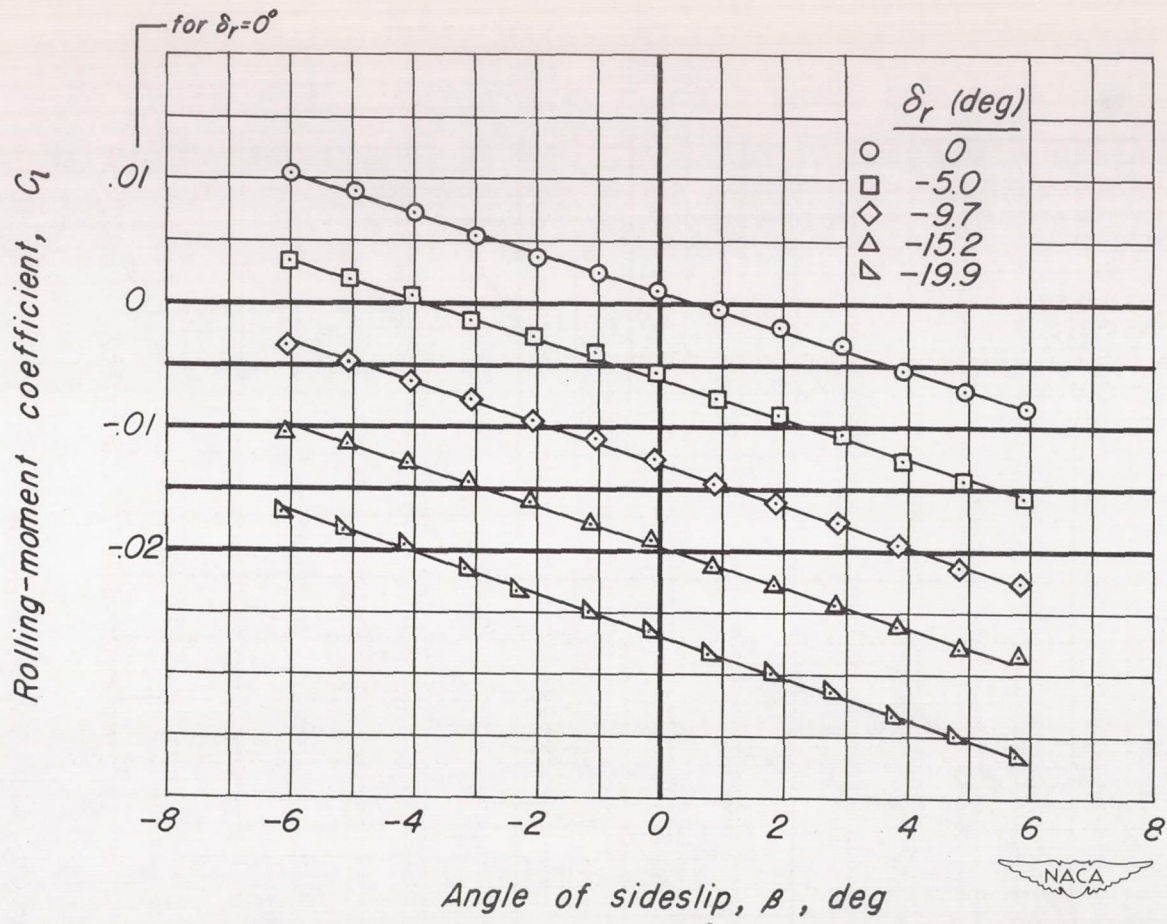
(a) Yawing-moment characteristics.

Figure 31.- Directional control characteristics of the 1/12-scale Douglas X-3 configuration A at a Mach number of 1.40. $R = 2.09 \times 10^6$; $\alpha_{nom} = 5^\circ$.



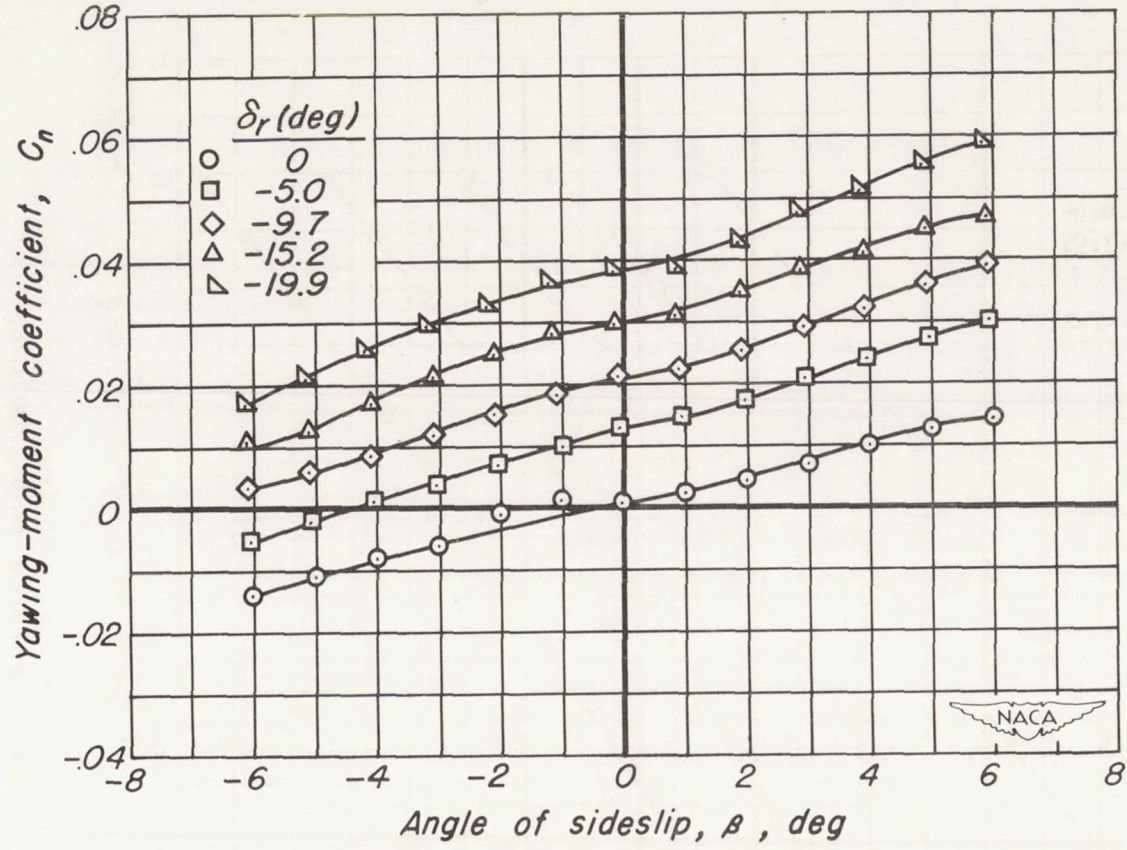
(b) Side-force characteristics.

Figure 31.- Continued.



(c) Rolling-moment characteristics.

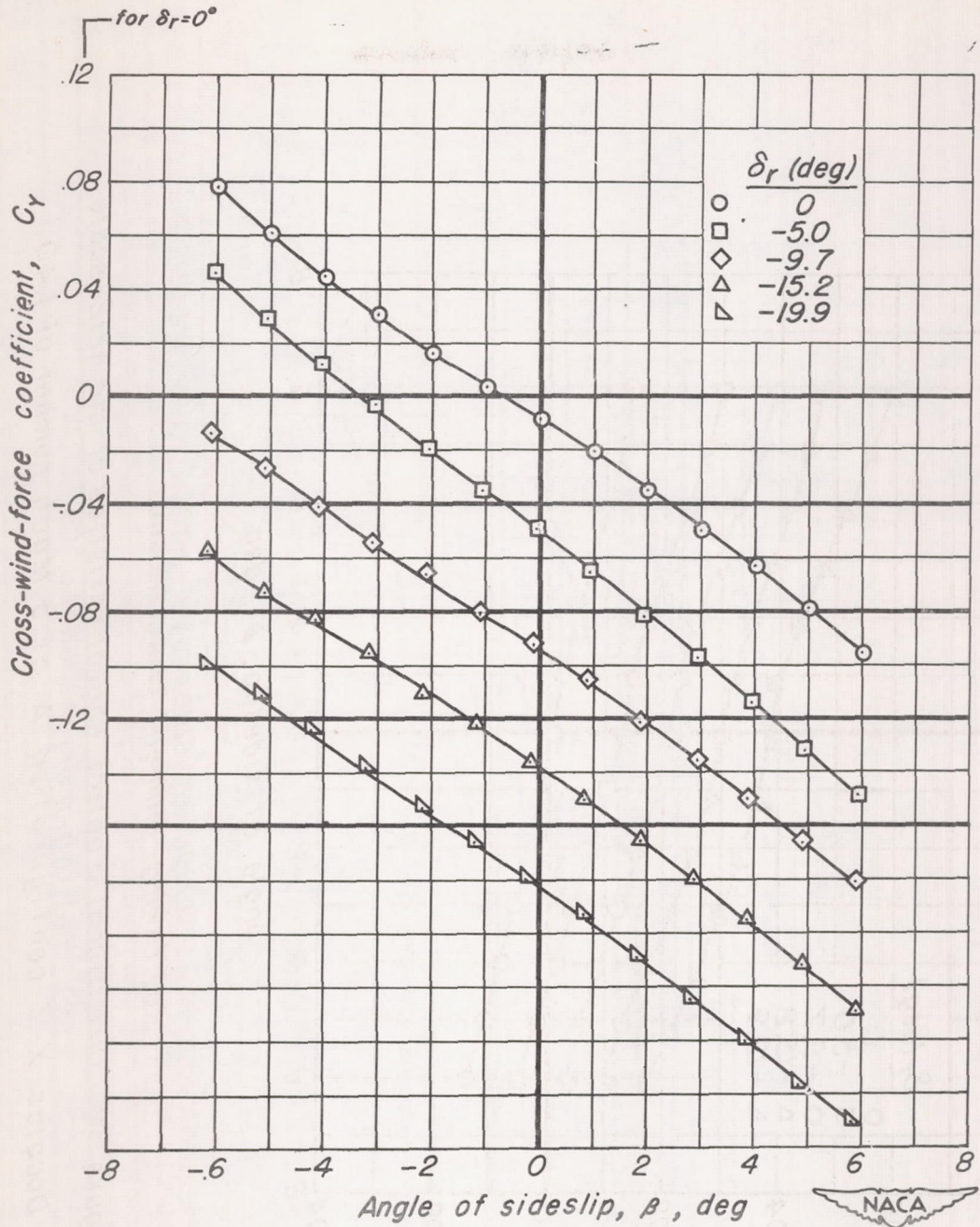
Figure 31.- Concluded.



(a) Yawing-moment characteristics.

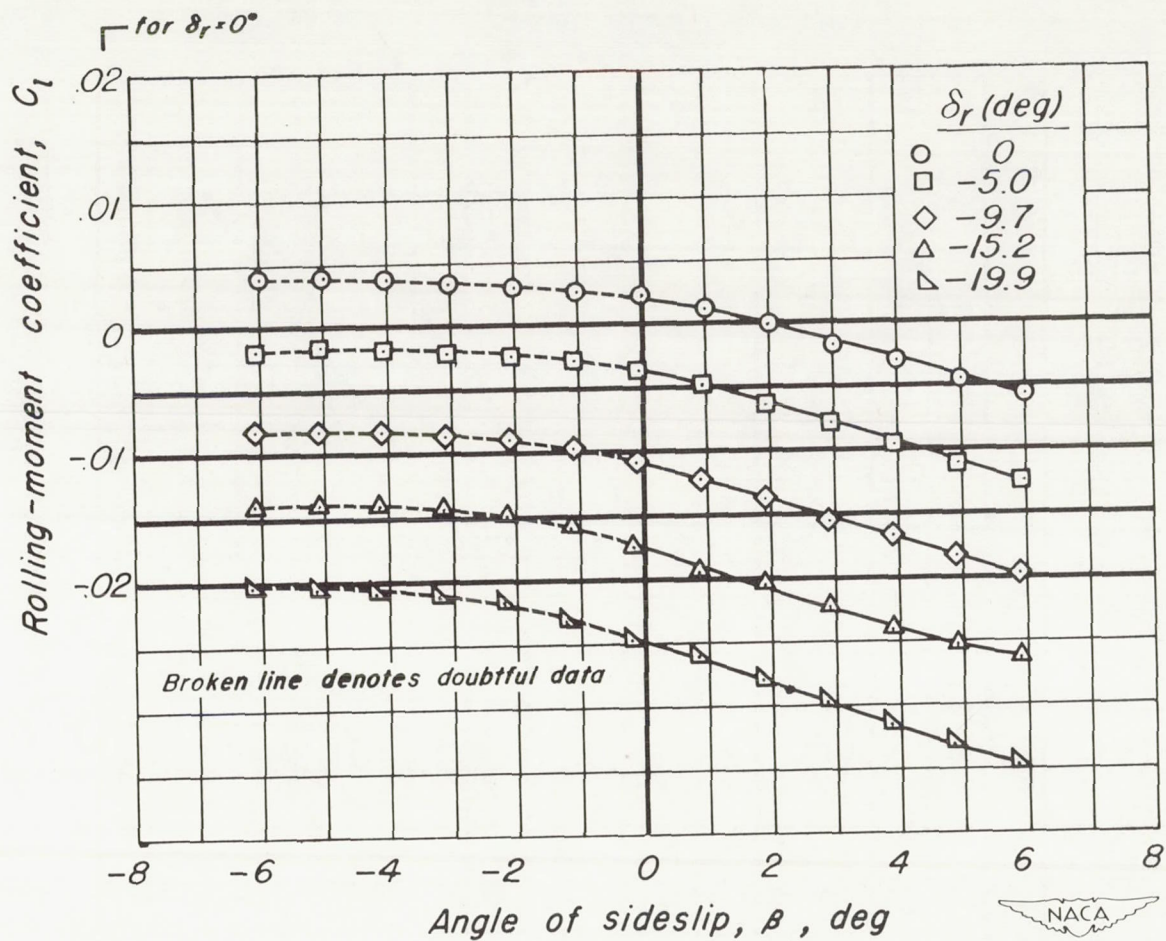
Figure 32.- Directional control characteristics of the 1/12-scale Douglas X-3 configuration A at a Mach number of 1.40.

$R = 2.09 \times 10^6$; $\alpha_{nom} = 10^\circ$.



(b) Side-force characteristics.

Figure 32.- Continued.



(c) Rolling-moment characteristics.

Figure 32.- Concluded.

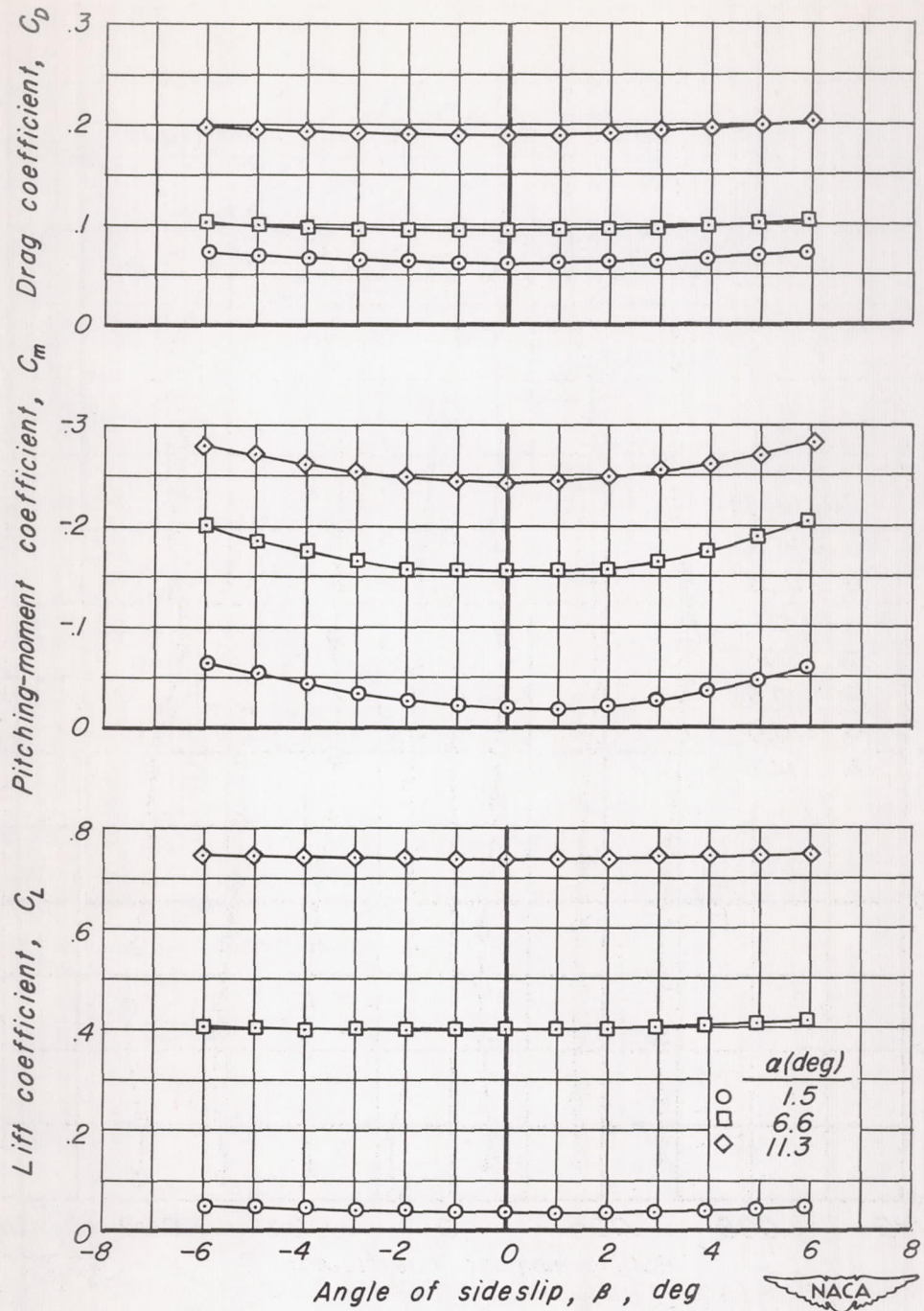


Figure 33.- Effect of sideslip angle on the longitudinal characteristics of the 1/12-scale Douglas X-3 configuration A . $R = 2.09 \times 10^6$; $M = 1.40$.

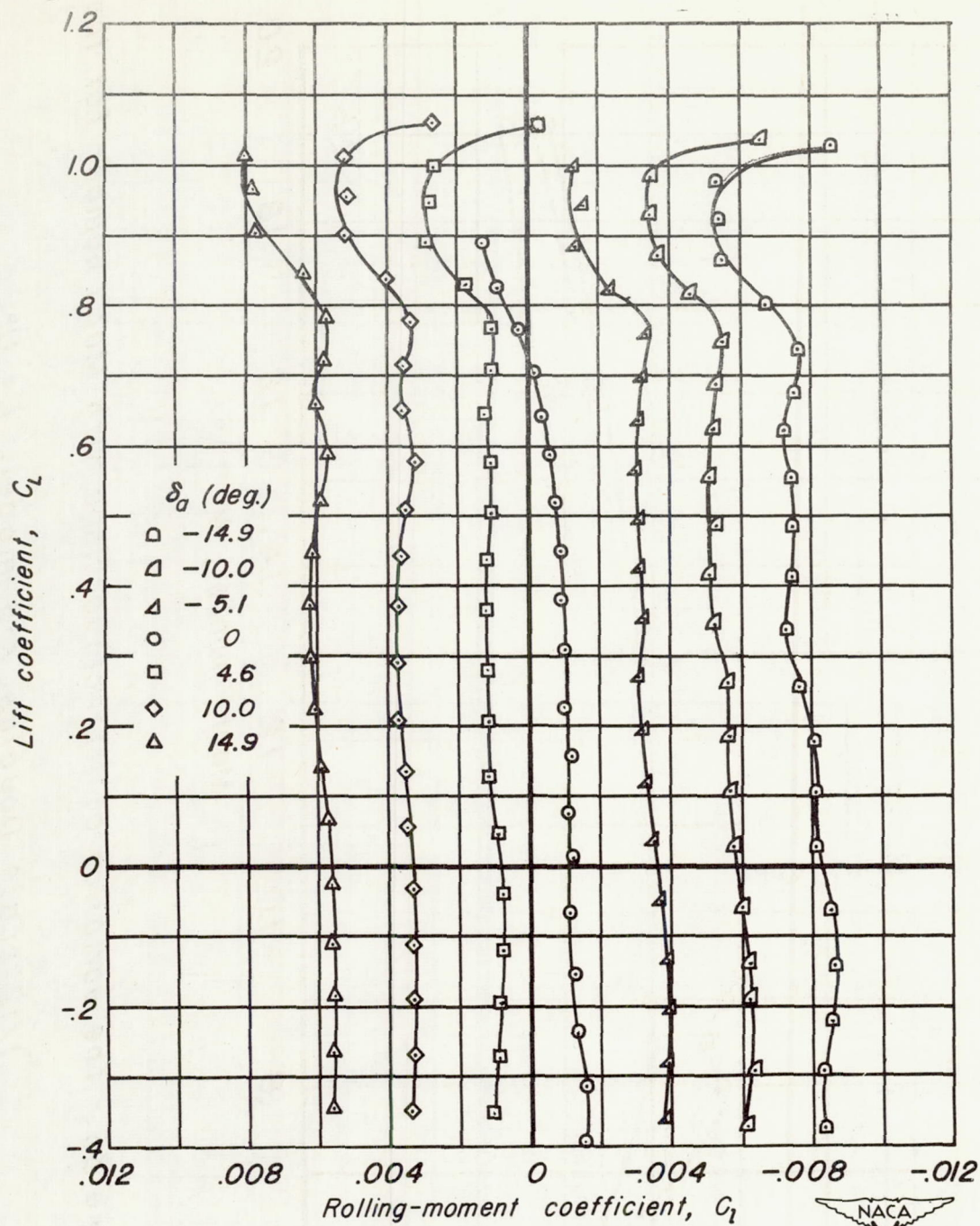


Figure 34.-Lateral control characteristics of the 1/12-scale Douglas X-3 configuration A . $R = 2.09 \times 10^6$; $M = 1.40$.
Data for one aileron .

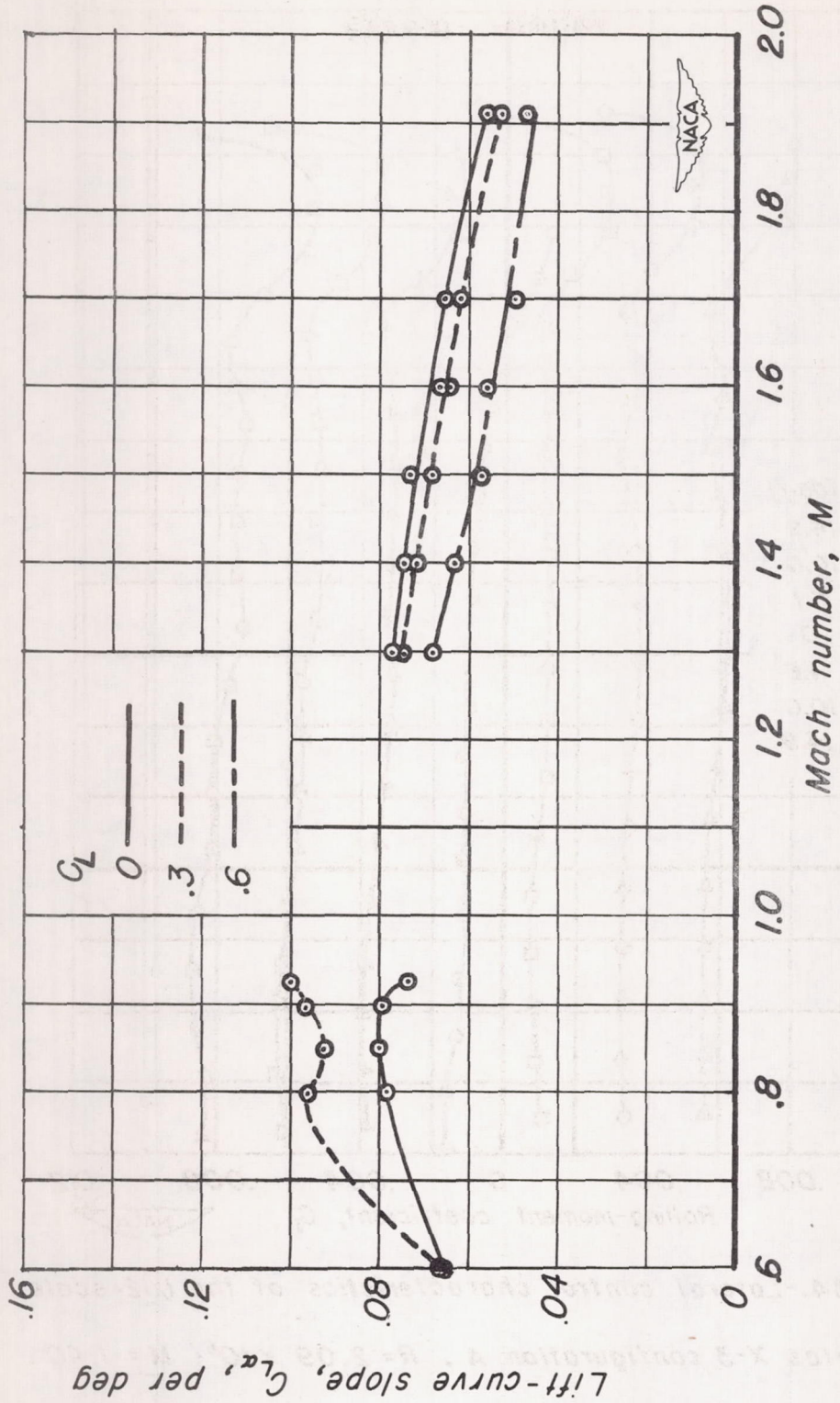


Figure 35.- The variation of lift-curve slope with Mach number for the 1/12-scale Douglas X-3 model. $i_t = 0^\circ$.

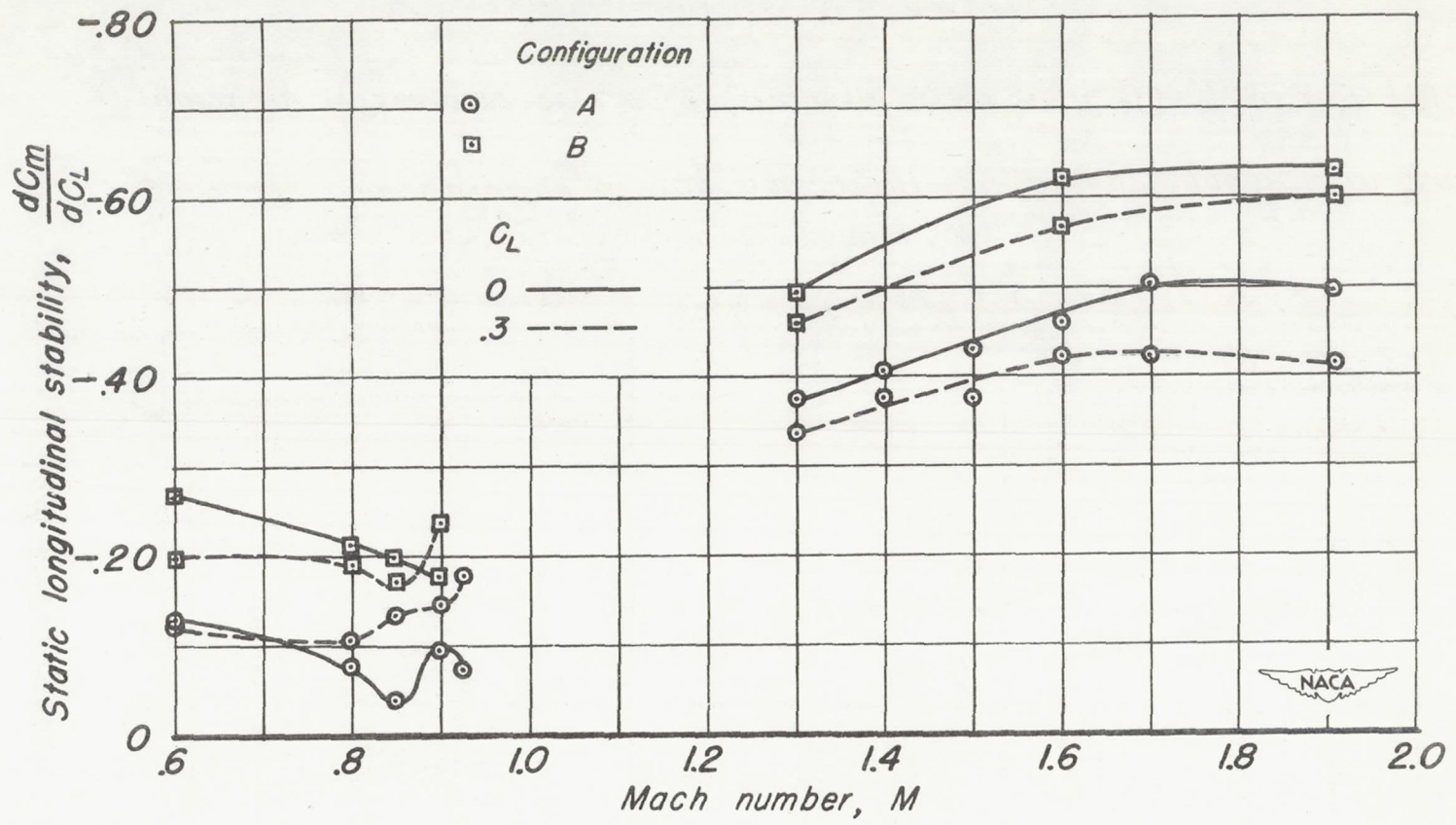


Figure 36.- The variation of the static longitudinal stability with Mach number for the 1/12-scale Douglas X-3 model. $i_t = 0^\circ$.

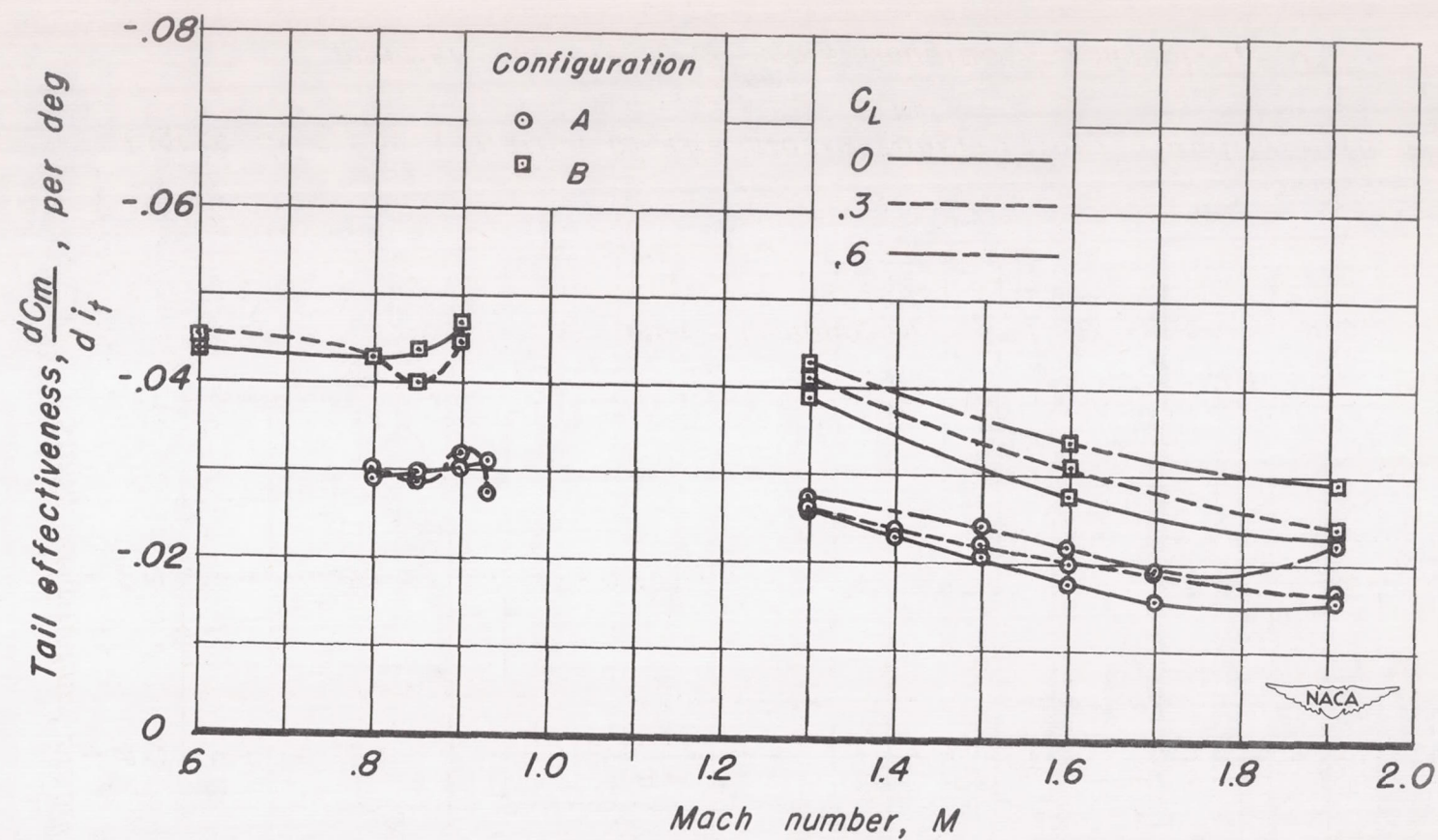


Figure 37.- The variation of the horizontal tail effectiveness with Mach number (measured at $i_t = 0^\circ$) for the 1/12-scale Douglas X-3 model.

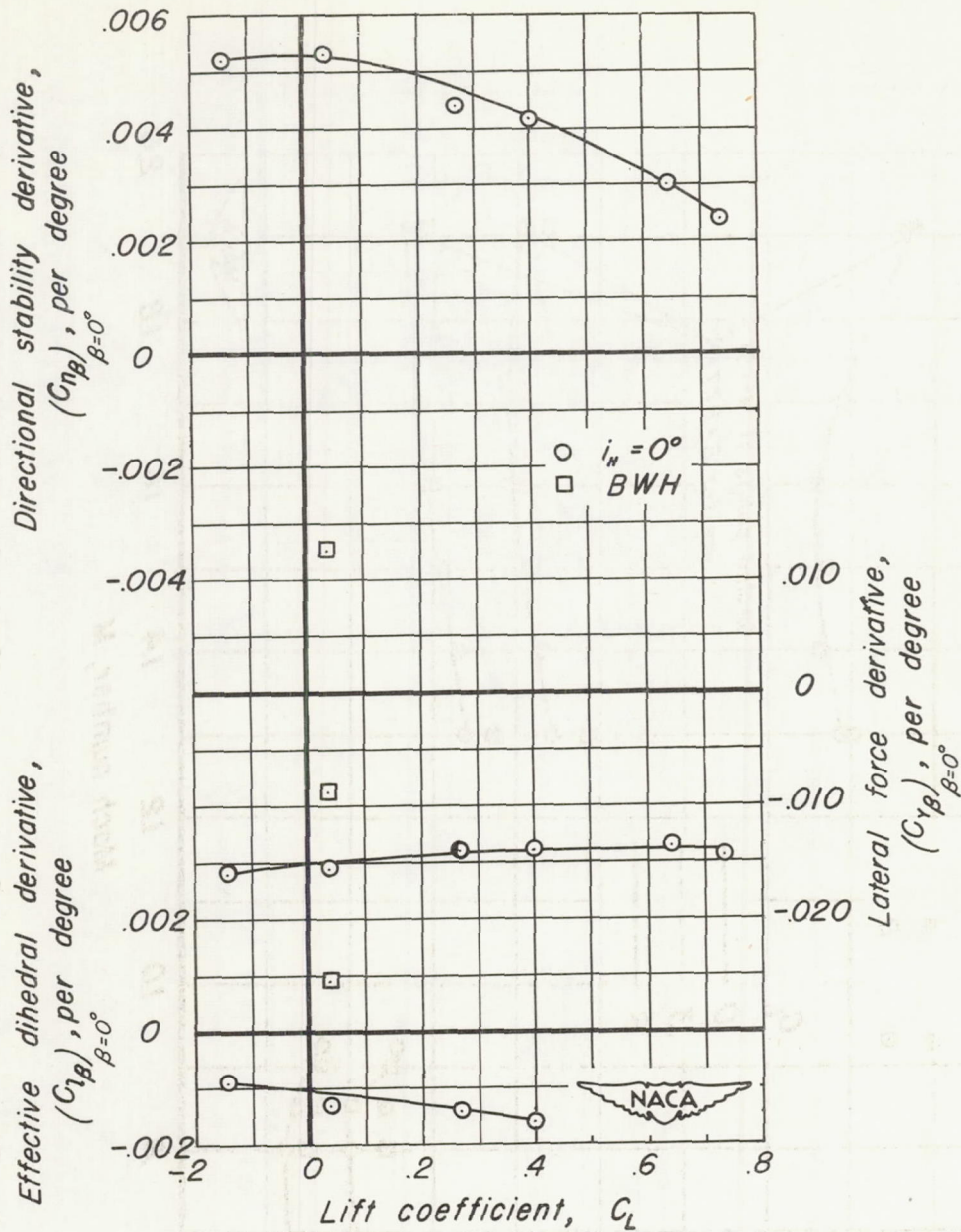


Figure 38.- The variation of the directional stability, lateral force, and effective dihedral derivatives with lift coefficient for the 1/12-scale Douglas X-3 configuration A at a Mach number of 1.40.

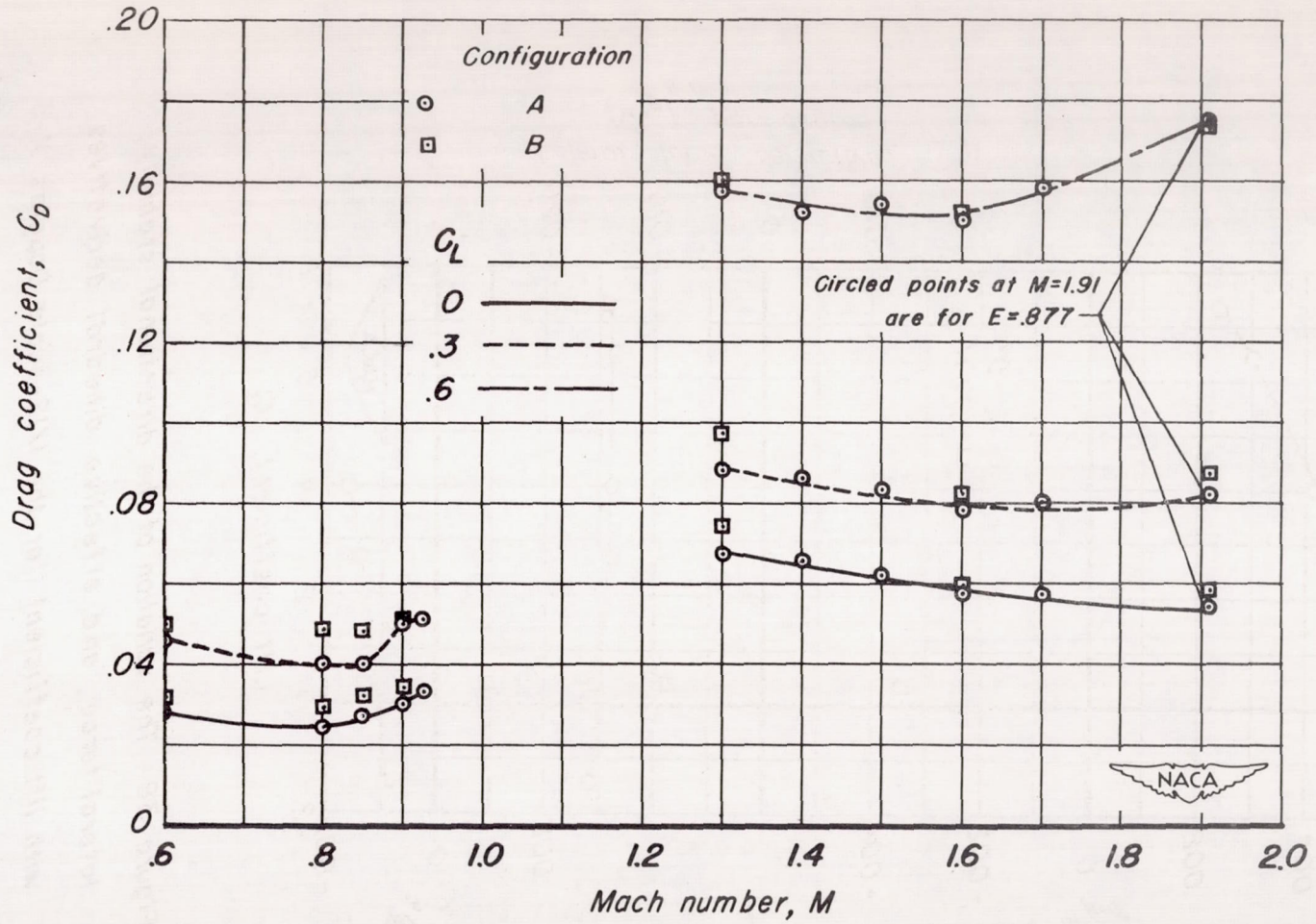


Figure 39.- The variation of drag coefficient with Mach number for the 1/12-scale Douglas X-3 model. $i_T = 0^\circ$.

